Petrology and (U-Th)/He Thermochronology of Mesoproterozoic Kimberlites from the eastern Dharwar Craton, southern India

Manoko Maggie Marokane
(0708883P)

A Dissertation submitted in fulfilment of the requirements for the degree of Master of Science, in the Department of Geosciences, University of the Witwatersrand, Johannesburg, South Africa, 2017

Supervised by Prof. S. Tappe and Dr. K.A. Smart

Declarations

I, Manoko Maggie Marokane (0708883P), declare that this dissertation is my own, unaided work. It is being submitted for the Master of Science Degree by dissertation at University of the Witwatersrand, Johannesburg. It has not been submitted before for any degree or examination in any other University.

Marokane M.M  Date: 05 October 2017

Abstract

Apatite (U-Th)/He thermochronometry data from two different kimberlite clusters of the Dharwar Craton is used, together with geologic constraints, to develop a model for the burial, uplift, and unroofing history of southern India (i.e. Peninsular India). The apatite helium (AHe) dates for the CC-5 kimberlite at a present-day elevation of 398 m range between 128-235 Ma, with a mean age of 164.9 ± 21.2 Ma (1 S.D.). The AHe dates for the SK-2 kimberlites at a present-day elevation of 289 m range from 121.1-170.7 Ma, with a mean age of 166.3 ± 25.2 Ma (1 sigma standard deviation). The mean AHe ages for the CC-5 and SK-2 kimberlites from the approximately 150 km apart Wajrakarur and Raichur kimberlite fields, respectively, are indistinguishable within their uncertainties. This suggests a similar uplift and erosion history of the two areas on the eastern Dharwar craton. All these dates are younger than kimberlite pipe emplacement (ca. 1100 Ma) signalling a major post-emplacement erosion during the Mesozoic (Middle Jurassic). We use the data to link not only uplift and erosion to elevation gain, but to show how this corresponds to deep mantle processes and continental formation or breakup.

Our HeFTy time-temperature modelling results indicate heating to temperatures of ~175 °C suggesting burial, which was followed by an unroofing (cooling) event. Plate tectonic modelling using GPlates software package is also consistent with t-T models, in that the signals observed are also recorded by plate movements (e.g. the 175 Ma). Burial is restricted to a depth of 3 km after pipe emplacement. Erosion estimates show that the Dharwar Craton underwent ≥ 1.5-4 km of erosion during the Jurassic, most likely related to Gondwana break-up that commenced at ~180 Ma.

The fast drift of the Indian plate (18 cm/a) towards the northern hemisphere during the Cretaceous is related to the removal of the once thick cratonic keel beneath the Indian Craton. Whether parts of the mantle lithosphere were delaminated/removed during or post Gondwana is controversially debated. Herein, we propose a model for cratonic root delamination, related to deep mantle processes (i.e., dynamic topography) that may have played a role or aided in lithospheric thinning of the Indian tectonic plate.

Dedication

To my mom

Acknowledgements

The financial assistance of the National Research Foundation (NRF) South Africa towards this research is hereby thankfully acknowledged. Opinions expressed and conclusions arrived at, are those of the author and are not necessarily to be attributed to the NRF. I am indebted to my supervisor Prof. S. Tappe for initiating this project and his valuable insights and ideas and support throughout completion of the project. I also thank the undivided attention, guidance and courage from my co-supervisor Dr. K.A. Smart, and also the financial support in preparation for my trip to the U.S.A. I also thank Prof. Rebecca Flowers for the invitation to the thermochronology laboratory in Boulder and also the financial support through the U.S.A. National Science Foundation (NSF) award no. 0951518 for supporting my travel and living costs in the U.S.A. Many thanks to Dr. James Metcalf and Ms Jaclyn Baughman of the Colorado University Thermochronology Research and Instrumentation Laboratory, for explaining the techniques and analyzing my samples and the continuous support while in the U.S.A. Prof. Jan. Kramers (University of Johannesburg) and Prof. Steven Prevec (Rhodes University) are gratefully acknowledged for providing constructive external reviews of this thesis.

I would like to thank the technical support from Wits University: Mr. C. Majola, Mr M. Cebekhulu and S. Tshabalala who made my thin sections and Mr J. Aphane for allowing me access to the lab in preparation for mineral separation and also for conducting heavy liquids on some of the sample fractions. The EPMA laboratory crew from Rhodes University; Dr. G. Costin, Ms. L. Tisane and Ms. T. Moloto are hereby acknowledged for analyzing my samples and compiling reports. I also thank Dr. C. Reinke of the University of Johannesburg electron microprobe laboratory in conducting additional microprobe analyses with me. Thanks to Mr. L. Glossop of the SGS mineralogy division for QEMSCAN analysis and to Prof. R. Gibson for covering analytical costs. I sincerely thank all my office mates for their continuous help whenever needed. Special thanks to Mr M. Terracin, Mr R.P. Maila, Ms K.D. Hlaole and for their continuous support and courage during the course of this study. Everyone at the geosciences department who contributed in my studies somehow, thank you this research wouldn't have come into completion if it wasn't for your help. How can I forget the geophysics department for loaning me a laptop when a crisis hit my house, thank you to Dr. M. Manzi, Prof. S. Webb and Mr. B. Chinamora. Zamo skhokho saam, ngiyabonga homie. The support of Wits interlibrary staff is greatly appreciated.

Wow, special thanks to my mom Mrs. M.S. Marokane and my dad Mr M.M. Marokane for the care, support and encouragement. The support of my siblings and friends is not taken for granted. Above all, thanks to the Lord Almighty for the strength and wisdom.

Table of Contents

Declarations……ii

Abstract……iii

Dedication……iv

Acknowledgements……v

Table of Contents……...vi

List of Figures……viii

List of Tables……12

List of Symbols……....13

Nomenclature……14

Introduction……16

1 Geological background of southern India ……19

1.1 Eastern Dharwar Craton of Peninsular India……..19

1.1 (i) The Wajrakarur Kimberlite Field…….....21

1.1 (ii) The Narayanpet Kimberlite Field……22

1.1 (iii) The Raichur Kimberlite Field…….....22

1.2 Proterozoic Purana Basins of Peninsular India……..23

1.2.1 Stratigraphy of the Cuddapah Basin……26

1.3 Kimberlite and Lamproite magmatism of Peninsular India ……..…28

1.4 Peninsular India during Gondwana assembly and separation……31

1.5 Previous AFT and AHe Studies of the Dharwar Craton……....33

2 Methods……35

2.1 Sampling……..……35

2.2 Petrography, QEMSCAN and EPMA analysis……35

2.3 Low-Temperature (U-Th)/He Thermochronology ……..….36

2.4 Time-Temperature Modelling……40

2.5 Plate Tectonic Modelling……41

3 Results……..42

3.1 Petrography: Mineralogy and Chemistry……42

3.1.1 Chigicherla Kimberlites……...42

3.1.2 Siddanpalle Kimberlites……42

3.1.3 Mineral Chemistry…….....44

3.2 Groundmass apatite morphologies and compositions……45

3.3 Apatite (U-Th)/He Data……...48

3.4 (U-Th)/He apatite systematics……...55

4 Discussion……57

4.1 Constraints on the uplift and erosion history of Peninsular India……57

4.2 Time-Temperature Modelling ……...62

4.2.1 Model constraints and assumptions……62

4.2.2 Possible thermal histories recorded by Dharwar Craton kimberlites……..65

4.2.3 Preferred Time-Temperature Model……67

4.3 Constraints on the mechanism for uplift and erosion of Peninsular India ……69

4.4 Implications for Gondwana break-up and the fast drift of the Indian tectonic plate ……76

5 Concluding Remarks……...83

6 References……85

Appendix A- Petrographic Descriptions……94

Appendix B- Mineral compositions and plots……98

Appendix C- Apatite Thermochronometry……...118

List of Figures

Figure 1: A generalised geological map of India showing the kimberlites of the Dharwar Craton (EDC), southern India. The occurrence of other kimberlites and lamproites in various cratons is also shown. Sample locations are circled in red. CBF- Chitradurga boundary fault; CITZ-central Indian tectonic zone; CIS- central Indian shear zone; CUB- Cuddapah basin; CB- Chhattisgarh basin; VB- Vindyan basin; SMB- Singhbhum mobile belt; Np- Narayanpet kimberlite field, R- Raichuir kimberlite field, W- Wajrakarur kimberlite field, T- Topakal Kimberlite field, M- Mainpur (Orangeite) field; Mg- Majhgawan; K- Khadka, N- Nuapda; Rd- Ramadugu lamproite field . Map modified from (Chalapathi Rao et al., 2014)…….....16

Figure 2: Location of various kimberlite and lamproites fields in the Eastern Dharwar Craton and historical locations of diamond distributions. WKF- Wajrakarur kimberlite field, NKF- Narayanpet kimberlite field, RKF- Raichuir kimberlite field, KLF- Krishna Lamproite field, RLF- Ramadugu Lampoite field, CLF- Cuddapah lamproite field. Map adapted form (Chalapathi Rao & Dongre, 2010)…….....19

Figure 3: Stratigraphy of the oldest preserved Purana basin, the Cuddapah Basin of the EDC, south India, adapted and modified from Collins et al. (2014) and Joy et al. (2015)…….26

Figure 4: The Indian tectonic plate within Gondwana during Permian times. Contours show present day continental lithospheric thickness in km. Map adapted from Kumar et al. (2007b)……...32

Figure 5: Grain morphologies and size of isolated apatite grains for the Wajrakarur kimberlite field. (a) Shows typical prismatic habits of apatites from sample SK-2 and (b) shows an individual grain before packaging. (b) Shows apatite grains from sample CC-5, which are mostly broken and smaller than those of SK-2, (d) shows the acceptable shape and size to be used for thermochronology analysis. (e) Shows a single grain from sample SK-1; apatites from this sample are generally smaller (both in length and width) in comparison to the CC-5 and SK-2

apatites. (f) Shows an image of a packaged apatite grain in a Pt tube……37

Figure 6: Petrographic properties of the EDC kimberlites. (a-c) show photomicrographs and (d-f) BSE images of samples CC-5, SK-1 and SK-2. (a) & (d) Sample CC-5 shows typical acicular apatite grains forming radiating sprays set in calcite (Cal) rich portions of the groundmass. (b) & (e) show SK-1 sample with macrocrysts of serpentinized olivine grains set in a fine groundmass of serpentine (srp) and perovskite (prv). Apatite (Ap) surrounds earlier formed olivine grains. (c) & (f) Sample SK-2 showing prismatic Ap embedded in serpentine. All samples show inequigranular textures with serpentinized olivines, in a Srp and Cal and spinel groundmass. Note the identical gray scale of all the perovskite grains depicting the lack of compositional zoning……42

Figure 7: Representative QEMSCAN (BSE) images for the EDC kimberlites (a) CC-5, showing the inequigranuar texture, above the red curve is the autolith, note the difference in grain size (grain sizes in the autolith are smaller than those of the later solidied rock). (c) show the detailed section of the circulated part of the CC-5 kimberlite, apatite is present as an acicular mineral set in an interstitial calcite matrix. (b) SK-2, show the textural positions of the groundmass apatite (Ap) grains, the sample is calcite (Cal) rich, with Cal rimming around olivine (Ol) grains Minor ilmenite, barite (Brt) and abundant perovskite (Prv) occur as groundmass minerals……..46

Figure 8. Chemical composition of apatites from the EDC Kimberlites. (a) A plot of SrO versus P2O5. (b) SrO versus CaO……54

Figure 9: Apatite (U-Th)/He data. (a) Individual grain AHe date or age plotted against sample latitude. (b) Date (Ma) plotted against eU (ppm)……55

Figure 10: Chigicherla (CC-5) erosion model. (a) Ideal kimberlite pipe at emplacement. (b) Period of Purana sedimentation until ca. 600 Ma. (c) Shows erosion estimate from 175 Ma to

present. The current pipe exposure is at root zone. The Chigicherla kimberlite experienced a 4 km erosion of crust including 2.5 km of sediments and 1.5 km of granitic basement……59

Figure 11: Schematic pipe model for the Chigicherla kimberlite (CC-5), showing the different zones in the pipe and the current erosion surface after Kirkley et al. (1991) and the estimated current erosion surface for the Chigicherla pipe (this study)…….……60

Figure 12: Emplacement ages for the kimberlites of the EDC Dated with different techniques, most of the dates fall within the Mesoproterozoic era (Paul et al., 1975; Basu & Tatsumoto, 1979; Kumar, et al., 1993; Osborne et al., 2011; Chalapathi Rao et al., 2013)……...63

Figure 13: Time-temperature plots depicting the cooling history of southern India (EDC). Black boxes represent imposed constraints. Light grey and dark grey lines represent acceptable and good fits, respectively. The solid line is the goodness of fit line. A-B shows the simple model A for sample CC-5 (a), and SK-1 & SK-2 (b), model A has kimberlite emplacement as the only constraint. (C-D) shows model B for both sample CC-5 (c) and SK-1 & SK-2 (d), model B has three constraints, constraint 1 is the kimberlite emplacement age at 1100 Ma, constrain 2 represents known continued Purana sedimentation between 800 and 600 Ma, constraint 3 is the AFT data from granitic basement rocks (Sahu et al., 2013). (E-F) show model C, constraint 1 starts at 120-140 °C to allow for burial, constraint 2 and 3 are similar to those of model B……..65

Figure 14a: Representative plate models (GPlates) indicating the movement of the Indian tectonic plate toward its current position in the Northern Hemisphere. At this stage India is still attached to west Gondwana……...71

Figure 14b: Representative plate models (GPlates) indicating the southern movement of the Indian tectonic plate since 165 after its breakup from west Gondwana……72

Figure 14c: Representative plate models (GPlates) indicating the rapid speed (¬20 cm/sec) of the Indian tectonic plate toward the north after its separation from Madagascar at 90 Ma……73

Figure 14d: Representative plate models (GPlates) showing the time period when India was moving northward (90-50 Ma) to collide with Asia (40 Ma) to form the Himalayas……74

Figure 15(a): Model for the lithosphere delamination: schematic diagram for the Dharwar Craton showing cratonic root……..78

Figure 15(b): Model for the lithosphere delamination: Plume beneath the Dharwar Craton…...79

Figure 15(c): Model for the lithosphere delamination: The interaction of the plume with lithosphere leading to cratonic root destruction after Pandey & Agrawal (1999) and Raval & V Veeraswamy (2003). Partial Melting Zone- (PMZ)……..80

Figure 16: A lithosphere-scale cross section through the EDC, WDC and SGT, inferred from available geological and geophysical data. Adapated from Agrawal & Pandey (2004)…….....79

List of Tables

Table 1: EPMA data for apatite compositions for CC-5 kimberlites (EDC)…….51

Table 2: EPMA data for apatite compositions of the CC-5, SK-1, and SK-2 and kimberlites (EDC)……...52

Table 3: EPMA data for apatite compositions for the SK-2 kimberlites (EDC)……..53

Table 4: EPMA data for apatite compositions for the SK-2 kimberlites (EDC) continued..……..54

Table 5: (U-Th)/He thermochronology data for the EDC kimberlite…….55

Table 6: Estimated erosion levels of some kimberlites in the world, from (Brown & Valentine, 2013)……...60

List of Symbols

Al_2O_3- Aluminum oxide

CaO- Calcium Oxide

Cr_2O_3- Chromium (III) oxide

eU- Effective uranium concentration

FeO* - Total iron

He- Helium

NiO- Nickel oxide

MgO- Magnesium oxide

Mg#- Fo [Mg/(Mg + Fe)]

MnO- Managnese (II) oxide

Nd-Neodymium

nmol/g- Nano moles per gram

SiO_2- Silicon dioxide or quartz

Sm- Samarium

Th- Thorium

TiO_2- Titanium oxide

t-T- Time-temperature

U- Uranium

V- Vanadium

µg- Micro-gram

µm- Micro-meter

Nomenclature

AFT- Apatite Fission Track

AHe- Apatite Helium

Ap- Apatite

BC- Bastar Craton

Cal- Calcite

CB- Cuddapah Basin

Cpht- Carats per hundred tonnes

CSB- Chitradurga Schist Belt

Cts- Carat

CZLF- Chelima Zangamrajupalle Lamproite fields

BMA- Bulk Modal Mineralogy

CCR- Archaen cratonic region

BSE- Back-scattered electron

EDC- Eastern Dharwar Craton

EDS- Energy Dispersive Spectrometry

EGMB- Eastern Ghats Mobile Belt

EPMA- Electron Probe Micro Analyser

Ga- Giga-annum (billions of years)

GSI- Geological Society of India

HeTM- He Trapping Model

KLF- Krishna Lamproite Field

LAB- Lithosphere Asthenosphere Boundary

LIP- Large igneous province

Ma- Mega-annum (millions of years)

MBSASZ- Moyar-Bhavani-Salem-Attur Shear Zone

Myr- Million years ago

NLF- Nauapada Lamproite Field

NKF- Narayanpet Kimberlite Field

Ol- Olivine

PMZ- Partial Melting Zone

Ppm- Parts-per million

Prv- Perovskite

Pt- Platinum

QEMSCAN- Quantitative Evaluation of Materials by Scanning Electron Microscopy.

RDAAM -Radiation damage accumulation and annealing model

RKF- Raichur Kimberlite Field

rs- Spherical radius

Rt- Rutile

PRZ- Phi-Rho-Z

Serp- Serpentine

SIMS- Secondary ion mass spectrometry

SGT- Southern Granulite Terrain

TTGs- Tonalities trondjhemites-granites

UML- Ultramafic lamprophyres

Ulvo- Ulvospinel

WKF -Wajrakarur Kimberlite Field

Zr- Zircon

Introduction

Old and stable continental regions are underlain by a thick lithosphere (Harris & Middlemost, 1969; Kumar, et al., 2007b); this is supported by the presence of numerous diamondiferous regions in the interior (Lehmann, 2010). Seismic studies such as those conducted by Kumar et al. (2007b) in the region of the Indian ocean and the surrounding fragments of Gondwana revealed that the Indian Craton is thinner (80-100 km) compared to the thick lithosphere of Australia, Antarctica and South Africa (Lehmann, 2010). Roy and Rao (2000) and Griffin et al. (2009) have demonstrated that the Dharwar Craton (DC) has typical heat flow values of 40-50 mW/m^2, and this is consistent with modern cratonic geotherm of ~20°C/km (Ault et al., 2013). Although the Indian shield is thought to have been in a steady state thermal condition in the past 1000 Ma (Ganguly & Bhattacharya, 1987), present day reconstruction of Gondwana shows lithospheric thinning (~100 km) beneath India and east Africa (Kumar et al., 2007b). The lithosphere beneath Peninsular India and South Africa are thought to be at least 185 km thick during the Mesoproterozoic to Cretaceous period (Ganguly & Bhattacharya, 1987; Karmalkar et al., 2009; Patel et al., 2009).

The presence of ca. 65 Ma old diamondiferous kimberlite events synchronous with the eruption of the Deccan Traps large igneous province was recognized in the Bastar Craton of central India by Lehmann et al. (2010). Chalapathi Rao and Srivastava (2012) suggested that this illustrates the lithosphere of the Indian shield was thick at the end of the Cretaceous and therefore the rapid drift of the Indian plate towards the north cannot be linked to lithospheric thinning.

The breakup of Gondwana into Africa, Antarctica, Australia and India has been envisaged to be the result of heating of the lithosphere from below by a large mantle plume whose relicts are now the Marion, Kerguelen and Reunion plumes. In comparison to other fragments of Gondwana, the Indian lithospheric plate has been shown to extend to ~100 km depth, whereas the lithospheric roots in South Africa, Australia, and Antarctica are estimated to be between 180 and 300 km deep (Kumar et al., 2007b). Processes that led to thinning of the Indian lithosphere remain a controversy. India's fast northward drift (18-20 cm/yr) in the Mesozoic has been linked to plume-related delamination of its cratonic lithosphere (Pandey & Agrawal, 1999; Kumar et al., 2007b). The Indian-Subcontinent, is the only continent that travelled a distance of about 9000 km within a short time span of less than 50 Myr during post-Pangaea period, scars of the long journey are reflected in the form of a degenerated lithosphere. Different studies have attested to the lithospheric thinning or removal beneath the DC, this includes petrological (Griffin et al., 2009), seismological (Kumar et al., 2007a) and magnetotelluric studies (Naganjaneyulu &

Santosh, 2012) . Naganjaneyulu and Santosh, (2012) and Kumar et al., (2007b) suggested that the removal or the significant modification of the cratonic root might have occurred during Gondwana breakup. This study argues that plate movements alone cannot be responsible for ~85 km of root delamination. Removal of a refertilized mantle and plate movements over hotspots might have aided in delaminating the cratonic root thereby causing India's rapid drift towards the north. This study makes generalised conclusions based on the data set used and has implications for understanding the tectonics of India.

In this study we report new apatite (U-Th)/He thermochronology data for kimberlite rocks of the Dharwar Craton (DC), which is divided into two blocks: 1) the Eastern Dharwar Craton (EDC) and 2) the Western Dharwar Craton (WDC). The focus of the study is only on the EDC; no kimberlites and related rocks are known from the WDC (Fareduddin and Mitchell, 2012). Samples were collected from the Raichur (RKF) and Wajrakarur (WKF) kimberlite fields by Prof S Tappe during the 10th International Kimberlite Conference held in India in 2012. We measured apatite He ages for kimberlites from the Siddanapalli cluster of the RKF and Chigicherla cluster of the WKF (Figure 2). Methods involve conventional crushing, milling, sieving and isolation of magnetic and non-magnetic minerals to recover apatite, determination of U, Th, and Sm contents, and dissolution of apatite grains to extract helium gas (^{3}He/^{4}He). The age data are then modelled using HeFTy software package to randomize t-T paths, which records the history of cooling of rocks (Ketcham, 2005). The aim is to unravel periods of significant uplift and erosion, which are believed to be caused by processes that operate deep within the Earth's mantle. We show here how apatite can be used as a thermochronometer for recording cooling history of rocks as they pass through the upper crust (~1-3 km) and therefore use the data to link burial and unroofing events to better understand the tectonics of southern India between 1 Ga and present-day.

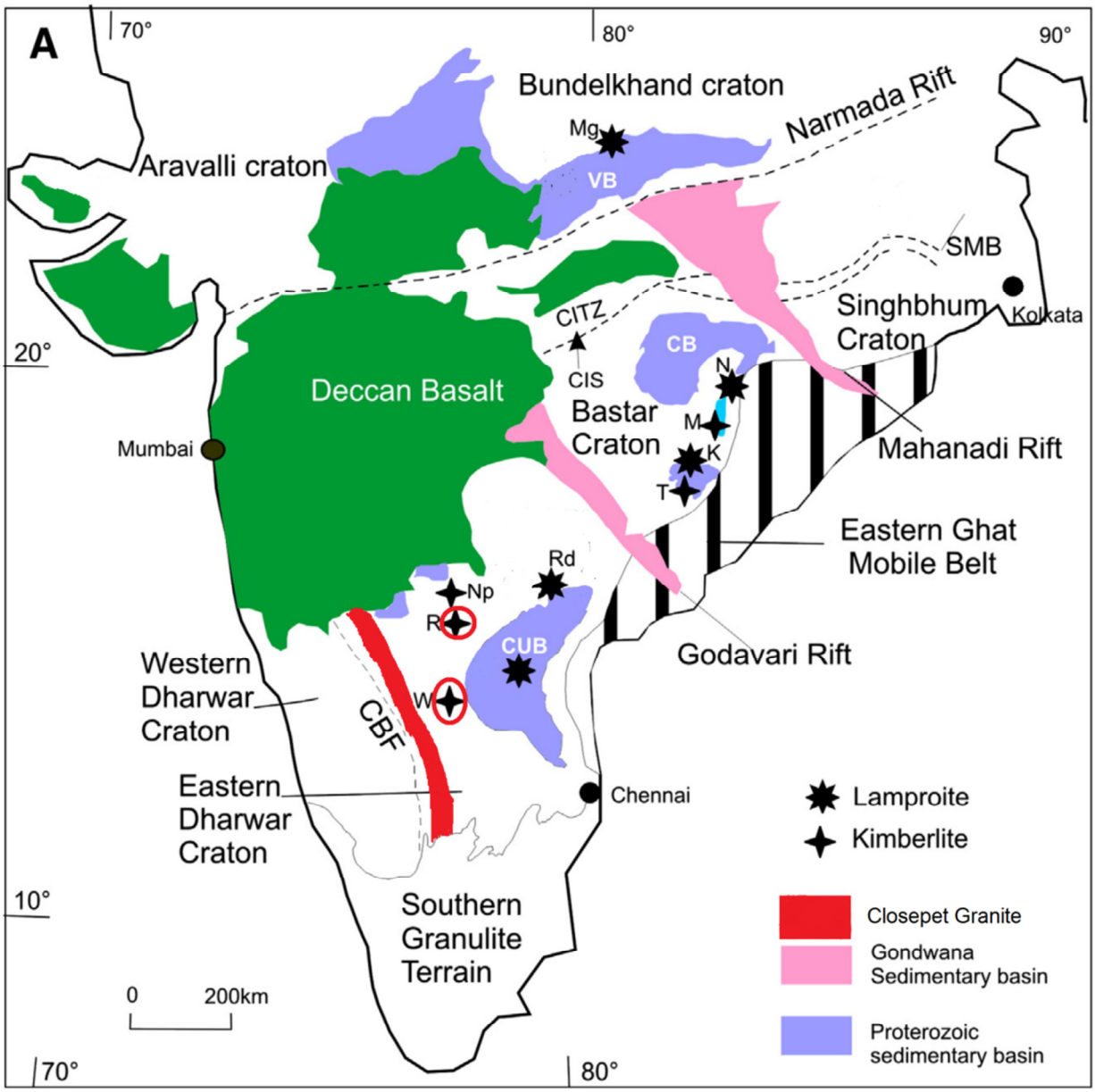

Figure 1: A generalised geological map of India showing the kimberlites of the Dharwar Craton (EDC), southern India. The occurrence of other kimberlites and lamproites in various cratons is also shown. Sample locations are circled in red. CBF- Chitradurga boundary fault; CITZ-central Indian tectonic zone; CIS- central Indian shear zone; CUB- Cuddapah basin; CB- Chhattisgarh basin; VB- Vindyan basin; SMB- Singhbhum mobile belt; Np- Narayanpet kimberlite field, R- Raichuir kimberlite field, W- Wajrakarur kimberlite field, T- Topakal Kimberlite field, M- Mainpur (Orangeite) field; Mg- Majhgawan; K- Khadka, N- Nuapda; Rd- Ramadugu lamproite field . Map modified from Chalapathi Rao et al. (2014).

1 Geological background of southern India

1.1 *Eastern Dharwar Craton of Peninsular India*

The Indian shield is an amalgamation of several cratons: Dharwar, Singhbhum, Aravalli, Bundelkhand, and the Bastar (Chalapathi et al., 2013) as shown in figure 1. Each of these cratons has low heat flow (31-41mW/$m^{2)}$ and is bordered by mobile belts or rift zones with substantially higher heat flow (61-74 mW/m^2) (Haggerty & Birkett, 2004). An earlier study by Roy and Rao (2000) suggested low heat flow values for these cratons ranging from 25 to 50 mW/m^2.

The Archaean Shield complexes of the Indian peninsula were assembled, separated and reassembled into two large cratonic provinces, the northern and the southern provinces (Chaudhuri et al., 2001). The ENE-WSW trending narrow linear zone known as the Central Indian Mobile Belt (CIMB) or as the Central Indian Tectonic Zone (CITZ) separates the northern provinces and the southern provinces. The northen and the southern cratonic provinces constituting the Indian peninsula and an undetermined amount of crustal material thought to have been subducted under the Himalayas were part of Gondwana and perhaps also of the earlier Proterozoic continent (Rogers, 1986; Chaudhuri et al., 2001).

The northern cratonic province includes only the Bundelkhand (Aravalli) Craton whereas the southern cratonic provinces include the Singhbhum, Bastar, EDC and WDC and the Southern Granulite Terrain (SGT). All these are believed to have amalgamated by ca. 2.5 Ga, detached and re-amalgamated along the western margin of the Bastar at ca. 1.6 Ga (Basu & Bickford, 2015). The SGT is one of the has preserved Archean crust with extensive granulites and it is separated from the DC by Moyar-Bhavani-Salem-Attur Shear Zone (MBSASZ), which is a transition zone marked by gradation in metamorphism from gneiss in the north to charnockite in the South (Collins et al., 2014).

Situated in southern India, the Archaean DC is a continental fragment with a continuously exposed crustal section formed of low-grade gneisses, greenstones and granulites (Balasubrahmanyan, 2006). The granite-greenstone terrain is exposed in the states of Karnataka, Andhra Pradesh, Kerala and Tamil Nadu (Fareeduddin & Mitchell, 2012). The Peninsular Gneissic complex consists of tonalities, trondhjemites and granites (TTGs), emplaced during several cycles of cratonic accretion between 3.3 to 3.0 Ga. These TTG gneisses and the greenstone belts of the DC are intruded by a number of Paleoproterozoic

granitic bodies Fareeduddin & Mitchell, 2012). The DC is bordered in the east by the Proterozoic Eastern Ghats Mobile Belt and in the north by the Cretaceous-Tertiary lavas of the Deccan Traps (Ravi et al., 2012).

The Dharwar Craton, based on formation ages, crustal and lithospheric thickness estimates as well as the characteristics of schist belts and abundance of younger granites (Sunder Raju et al., 2014; Joy et al., 2015), is subdivided into two segments: the eastern Dharwar Craton (EDC) and the western Dharwar Craton (WDC). The WDC is composed of tonalite-trondhjemite-granodiorite (TTG) type peninsular gneisses and greenstone belts (komatiite basalt) of two differing ages (3.35 Ga in south and 2.9 Ga in the north part of the craton). The EDC is composed largely of 2.7-2.5 Ga TTG and gneisses and 2.56-2.5 Ga plutonic bodies, with the prominent feature being the N-S trending Closepet batholith (Kumar et al., 2015). The 600 km north-south trending suite of granite bodies known as the Closepet Granites (Figure 1) is located at the site of differing crustal thickness and could possibly mark a rift zone (Balasubrahmanyan, 2006) dividing the DC into these two segments (Fareeduddin & Mitchell, 2012). Linear belts of ancient supracrustals (older greenstones) occur east of the Closepet Granite and as rafts in the EDC (Lynn et al., 2013). The Closepet Granite lies at the juncture of EDC and WDC cratons and represents the amalgamation and final cratonization event at ~2.5 Ga (Saha & Patranabis, 2013).

Geological and geophysical studies have demonstrated that the two cratons have different lithologies and must have developed as two distinct terranes (Fareeduddin & Mitchell, 2012). The Chitradurga Schist Belt (CSB) represents a crustal shear zone defining the boundary between the EDC and WDC (*Naqvi and Rogers*, 1987). Both these cratons have evolved differently; the WDC records older (3.2-3.0 Ga) orthogeisses and granites whereas the EDC records a younger (2.6- 2.5 Ga) crustal accretionary event of juvenile and anatectic granites (Fareeduddin & Mitchell, 2012). The WDC was cratonized prior to 2.6 Ga, whereas the EDC was rejuvenated by massive late Archean magmatism (Kumar et al., 2015).

The EDC of southern India is thought to be the world's largest region host to Proterozoic kimberlites and lamproites, with more than 100 known occurrences (Chalapathi Rao et al., 2013). Kimberlites of the EDC are confined to three distinct fields: 1) the diamondiferous Wajrakarur Kimberlite Field (WKF); 2) the non-diamondiferous Narayanpet Kimberlite Field (NKF) and 3) the Raichur kimberlite field (RKF) (Osborne et al., 2011; Chalapathi Rao et al., 2013). Major element concentrations of garnet concentrates from the WKF and NKF kimberlites reveal that diamonds in the WKF have been derived from both lherzolitic and harzburgitic

varieties, whereas the rarity of diamondiferous kimberlite in the NKF is attributed to be due to shallower depth of origin of the kimberlite magma (Chalapathi Rao & Srivastava, 2012). The following subsections give a brief introduction on kimberlite occurrences in these three kimberlite fields of the EDC:

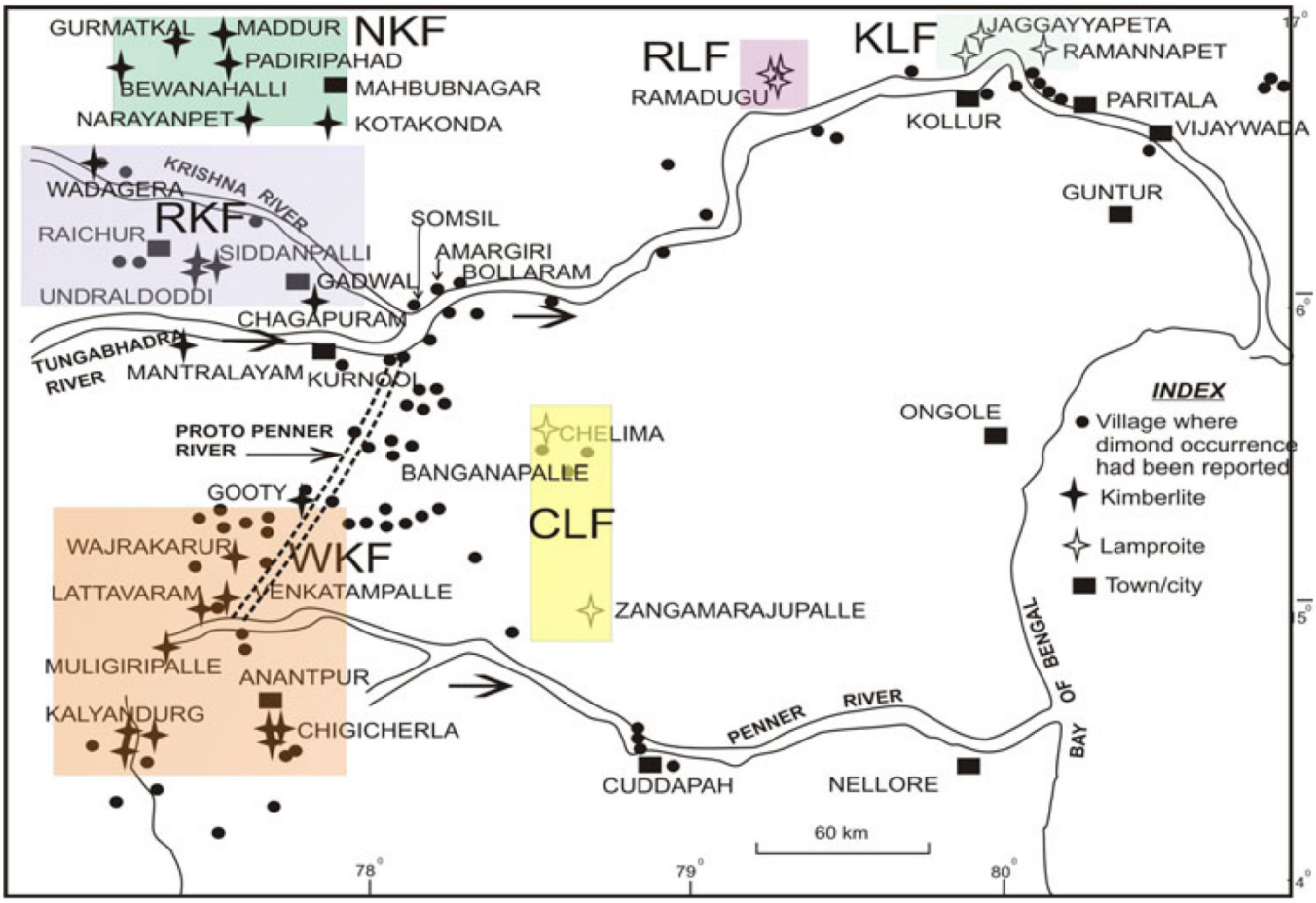

Figure 2: Location of various kimberlite and lamproites fields in the Eastern Dharwar Craton and historical locations of diamond distributions. WKF- Wajrakarur kimberlite field, NKF- Narayanpet kimberlite field, RKF- Raichuir kimberlite field, KLF- Krishna Lamproite field, RLF- Ramadugu Lampoite field, CLF- Cuddapah lamproite field. Map adapted from Chalapathi Rao and Dongre (2010).

(i) The Wajrakarur Kimberlite Field

The WKF, also known as Anantapur district, is located west of the Cuddapah Basin (Figure 1) and it is the largest diamondiferous kimberlite field (~180 km x 70 km) in Peninsula India (Ravi et al., 2012). Kimberlites of the WKF are emplaced into granites and gneisses of the EDC (Fareeduddin & Mitchell, 2012). The WKF consists of a total of 45 kimberlite bodies with 31 bodies occurring in four clusters: Wajrakarur-Lattavaram (14 intrusions, P1-P14), Kalayandurg

(6 intrusions, KL1-KL6), Chigicherla (5 intrusions (CC1-CC5) and Timmasamudram (6 intrusions, TK-1-TK6) (Figure 2) (Ravi et al., 2012). The other 14 intrusions of the WKF (WK1-WK14) have been discovered by Rio Tinto Exploration. Although diamonds have been recovered in the WKF, (Ravi et al., 2012 and references therein), grades are typically below 2 carats per hundred tonnes (cpht). However, many recovered stones are of gem quality and the largest diamond recovered is a sizeable 16.3 carat stone (Ravi et al., 2012). One sample (CC-5) analysed in this study is from the Chigicherla kimberlite cluster, below is a short description of the kimberlite pipe.

- **Sample CC-5** (77.6361 E, 14.5188 N) from the Chigicherla cluster of the WKF: A narrow pear-shaped body of dimensions 220m × 70m with an ENE–WSW trend and emplaced into basement granitoid rocks. The pipe is located ~1 km NE of Gollapalle. The kimberlite outcrops as boulders. This magmatic body is characterised by an abundance of kimberlite melt-in-melt segregations (or globular segregations), which give the outcrop a nodular appearance. Crustal xenoliths of granitoids are common. Kimberlite magma emplacement at 1099 ± 12 Ma was determined by Chalapathi Rao et al. (2013) using the Secondary ion mass spectrometry (SIMS) U-Pb perovskite method. The pipe is currently exposed at root zone level. The use of AHe data in HeFTy to produce t-T plots and calculation of erosion estimates will aid in reconstructing the ideal (original) kimberlite pipe (Figure 11) prior to uplift and erosion.

(ii) The Narayanpet Kimberlite Field

The NKF is located in the western part of Mahbubnagar district (Fareeduddin & Mitchell, 2012; Ravi et al., 2012) and consists of 32 pipes in five clusters: Kotakonda (7 pipes), Maddur (11 pipes), Narayanpet (10 pipes), Bhima (4 pipes) and Raichur (4 pipes) (Figure 2) (Kumar et al., 2007a).

(iii) The Raichur Kimberlite Field

Raichur Kimberlite Field is located in the eastern part of Raichur in Karnataka district and also lies 75 km southwest of the NKF and about 100 km north of the WKF (Figure 1). Alluvial diamonds are known from this region for the last 600 years (Fareeduddin & Mitchell, 2012). The RKF contains the Raichur, Siddanpalle and Tungabhadra clusters (Figure 2) (Chalapathi Rao et al., 2013).The Proterozoic Bhima sediments located 30 km NW of NKF unconformably overlie the Archean granite-greenstone terrain. Limestone xenoliths hosted by kimberlites from the Siddanpalle cluster are thought to have originated from the Proterozoic Kurnool and Bhima sedimentary sequences (Chalapathi Rao & Dongre, 2010; Chalapathi Rao & Srivastava, 2012).

Two samples in this study are from the Siddanpalle Kimberlite Cluster, and following is the short descriptions of the individual pipes:

- **Sample SK-1** (77.5543 E, 16.1909 N) of Siddanpalle cluster in the RKF: located about 2 km N25°E of Siddanpalle and emplaced within pink granitoids. The dimensions of the kimberlite body are 100 m × 65 m with good outcrops in relatively low ground (i.e. forming a depression). The kimberlite is dark grey with macrocrysts of olivine, mica, ilmenite and crustal xenoliths of granite and carbonates. Emplacement ages range from 1093 ± 4 and 1093 ± 18 Ma to 1063 ± 41 Ma, (Chalapathi Rao et al., 2013).

- **Sample SK-2:** is an oval kimberlite body, which appears to be a composite pipe with a main phase of 110 m and 50 m and a small satellite plug (10 x 10 m). The kimberlite is covered by 1 m of calcrete. Some of these hard greenish black outcrops of the main body are exposed along a stream. This kimberlite body has an emplacement age of 1093 ± 4 Ma determined by Kumar et al. (2007a) using the Rb-Sr-phlogopite method.

1.2 *Proterozoic Purana Basins of Peninsular India*

Basins occur in many shallow (<5 km), large and small depressions in the Archean-Paleoproterozoic cratons in peninsular India. Purana basins are largely unmetamorphosed, deformed or only slightly deformed at basin margins and devoid of body fossils (Basu & Bickford, 2015). The 1.1 Ga kimberlites of the Dharwar Craton intruded into these basins; of importance is the fact that some of these kimberlites are eroded to root zone level. The systematics of how and when these kimberlites eroded is important in this study. The knowledge of the opening and closing of Purana basins will aid in having a well constrained geologic time frame where paths are supposed to pass in our AHe models. The emplacement of kimberlites in undeformed inverted Purana basins may have implications for the source of iconic alluvial diamonds known to occur in India such as the Krishna River valley, e.g. the Great Mogul.

Mahadevan (2013) stated that 'These basins developed on a strong lithosphere that evolved due to cooling of the earth. The strong lithosphere was subjected to slow extension attended by early magmatism in some of the basins (Chakraborty et al, 2010) and emplacement of dyke swarms along extensional fractures in the basement gneissic complex. The dyke swarms are episodic with peak emplacements of 2.4, 2.1, 1.6, and 1.0 (Sarkar and Mallick, 1995). Notably, the dike swarms include diamondiferous kimberlitic emplacements in the time span of 1100-1300 Ma along a long corridor in the interior of the Archaen cratonic region (CCR). Their

emplacement implies a progressive deepening of the mechanical boundary layer of the lithosphere down to the diamond stability field (> 155 - 185 km)'.

The term Purana (meaning old) was introduced into the literature by Holland (1907) and subsequently applied to all fossil-free deposits (Wu et al., 2014; Basu & Bickford, 2015) resting on the Archean crystalline rocks with a profound (Great Eparchean) unconformity. Seven supracratonic Proterozoic basins occupy more than one fifth of the Precambrian exposure in the Indian peninsula. These basins contain one of the most intricate records of Middle to Late Proterozoic (Riphean–Vendian) sedimentation preserved in an unmetamorphosed and only slightly deformed state (Wu et al., 2014). The majority of Purana basins and outliers occur in the Bastar Craton and EDC suggesting that the basins could be remnants of a larger basin or that they were connected from time to time (Basu & Bickford, 2015). The Bhima and the Kurnool basins are believed to have been inter-connected during ca. 1.1 Ga kimberlite emplacement (Sharma & Shukla, 2012).

Basu and Bickford (2015) used basin correlation, their ages and tectonic framework to track the opening and closing of Purana basins. Although these basins were thought to be homotaxial, it is currently known that the basins opened and closed at different times, with the majority closing around 1000 Ma. The opening and closing of Purana basins collectively span an age from 2000 Ma to 520 Ma (Basu & Bickford, 2015). These authors also recognise three sets of Purana basins in Peninsula India: 1). The oldest set comprising the Cuddapah *sensu stricto* (Papaghni-Chitravati; Kaladgi-Badami, Lower Vindyan; Gwalior-Bijawar-Sonrai); believed to have opened between 2.0 and 1.9 Ga and most likely closed before the intrusion of the 1.4 Ga lamproites; 2). The largest set of basins (Upper Vindhyan, Chhattisgarh, Indravati, and Khariar), which opened between 1.4 Ga and 1.5 Ga and inverted (uplift of a sedimentary basin) shortly after 1.0 Ga 3). The youngest set of basins includes Marwar, Kurnool and possibly Sullavai Group at the top of Albaka and Mallampalli successions, which opened at ca. 750 Ma and closed prior to the Cambrian explosion but no later than 520 Ma.

Most of the Purana basins have mobile belts overriding them, with the exception of the Kalagadi-Bhima Basin (Ram et al., 2007). Individual sequences vary in thickness from less than 200 m to over 10 000 m and contain predominantly orthoquartzite–shale-carbonate suites. The Purana Basins are comparable with the Proterozoic–Early Palaeozoic basins of North America, the Russian platform and the Australian basins with respect to the prolonged duration of basin history, shape, size and sediment thickness and depositional systems (Chaudhuri et al., 2001). These basins span almost a billion years of history between 1600 Ma to perhaps 500 Ma.

All the Purana basins of undeformed Proterozoic sedimentary successions lie above a basal unconformity over Archean granitoid basement, predominantly quartzite-shale-carbonate successions. The common occurrence of stromatolitic carbonates with algal and other micro-fossil is comparable to those of Russian Rephean sequences (Saha & Patranabis, 2013); which also share a common aspect of flat lying, undeformed Proterozoic sedimentary successions. The occurrence of carbonaceous microfossils, occurring normally in shales, cherts and carbonate rocks are recorded from Australia, Alaska, Canada, China, Greenland, India, Mongolia, Russia and Saudi Arabiab (Sharma & Shukla, 2012). In the Indian sedimentary successions, most recent are the different species of microfossil Obrucehvella, which occur in the Owk Shale of the Cuddapah Supergroup. These fossils are considered as a typical Vendian marker from close to the Precambrian-Cambrian boundary successions (Sharma & Shukla, 2012).

At the northern margin of the WDC lie the smaller Bhima and Kaladgi basins. The Bhima Basin exposed on the northeastern margin of the DC as a sigmoidal array of en-echelon with an aggregate area of 5000 km^2, this is perhaps the smallest and perhaps the youngest of the independently recognized Purana basins (Saha & Patranabis, 2013). The Bhima Basin comprise of clastic and limestone sequence in Karnataka and Andhra Pradesh, this basin is split up into a lower Sedam and upper Andola subgroups with an Archean granite, gneiss and schist as the basement and is covered by the Deccan Traps. The disconformity at the top of the Bhima succession represents a long lapse of time accounting for the vertical uplift and cratonization. A number of limestone and metasomatised carbonate xenoliths occur in the 1,090 Ma Siddanpalle kimberlite cluster of the RKF (Chalapathi Rao & Dongre, 2010). Their derivation has been demonstrated to be from the Kurnool and Bhima sediments. This provides evidence for the continuity of the Purana Basins of Peninsular India (Chalapathi Rao & Srivastava, 2012), and supports a Mesoproterozoic age of these basins contrary to the existing knowledge that they are Neoproterozoic (Patel et al., 2009).

The crescent shaped Cuddapah Basin (CB) is the largest intracratonic basin on the EDC. The Cuddapah Basin, exposed on the eastern margin of the DC, covers an area of 445,000 km^2 (Fareeduddin & Mitchell, 2012) and shows increasing metamorphic grade from west to east, attributed to the Proterozoic Eastern Ghats orogeny (Chalapathi Rao et al., 2004). The basin contains the thickest of the Purana sequences with estimates of around 13 000 m in thickness (Fareeduddin & Mitchell, 2012; Saha & Patranabis, 2013). Mafic dykes and sills of 1.88 Ga are reported from this basin (Chalapathi Rao & Srivastava, 2012). Radiometric age determinations

suggest three major episodes of dyke emplacement: 1900-1700 Ma, 1400-1300 Ma, and 1200-1100 Ma (Fareeduddin & Mitchell, 2012).

The eastern margin of this basin is marked by a deep crustal, the eastern part of the Cuddapah basin is overthrust by the Nallamalai fold belt (NFB) and the Nellore schist belt (NSB) (Saha & Patranabis, 2013). The western margin is marked by a profound non-conformity with Cuddapah rocks lying on the Archean Peninsula Gneissic Complex (Fareeduddin & Mitchell, 2012). The CB is a composite of four sub-basins: Papaghni-Chitravati, Palnad, Srisailam, and Kurnool (Collins et al., 2014). The CB was initiated by block or down-faulting in the western part, whereas the Kurnool, Palnad subbasins originated by down-faulting in the east, west, and north. The oldest intracratonic sedimentary rocks of the Purana basins, i.e. Paleoproterozoic units, are preserved in the Cuddapah Basin (Saha & Patranabis, 2013).

1.2.1 Stratigraphy of the Cuddapah Basin

Basin infill is subdivided into four unconformity-bound sequences which are thought to have developed under syn-post-rift cycles. Sedimentation in each cycle commenced with the deposition of conglomerates, immature feldspathic sandstones representing syn-rift immature clastic deposits. Deposition grades upwards to a highly mature-quartz-arenite-carbonate succession indicative of a post-rift, passive stage subsidence (Saha & Patranabis, 2013) (see figure 3 for the stratigraphy).

Cuddapah sedimentation commences with the deposition of the Gulcheru Formation conglomerates and sandstones of the Papaghni Group (thickness 2110 m), deposited within a series of fan deltas and shelf bar sequences. These sediments uncomformably overlie the Archean basement rocks of the EDC (Chaudhuri et al., 2001; Collins et al., 2014, Joy et al., 2015). The carbonate-dominated Vempalle Formation gradationally overlies the Gulcheru Formation. It comprises dolomitic limestones, stromatolites and algal laminates interbedded with dolomites, calcareous shales, silt stones, sandstones and cherts; representing shallow water carbonate platform. Mafic dykes and dolerite dated at ca. 1800 Ma intruded the Vempalle Formation (Chaudhuri et al., 2001; Saha & Patranabis, 2013), providing a robust constraint on the minimum age of the Cuddapah Basin.

The Chitravati Group represents a second cycle of sedimentation, and comprise mature sandstones of the unconformable Pulivenda (~90 m) and Gadinkota Quartzite (Saha & Patranabis, 2013). The Pulivenda Formation has 10 m thick pebbly sandstone conglomerate dominated by well sorted quartz-arenite deposited close to sea level (Collins et al., 2014; Joy et

al., 2015). The Srisalaim Formation represents a third cycle with depostion of widespread coastal-fluvial to shallow marine sandstone. The formation dominantly consists of >600 m of well sorted quartz arenite with a prominent m-scale cross bedding (Collins et al., 2014). The Srisalaim Formation overlies the granite gneiss basement and has a tectonic contact with the Nallamai Group. The Nallamai Group is thrust over the Kurnool and the Srisailam formations, and comprises arenites (Bairekonda Formation), shales, slates and phyllites interebedded with quartzites, chert and dolomites (Cumbum shales) (Collins et al., 2014).

The Kurnool Group represents the fourth cycle of sedimentation; each cycle of sedimentation represents a rifting phase followed by a stable subsidence stage when the basin evolved into one large epi- continental sea. The Kurnool Group unconformably overlies rocks of the Cuddapah Supergroup and the Srisailam Formation. The Cuddapah Supergroup was gently folded and faulted subsequent to deposition of the overlying Kurnool Group sediments (Joy et al., 2015). The Kurnool Group sediments (~450 m) outcrop in the separate Kurnool and Palnad sub-basins (Saha & Patranabis, 2013; Joy, et al., 2015). The Kurnool Group consists of >500 m of siliciclastic and carbonate sediments that grade from the basal alluvial diamond bearing Banganapalle Formation, through micritic carbonates of the Narji Limestone Formation, the Owk Shale Formation, the Panium Formation, and the Koilkuntala Formation to the uppermost Nandyal Shale Formation (Saha & Patranabis, 2013; Collins et al., 2014, Joy et al., 2015). Sediments of the Kurnool Group were deposited over different units of the Cuddapah Supergroup and are exposed in Khundair Valley in the west and Palnad area in the northwest.

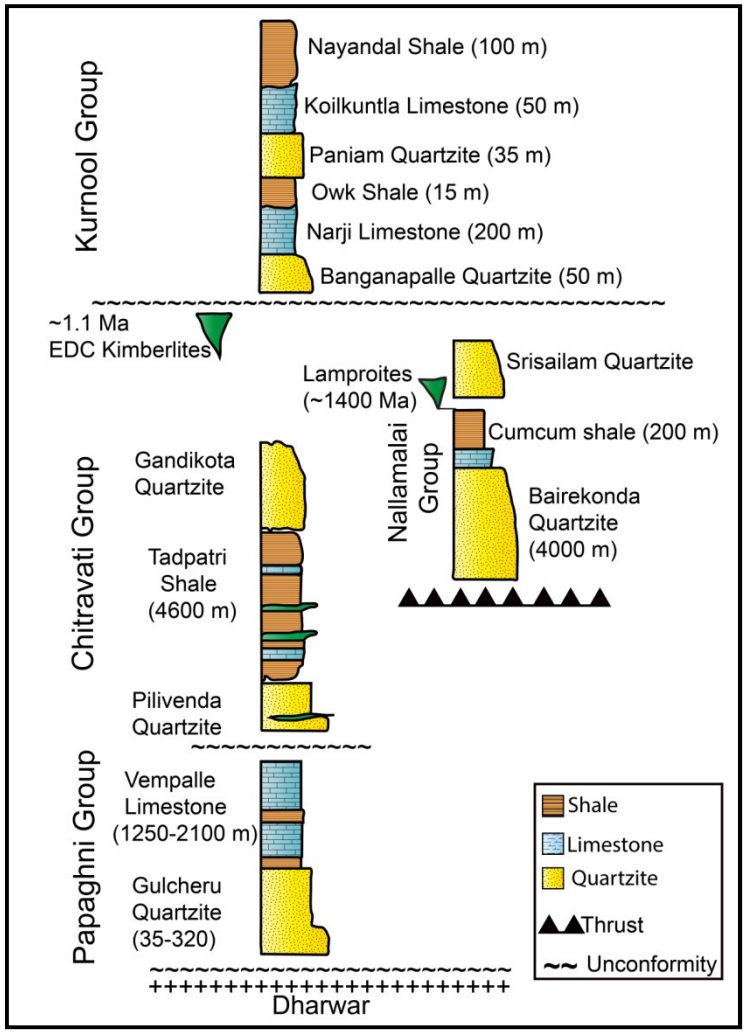

Figure 3: Stratigraphy of the oldest preserved Purana basin, the Cuddapah Basin of the EDC, south India, adapted and modified from Collins et al. (2014) and Joy et al. (2015).

The presence of helically coiled microfossil Obruchevella in the Owk Shale, was recorded by Sharma & Shukla (2012). The presence of worm burrows from the Narji Limestone together with Obruchevella suggest an Ediacaran age close to the Precambrian-Cambrian boundary for the Kurnool basin.

1.3 *Kimberlite and Lamproite magmatism of Peninsular India*

Kimberlites and related rocks occur in almost all of the cratonic segments of the Precambrian Indian Shield. According to Haggerty and Birkett (2004), India hosts the largest number of Proterozoic kimberlites and lamproites in the world. Occurrences are reported from the Bastar (Tokapal and Raipur kimberlites), Bundelkhand (Majhgawan lamproite) cratons and the Dharwar Craton with close to 100 kimberlite and lamproite discoveries (Kumar et al., 2007a; Fareeduddin

& Mitchell, 2012). Age determinations indicate that most of the kimberlites and lamproites in the Indian cratons intruded about 1.1-1.2 Ga and are therefore Mesoproterozoic (Chalapathi Rao et al., 2013, *for summary*).

On the Bastar Craton (BC), kimberlites are distributed in two fields, i.e. the diamondiferous Mainpur Kimberlite Field (MKF) and the Tokapal Kimberlite Field (non-diamondiferous). The MKF comprises six intrusions while the TKF has two intrusions. Although Group I (archetypal) kimberlites are known from Archaean cratons worldwide (Tappe et al., 2017), Group II kimberlites, which were thought to be restricted to the Kaapvaal Craton of southern Africa, are reported from the MKF of the Bastar Craton in central India (Chalapathi Rao et al., 2014)

Lehmann et al. (2010) discovered a Phanerozoic diamondiferous (Group II) kimberlite synchronous with the Deccan Traps in Central India (Bastar Craton). Their work demonstrated that the lithosphere in the Indian shield was thick at the end of the Cretaceous and therefore India's fast drift to the north before collision with Eurasia cannot be related to its lithospheric thinning during Gondwana break-up at 130 Ma, (Lehmann et al., 2010; Chalapathi Rao and Srivastava, 2012). The preserved crater facies Tokapal kimberlite (hosted in the Indravati Basin of Central India), is among the world's largest (Mainkar et al., 2004) crater-facies (>550 ha) and is exposed at the peneplained surface, in dug wells as well as stream cuttings and escavations. The pipe was classified as a kimberlite based on its notable similar petrographic characteristics as that of the crater-facies Fort a` la Corne (FALC) kimberlites in western, Canada (Chalapathi Rao et al., 2014). Lamproites on the BC are known from two areas, the Nuapada Lampoite Field (NLF) in Odisha and Khadka in the Chhattisgarh. The NLF comprises hypabyssal facies lamproite dykes at Amlidadar, Parkom and Darlimunda (Sahu et al., 2013).

Rio Tinto Exploration (2002) made new discoveries of kimberlites on the EDC in the WKF: a total of 15 kimberlites (including the recent pipe in Kalayandurga cluster) with 2 in the Rayalu cluster, 4 in Anumapalli cluster and 8 in the Gooty cluster. The Gooty cluster marks the first discovery of kimberlites within sediments of the Cuddapah Basin (Fareeduddin & Mitchell, 2012). Kimberlites and lamproites are restricted to the EDC and are found in four areas on the EDC: the Wajrakarur, Narayanpet, Krishna and Nallamai fields, with the majority of the intrusives being distributed around the Cuddapah Basin (Kumar et al., 2007a). These kimberlite and lamproite intrusions are known to occur prolifically during the development of the Purana basins, some occur within the basins and others outside. Interestingly, kimberlites in the EDC mainly crop out west of the Cuddapah Basin (Figure 1), whereas lamproites intruded the basin and its north-eastern margin (Kumar et al., 2007) close to the EGMB. Lamproites of the EDC

occur in the Nallamail Fold Belt of the Cuddapah Basin in two areas: the recently discovered Krishna Lamproite Field (KLF) and the Chelima Zangamrajupalle Lamproite fields (CZLF) (Balasubrahmanyan, 2006). The KLF comprises 30 lamproites that intrude the Archean granites and gneisses and occurs along the north eastern edge of the Cuddapah Basin. Osborne et al. (2011), cited that the Krishna Lamproites, which intrude the Cuddapah Basin, are thought to be some of the oldest lamproite occurrences globally and are also speculated to be the source of several of notable Indian diamonds (the Great Moghul with 900 cts, Regent with 410 cts, Orloof with 195 cts, Hope with 182 cts, Khoinoor with 793 cts). Lamproites from the EDC were dated using $^{40}Ar/Ar^{39}$ methods and results have yielded emplacement ages ranging from 1224 Ma to 1400 Ma. The Nallamalai lamproites (Chelima, Pachcherla, and Zangamrajupalle) occur as dykes within the 1.9 Ga Cuddapah Basin (Fareeduddin & Mitchell, 2012).

More than 30 kimberlites constitute the NKF, which comprises 4 clusters: the Kotakonda, Maddur, Narayanpet and the Bhima clusters. Kimberlites of the Maddur and Kotakonda clusters are emplaced in the younger biotite granites and are associated with major E-W faults and NE-SW trending minor tensional fractures, whereas the Narayanpet kimberlites are emplaced into the migmatitic gneiss. Twenty nine kimberlites are reported from the Bhima cluster. These kimberlites intrude mainly Archaean basement rocks of the younger Gneiss Complex, and amphibolites of the Paleoproterozoic Kolar-type greenstone belt near Gurmatkal (Fareeduddin and Mitchell, 2012). The Raichur kimberlite field is composed of two clusters, the Siddanpalle and the Undraldoddi kimberlites. The Siddanpalle kimberlites are emplaced in granitic rocks. Age determinations of kimberlites using 3 methods: 1). Rb-Sr phlogopite (Kumar et al., 1993; Chalapathi Rao et al., 1996; Kumar et al., 2007), 2.). Ar-Ar phlogopite (Osborne et al., 2011), 3). U-Pb perovskite (Kumar et al., 2007a, Chalapathi Rao et al., 2013), have demonstrated that kimberlites in all fields of the Eastern Dharwar Craton took place essentially during the Mesoproterozoic.

The Bundelkhand (Aravalli) Craton hosts the only diamond producing mine in India. The Majhgawan diamondiferous lamproite pipe near Panna is the first known primary source of diamonds in the world (Fareeduddin & Mitchell, 2012) and it is the only diamondiferous pipe presently mined in India. The emplacement of the Majhgawan lamproite pipe is reported to be ca. 1060 Ma, that is Mesoproterozoic in age (Chalapathi Rao, 2005). This lamproite pipe shares petrological and geochemical characteristics of kimberlite, orangeite and lamproite and has been regarded as a transitional/hybrid kimberlite-orangeite-lamproite rock type (Chalapathi Rao, 2005) with affinitities to ultramafic lamprophyres (cf. Tappe et al., 2005).

Radiometric ages of Indian kimberlites indicate episodic magmatism during the Mesoproterozoic at ca. 1110 Ma (Chalapathi Rao et al., 2013). This extensive Mesoproterozoic magmatism in India can be linked to the global event that produced many of the diamondiferous kimberlites and lamproites of South Africa, Australia and Canada-Greenland (Kumar et al., 2007a; Chalapathi et al., 2013; Wu et al., 2014; Tappe et al., 2007). For example, this includes the ~1150 Ma Premier kimberlite in South Africa, ~1.1-1.4 Ga lamproites of the North Atlantic Craton in Canada and Greenland (Scott-Smith, 1989; Tappe et al., 2007), and Mesoproterozoic kimberlite occurrences of the Lake Superior region of North America (Kumar et al., 2007a).

A temporal and spatial relationship has also been identified between kimberlites and related rocks and the large-volume continental flood basalts, which form Large Igneous Provinces (LIPs). At least 6 Phanerozoic and one Mesoproterozoic flood basalt eruptions are associated with kimberlites and related rock types (e.g. lamproites and lamprophyres) have been reported (Chalapathi Rao & Lehman, 2011). The overlap of ages between flood basalts and kimberlites are likely to reflect a cause and effect via mantle plume activity (Chalapathi Rao & Lehman, 2011). The involvement of mantle plumes in the genesis of 1.1 Ga Mesoproterozoic kimberlites of the DC has also been proposed (Kumar et al., 2007a; Chalapathi Rao and Lehmann, 2011, and references therein).

1.4 *Peninsluar India during Gondwana assembly and separation*

The assembly of Gondwana during the Ediacaran (~635-541 Ma) to Cambrian was envisaged by Collins et al. (2014) to be the result of collision and amalgamation of continental blocks along a number of incongruent orogenic belts. According to recent paleogeographic reconstructions, India only amalgamated with other Gondwana fragments during the Neoproterozoic or Cambrian. In these reconstructions, southern India and adjacent regions of Madagascar, Sri Lanka and Antarctica are located at the focal point of a number of separate orogenic belts that formed during collisions between India, Australia, Azania, Kalahari and Antarctica (Collins et al., 2014).

Madagascar, Sri Lanka and exposed regions of East Antarctica are cut by various orogenic belts related to Gondwana assembly (Pradhan et al., 2010). During the Mesoproterozoic the separation of the Paleoproterozoic supercontinent Columbia led to the almagamation of the Early Neoproterozoic landmass of Rodinia, whereby India was attached to Australia and East Antarctica, similar to its Gondwanan configuration (Pradhan et al., 2010). Between 1.1-1.0 Ga, (end of the Mesoproterozoic) is a significant time period for the initiation of the break up of the

Rodinia supercontinent followed by Gondwana assembly. The end of the Neoproterozoic era marks the break up of Rodinia and the nearly synchronous amalgamation of Gondwana at ca. 530 Ma. Eastern and western Gondwana break-up was signalled by the extrusion of the extensive Karoo and Ferrar basalts during the Early Jurassic, followed by the creation of Middle Jurassic oceanic crust in the Somali and Mozambique basin (Acharyya, 2000).

The break up of the greater Indo-Australian continent in phases led to the opening of the Indian Ocean and opening/closing of the Neo-Tethys ocean. This also produced continent-sized blocks like India, Australia, and smaller elongated marginal blocks (Lhasa, Indo-Burma-Andaman). During the formation of new rift basins and peri-cratonic shelf in the Cretaceous period, there were two episodes of extensive volcanism in the Indian subcontinent: the Rajmahal-Bengal Basin LIP at ca.117 Ma and the Deccan Traps at ca. 65 Ma.

Madagascar and East Africa lie to the west of Gondwana (Collins et al., 2014), whereas east Gondwana comprises India, Australia, East Antarctica and Sri Lanka (Pradhan et al., 2010; Acharyya, 2000). East Gondwana is widely assumed to have been a single coherent entity since the end of the Mesoproterozoic, but paleomagnetic data from the coeval Malani Igneous Suite of India and Mundine well dyke swarms of the Australia-Mawson continental block indicate that these were not united until after 750 Ma. Pradhan et al. (2010) argue based on their paleomagnetic data results that a coherent East Gondwana never existed at 750 Ma but explain the younger Pan-African belts between these cratons as a result of a final Ediacaran-age collision. The growing body of evidence for tectonism within some parts of East Gondwana show that East Gondwana may have not remained as a stable and rigid entity subsequent to ca. 1 Ga (Acharyya, 2000). The Eastern Gondwana Block escaped subsequent Neoproterozoic and Pan-African break-up and orogenesis, which are important in the Afro-South American West Gondwana (Acharyya, 2000). Subsequently, India and Seychelles which are part of Greater India drifted NNE away from Madagascar, and finally separated from one another over the Reunion hotspot that produced the massive Deccan Traps at the K–T boundary (Torsvik, 1998).

The peripheral parts of the Indian Mosaic are mainly affected by the Late Neoproterozoic (1.0-0.85 Ga) and the Pan- African (0.6 -0.45 Ga) thermal reactivations, felsic magmatism and crustal additions with little deformation (Acharyya, 2000). A thermal reworking occurred throughout East Gondwana notably in the Eastern Ghats and also in the South Indian granulite belts, Sri Lanka and Rayner and Napier Complexes of Antarctica at ca. 1.0 Ga. (Acharyya, 2000). Collins et al. (2014) suggested that southern India was the leading vertex of India as it collided with other Gondwana continents during the Ediacaran – Cambrian. The South Granulite

Terrain of southern India, as opposed to the rest of the Indian continent, records tectono-metamporphic reactivation and granulite formation at 600-450 Ma coinciding with Pan-African activity (Acharyya, 2000).

Kumar et al. (2007b), in their study to determine lithospheric thickness of Gondwana fragments using seismic methods, discovered that the lithosphere is much thinner beneath southern India compared with the cratons of South Africa, Antarctica, and Australia. The Indian lithosphere has a current thicknes of ~100 km or less. Old and stable continental regions are generally known to be underlain by a thick lithosphere (>150 km), demonstrated by the presence of diamondiferous areas within their interiors. Therefore, lithospheric thickness sufficient to extend into the diamond stability field must have existed beneath the Indian shield before the breakup of Gondwana. Figure 4 shows the position of India in Gondwana and current lithospheric thicknesses of the different continents according to Kumar et al. (2007b).

1.5 *Previous AFT and AHe studies of the Dharwar Craton*

Early studies of denudation history in peninsular India are mostly based on Apatite Fission Track (AFT) analysis (Gunnell et al., 2003; Sahu et al., 2013; Mandal et al., 2015). Several AFT studies have been carried out to the west of the EDC to investigate the thermo-tectonic evolution of the Indian passive margin. Gunnel et al (2003) studied the denudation history of the continental margin of western peninsular India since the early Mesozoic reconciling apatite fission-track data with geomorphology. In his study he suggested extremely low Mesozoic denudation rates and attributed the increased denudation rates to known major events (i.e. 130 Ma: rifting with Antarctica, 80 Ma: rifting with Madagascar).

Another study was conducted by Sahu et al. (2013); this study focused on the denudation history of Eastern peninsular from AFT analysis, linking possible plume-related uplift and the sedimentary record. In their study they suggested accelerated cooling during the Late Cretaceous, which translated to 0.5 – 2 km of denudation in this period. The fact that AFT alone cannot provide reliable constraints on the cooling below 60-50 ºC is a perfect example why it is necessary to find other complementary dating techniques, such as (U-Th)/He. Apatite (U-Th)/He thermochronology is sensitive to temperatures between 90-30ºC (Farley, 2005; Flowers et al., 2009, Shuster et al., 2006). The sensitivity of the AHe dating method to low temperature makes it suitable to quantify the timing, magnitude and the extent of shallow deposition and erosion episode in passive margins which in turn help to reconstruct the landscape history (Ault et al.,

2013; Mandal et al., 2015). A recent study by Mandal et al. (2015), studied Phanerozoic surface history of southern peninsula India from apatite (U-Th)/He, mean ages ranged from 38 to 364 Ma, with older ages in the Deccan Plateau and younger ages in Palghat Gap region. They suggest an erosion of 1-1.5 km along the western coastal plain.

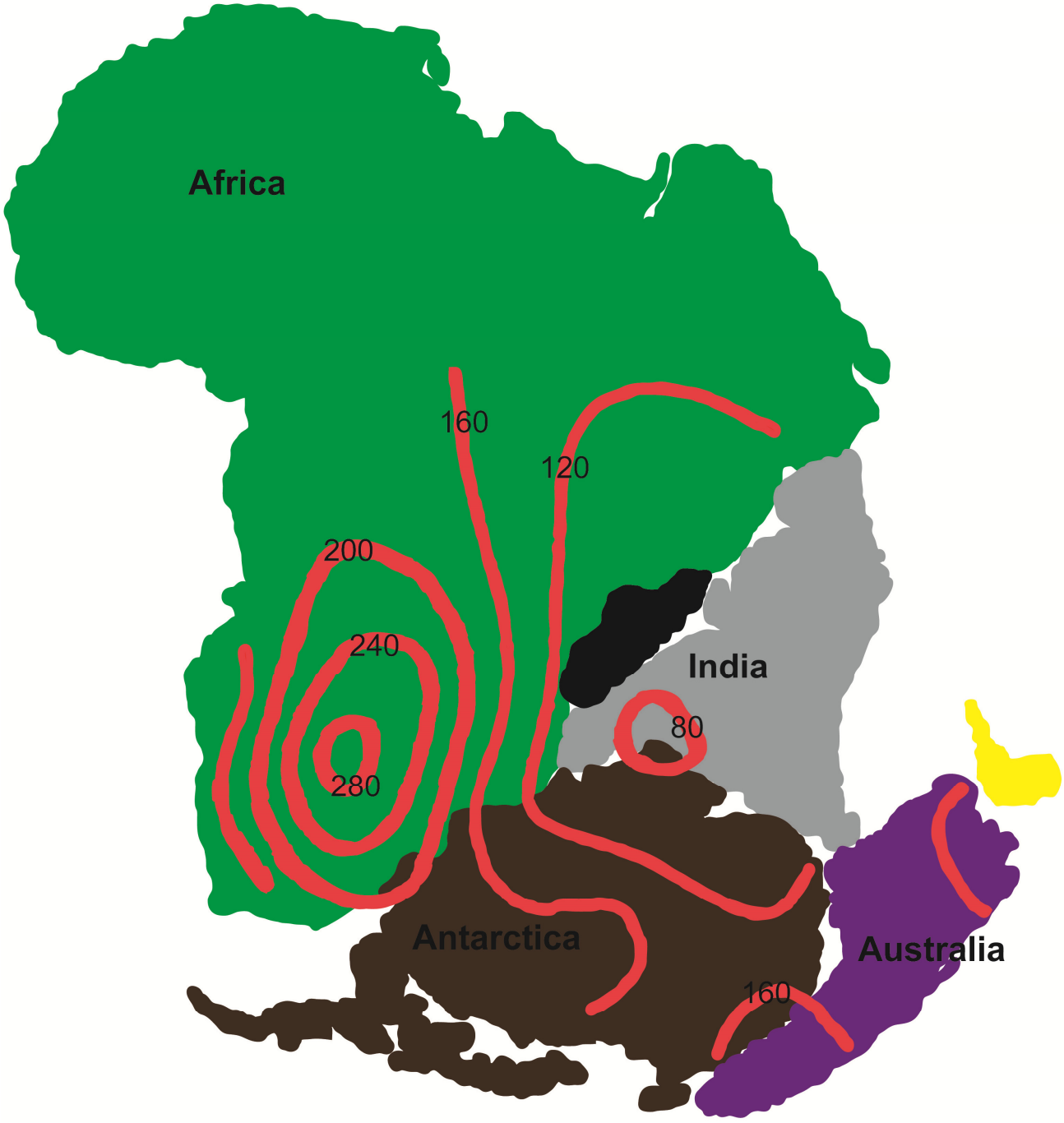

Figure 4: The Indian tectonic plate within Gondwana during Permian times. Contours show present day continental lithospheric thickness in km. Map adapted from Kumar et al. (2007b).

2 Methods

2.1 *Sampling*

Samples used in this study were collected from the Dharwar Craton of southern India, comprising 3 dark grey to black, visibly fresh hypabyssal magmatic kimberlite samples. These samples were collected by Dr. S. Tappe during the 10th International Kimberlite Conference held in Bangalore (India) in 2012. It should be noted however that approximately 47 samples including kimberlites and lamproites from the Dharwar Craton and other Indian cratons had been processed during this MSc study, but the majority of samples yielded only small apatite grains below the threshold size (see Appendix C for detailed explanation) for thermochronology applications. Appendix A contains petrographic descriptions for all samples screened in this study.

2.2 *Petrography, QEMSCAN and EPMA analysis*

Petrographic analysis involved observations of the samples using an Olympus BX51 optical microscope enhanced with both reflected and transmitted light, and a Zeiss Stereo Microscope (Discovery V12). In this section, only samples used for thermochronology are petrographically documented including images. Petrological and geochemical studies of kimberlites from the WKF in Anantapur, the NKF in Mahbubnagar, and RKF in Karnataka revealed that these kimberlite occurrences represent remnant root zones of diatremes or pipes; i.e. they have typical hypabyssal coherent magmatic textures (Biswas, 2007).

Three thin sections were analysed by EPMA (Electron Probe Micro Analyser) for major and minor element concentrations of petrogenetically important mineral phases such as olivine, spinel, phlogopite and apatite. In addition, back-scattered electron (BSE) images were taken using the EPMA. One of our aims was to clarify whether the selected rocks are bona fide kimberlites or have a lamprophyric to lamproitic affinity (Appendix A2). The main goal was to specifically target apatite in the kimberlite groundmass to evaluate the absence or presence of compositional zoning, which has important implications for thermochronology. EPMA data acquisition was performed at Rhodes University (Department of Geology), using a Jeol JXA 8230 Superprobe and at the University of Johannesburg (Department of Geology) using a Cameca SX100 instrument. Both EPMA instruments are equipped with four WD spectrometers, and mixtures of synthetic and natural mineral standards were used for calibration. The analytical conditions employed were: an acceleration voltage of 15 kV and a probe current of 20 nA for

major elements; counting times were 10 seconds on the peak and 5 seconds on the background. The beam size was <1 micron and the standards used for measuring the characteristic Kα radiations were natural minerals and synthetic compounds. The Phi-Rho-Z matrix correction method was used for quantification. These analyses were focused only on apatite; other minerals were analysed to confirm rock type (see Appendix B).

Further petrographic observations and semi-quantitative analyses to determine modal mineral abundances were made using the QEMSCAN method (Quantitative Evaluation of Materials by Scanning Electron Microscopy). QEMSCAN is a rapid chemical data collection system which utilizes a combination of BSE images and EDS (Energy Dispersive Spectrometry) analysis to generate an image of a polished sample based on its chemical composition. Images are then processed off-line to provide information on modal mineral abundances, grain size distributions, and grain contact relationships. We acquired Bulk Modal Mineralogy (BMA) for both sample CC-5 and SK-2 including field maps showing grain and particle sizes.

The detailed QEMSCAN analysis established the percentage of each major and minor mineral phase in the hypabyssal kimberlite samples QEMSCAN analysis was performed at the Society of Geological Sciences (Johannesburg, South Africa), using the EVO Scanning Electron Microscope (SEM) equipped with 4 liquid nitrogen cooled SiLi Energy Dispersive Spectrometry (EDS) detectors. The detectors were calibrated using a Cu standard. A field map was created for two samples CC-5 and SK-2, and 214 and 218 fields were mapped, respectively. Field size was 1000 µm at magnification of 71X and each field was 1000 µm along the X-axis and the Y-axis with a 5 µm pixel and the point spacing of 5 µm. The electron beam was accelerated at 25 kV, with a specimen current of 5 nA, the spot size was 5 µm (measured at 4.88 µm) with an x-ray count of 1000. The Back Scatter Electron (BSE) grey scale calibration used Au at 232, Cu at 130 and quartz at 42. QEMSCAN analysis established the percentage of each major and minor mineral phase in the samples.

2.3 *Low-Temperature (U-Th)/He Thermochronology*

Kimberlite samples were selected for apatite (U-Th)/He analysis based on the identification of groundmass apatite crystals using polished thin sections under a petrographic microscope. Typically, a coarser grained kimberlite matrix contains more abundant and larger apatite crystals. Samples were then prepared for apatite grain liberation and isolation (see Appendix C) for thermochronology analysis. Here we explain how the techniques work.

The (U-Th)/He technique was developed by Ernest Rutherford in 1906. The decay of U and Th to helium was one of the earliest techniques used by geochronologist to determine the ages of rocks (Zeitler et al., 1987). (U-Th)/He dating is based on the ingrowth of α particles (^{4}He nuclei) produced by U and Th series decay (Ehlers & Farley, 2003). During secular equilibrium the series of decay of short-lived radionuclides of ^{238}U, ^{235}U and ^{232}Th and α decay of ^{147}Sm produces 8, 7, and 6 α particles (Farley & Stockli, 2002). Under conditions of secular equilibrium amongst the short-lived actinide daughters, the rate of ^{4}He ingrowth is:

$d^4He/dt = 8\,\lambda_{238}\,{}^{238}U + 7\,\lambda_{235}\,{}^{235}U + 6\,\lambda_{232}\,{}^{232}Th + \lambda_{147}\,{}^{147}Sm$ ……………………………..(1)

Where d^4He/dt is the change in He over time and all the λs are the decay constant ($\lambda_{238} = 1.551 \times 10^{-10}\ yr^{-1,}$ $\lambda_{235} = 9.849 \times 10^{-10}\ yr^{-1}$, $\lambda_{232} = 4.948 \times 10^{-10}\ yr^{-1)}$. By measuring U, Th, and He content, and assuming that an initial He content of zero in the dated grain; apparent t can be calculated (ignoring Sm, contribution of ^{4}He from ^{147} Sm is small compared to those of from U and Th) from the equation:

$^4He = 8\,{}^{238}U\,(e\,\lambda^{\,238t-1}) + 7\,{}^{238}U/137.88\,(e^{\lambda\,235t-1}) + 6\,{}^{232}Th\,(e^{\lambda\,232t-1})$……………………….. (2)
where the factor of 137.88 is the ^{238}U/^{235}U ratio of natural uranium (Farley & Stockli, 2002).

Application of low-temperature thermochronometry is a powerful technique for constraining thermal histories of samples as they pass through isotherms in the upper crust (see Appendix C for (U-Th)/He technique description and sample preparations). Apatite was separated using conventional crushing, milling, and sieving, magnetic and heavy liquids techniques. Magnetic and heavy liquid techniques were performed at the University of Colorado in Boulder; U.S.A Minerals were initially separated using a hand-magnet by using their magnetic properties, allowing for refinement of the mineral concentrate and removal of minerals with different degrees of magnetic susceptibility (e.g. magnetite). Frantz magnetic separation was done to further separate the magnetic and non-magnetic minerals. The Frantz magnet was run starting with a 20° table tilt and set at ~1.0A for most samples, with the highest amperage set at 1.4A at a 15° table tilt. Apatite remains in the non-magnetic fraction after passing through the Frantz on the highest power setting.

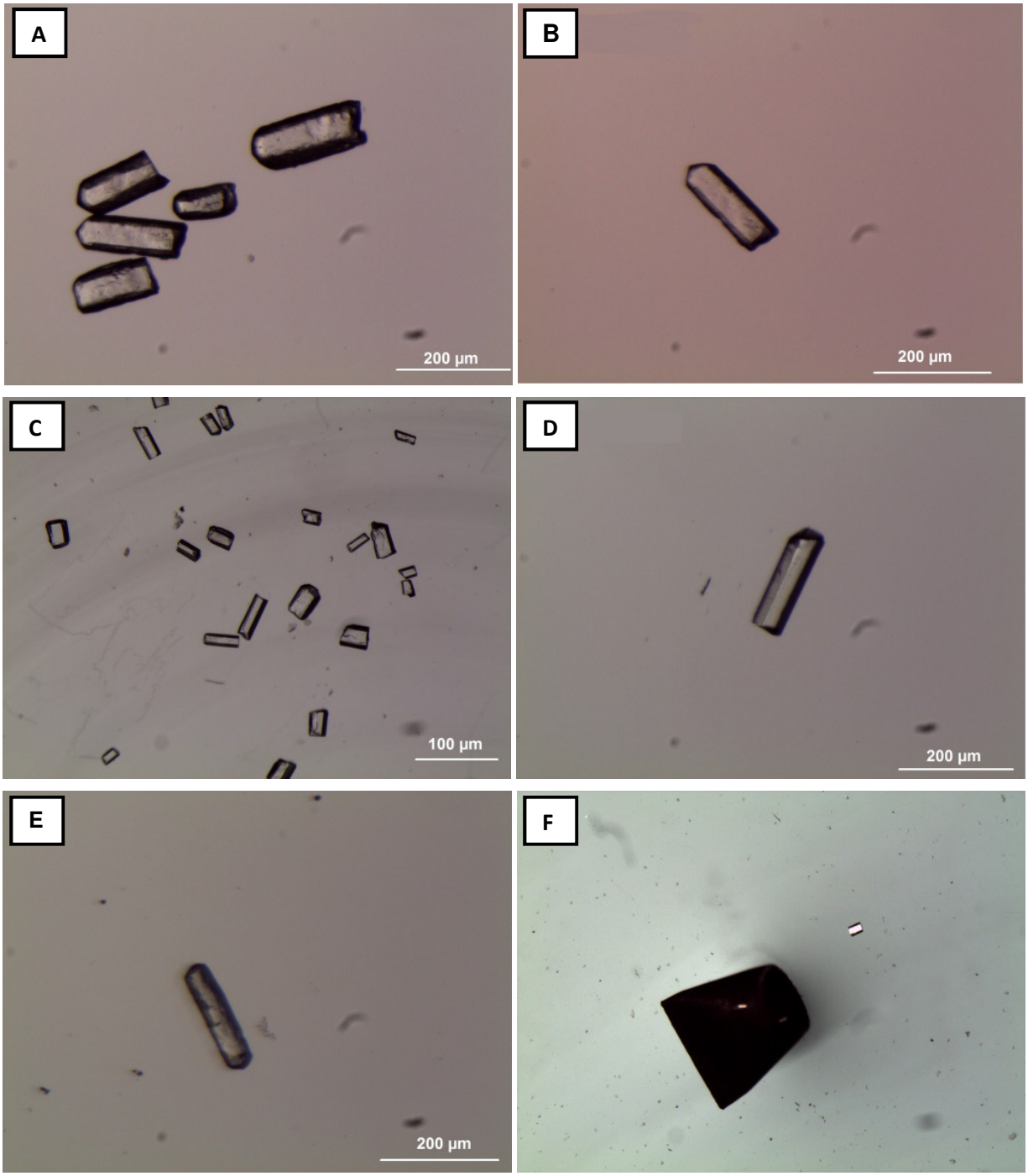

Figure 5: Grain morphologies and size of isolated apatite grains for the Wajrakarur kimberlite field. (a) Shows typical prismatic habits of apatites from sample SK-2 and (b) shows an individual grain before packaging. (b) Shows apatite grains from sample CC-5, which are mostly broken and smaller than those of SK-2, (d) shows the acceptable shape and size to be used for thermochronology analysis. (e) Shows a single grain from sample SK-1; apatites from this sample are generally smaller (both in length and width) in comparison to the CC-5 and SK-2 apatites. (f) Shows an image of a packaged apatite grain in a Pt tube.

Density (heavy liquid) separations are performed to recover apatite grains using the non-magnetic fractions from the thermodynamic isolator (Frantz magnet). Bromoform ($CHBr_3$) was used as the heavy liquid with a density of 2.89 g/cm^3 (Suzzman, 1967). This step involves the

use of a separatory funnel, test tubes, conical flask, centrifuge tubes (to prevent contamination when transferring different samples), test-tube rack**,** clamps, acetone, filter papers and the non-magnetic separate of the sample. Approximately 8ml of bromoform was then poured into a test-tube. The non-magnetic sample fraction was then poured into the test-tube and gently shaken to ensure proper sample propagation. Light minerals such as micas (2.65 g/cm^3) float on top of the bromoform liquid, while heavy minerals such as apatite (3.19 g/cm^3) and zircon (4.65 g/cm^3) sink to the bottom of the test-tube. The light and the heavy minerals were then packaged in small tubes and clearly labelled. Mineral separates were then packaged in small tubes and clearly labelled.

Mineral picking in ethanol was done using a petri dish under a binocular microscope enhanced with both transmitted and reflected light. Euhedral, inclusion-free apatite grains were hand selected using tweezers under the microscope; whilst irregular anhedral to subhedral shapes were discarded, due to the requirements of (U-Th/He) thermochronometry discussed in Section 3.2. Apatite grains were examined for mineral inclusions under crossed polarizers. When the apatite crystals are taken to extinction, tiny inclusions of phases such as zircon stand out on rotation of the stage. Grain dimensions were measured from photographs (Figure 5) prior to packaging in individual Pt tubes for analysis. Measured apatite grain sizes in our samples have a spherical radius (rs- The radius of a sphere with an equivalent surface to volume ratio a crystal) ranging from 54-116 µm. Figure 5 shows apatites from kimberlite sample SK-2 with an ideal habit and size.

The analytical helium extraction techniques were performed at the University of Colorado; grains were heated in Pt tubes at 6A for 5 minutes to extract radiogenic ^{4}He. Extracted He was spiked with ^{3}He, purified using gettering methods, and measured on a quadrupole mass spectrometer. All degassed apatites were then retrieved and dissolved in HNO_3 at ~90 °C for 1 hour with a ^{235}U-^{230}Th-^{145}Nd-^{51}V tracer solution added. Dissolved samples were measured for U, Th, and Sm on a Thermo-Finnigan Element2 sector field inductively coupled plasma mass spectrometry (ICP-MS). Grain masses were calculated using the measured dimensions of the crystal Fragments of the Durango apatite were analyzed as a standard by the same procedures along with our samples. The alpha-ejection correction (Ft) of Farley et al. (2002) was applied to all grains (Table 5).

A total of 13 individual apatite grains and 2 aliquot analyses were run, After the analysis, grains with minimum blank U and low eU were eliminated, due to probable He injection problems; leaving only a total of 10 grains. Two apatite grains are from kimberlite sample SK-1; three

grains are from sample SK-2 (Siddanpalle kimberlite cluster in the RKF), and 5 grains are from sample CC-5 of the Chigicherla kimberlite cluster in the WKF. Effective uranium concentration is a parameter that weighs the decay of two parents for their α-productivity, and it is computed as [U] + 0.235 [Th]. At temperatures low enough low enough for radiation damage to accumulate, according to the He trapping method (HeTM), an apatite with higher eU will accumulate more damage traps and will develop a higher He closure temperature than an apatite with low eU that will accumulate fewer traps (Flowers et al., 2009).

2.4 *Time-Temperature Modelling*

A large number of thermal histories can satisfy any given AHe age, so thermal history simulation software was used to limit the possible thermal histories to those which best replicate the data and are consistent with reasonable geologic constraints. The HeFTy software program (Ketcham, 2005) was applied to model the (U-Th)/He ages. It incorporates inverse modelling and radiation damage accumulation and annealing model (RDAAM) corrections for apatite He diffusion kinetics (Flowers et al., 2009). Thermal history information can be linked to datasets to infer geological processes that are responsible for producing the observed thermal history paths. HeFTy generates random t-T paths in compliance to a defined thermal history and finds good and acceptable fit thermal histories that simultaneously satisfy the date, eU (effective uranium concentration) and equivalent spherical radius for each sample (Ketcham, 2005).

Constraints are represented as user-defined t-T boxes/points within the model through which thermal scenarios must pass. These constraints assume starting conditions such as emplacement ages, geologic constraints or thermal system conditions (e.g. Aapatite Fission Track data). Additional information regarding good versus acceptable data fits and goodness of fits are explained by Ketcham (2005).

Apatite (U-Th)/He data are listed in Table 5 with He ages and isotopic ratios. The modelled paths in each t-T box are assumed to be monotonic (i.e., heating or cooling only), and the paths were simulated for 10,000 random Monte Carlo inversion runs. For modelling with HeFTy, input parameters include: (i) the average raw mean AHe ages (with uncertainty), (ii) the U, Th and Sm contents of the respective apatite grain fractions, and (iii) the average spherical radius (rs) of all averaged grains per sample. Samples SK-1 and SK-2 from the RKF were modelled together as they come from the same kimberlite cluster and are only ~1 km apart

Conditions for using HeFTy: In general, all the t-T histories should begin at sufficiently high temperatures to ensure that there is total annealing of the apatite grains (i.e., no fission tracks

present) and/or no retained He as an initial condition. The final constraint should correspond to the temperature at which the sample was collected, i.e. an average annual surface temperature. Another constraint might correspond to the depositional time and assumed temperature of the sedimentary sequence from which the sample was obtained (Ketcham, 2005).

2.5 *Plate Tectonic Modelling*

In the past decade, developments of numerous tools for tectonic reconstructions have emerged. This project utilized GPlates software, which is an open-source, cross platform, Geographic Information System that offers a suite of integrated, interactive functionality for geological studies. This software allows users from different disciplines to work with plate tectonic models and be able to relate these models to their own data sets (Williams et al., 2012). GPlates was utilized in order to conduct the paleo reconstructions for Gondwana breakup focusing on the Indian plate as it drifted away from the African plate. The plate reconstructions are shown in Figure 14.

3 Results

3.1 *Petrography: Mineralogy and Chemistry*

This section focuses on the descriptions of samples from the Eastern Dharwar Craton, the Chigicherla and the Sindanpalle kimberlites. The petrographic studies on these samples were done using an optical microscope, SEM and the Electron Microprobe Analyser. Appendix A is a summary table of the petrographic description and classification (table A2) of the studied EDC kimberlites.

3.1.1 Chigicherla Kimberlites

Kimberlites of the Chigicherla cluster are characterized by autoliths with a black groundmass that is likely made up of clay minerals (e.g., brucite). The inequigranular texture is imparted by olivine macrocrysts and microphenocrysts set in a fine groundmass. Phenocrystal and microphenocrystal olivine is abundant and commonly serpentinized or completely pseudomorphed by serpentine. Fresh olivines occur within the autolith portion of the kimberlite rock. Olivines outside the autoliths are highly serpentinized. Kimberlite CC-5 has an even groundmass distribution (Figure 7C) of olivine, serpentine, calcite, carbonated olivine, perovskite, ilmenite and other opaque minerals. In CC-5, apatite crystals occur as radial (acicular) sprays (Figure 6 a, b; Figure 6a, c), Mitchell (1995) stated that apatites with acicular habits are indicative of crystallization during rapid quenching of magma, i.e. rapid growth. Apatite is a late crystallizing groundmass mineral and it occurs in quantities ranging from less than 1vol% to 10vol%. Apatite is abundant in the carbonate rich portions of the groundmass and in calcite rich segregations (Mitchell, 1995; Mitchell, 2008). Apatites in CC-5 kimberlite occur in calcite rich portions of the groundmass (Figure 6a, d). Apatite crystals in this sample are relatively large with grain sizes of up to 200 µm.

3.1.2 Siddanpalle Kimberlites

Siddanpalle (SK-1) kimberlite is calcite rich, with two generations of olivine. Most of the olivines are serpentinized and some olivine grains are carbonated (Figure 6b; Figure 7b). Perovskite, olivine, serpentine, spinel, rutile and apatite form part of the groundmass minerals in sample

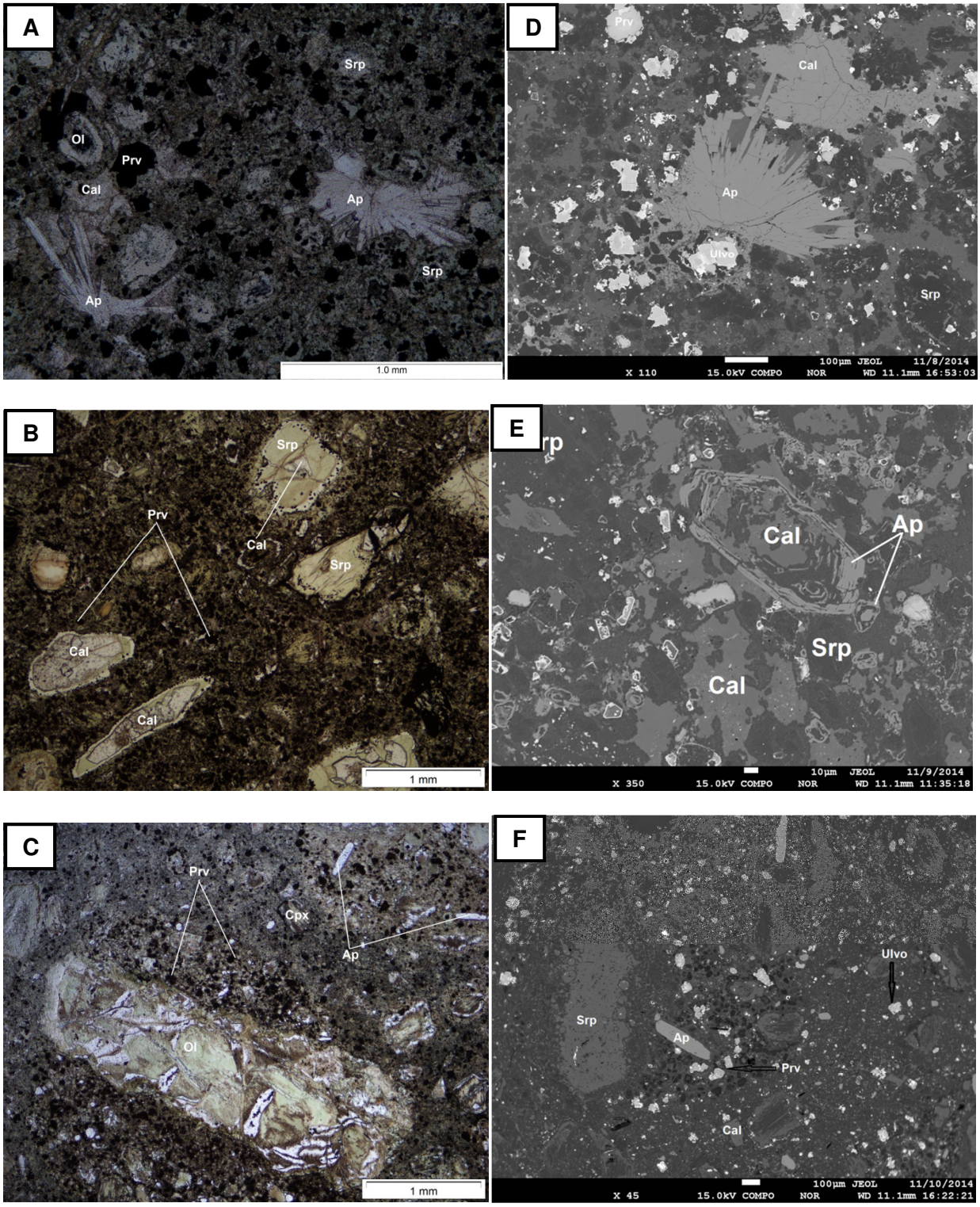

Figure 6: Petrographic properties of the EDC kimberlites. (a-c) show photomicrographs and (d-f) BSE images of samples CC-5, SK-1 and SK-2. (a) & (d) Sample CC-5 shows typical acicular apatite grains forming radiating sprays set in calcite (Cal) rich portions of the groundmass. (b) & (e) show SK-1 sample with macrocrysts of serpentinized olivine grains set in a fine groundmass of serpentine (srp) and perovskite (prv). Apatite (Ap) surrounds earlier formed olivine grains. (c) & (f) Sample SK-2 showing prismatic Ap embedded in serpentine. All samples show inequigranular textures with serpentinized olivines, in a Srp and Cal and spinel groundmass. Note the identical gray scale of all the perovskite grains depicting the lack of compositional zoning.

SK-1. In this sample apatite and olivine is commonly replaced by later forming calcite resulting in the formation of resorbed crystals. Apatites in the SK-1 sample are small with less than or close to 10 µm in size. Kimberlite SK-2 is a fine grained carbonate rich rock (Figure 7b), with macrocrysts of olivine that are typically surrounded by perovskite crystals forming a necklace texture. Backscattered images depict two modes of occurrence of perovskite, as discrete grains in SK-2 and as necklaces around phenocrysts/macrocrysts of olivine (SK-1). Perovskite is a common phase in the Sidanpalle kimberlites samples. It forms at the final stages of magmatic crystallization (Tappe and Simonetti, 2012) and occurs either as discrete grains dispersed throughout the groundmass (Figure. 6d), or as necklaces surrounding the earlier formed olivine grains (Figure. 6f). Perovskite postdates minerals of the macrocryst suites and crystals nearly simultaneous with groundmass spinel belong to the magnesian–ulvospinel series. Perovskite precipitates later than the macrocrystal spinel (Al-Mg chromite) and nearly simultaneous with the reaction of Fe-rich spinel. Groundmass minerals in sample SK-2 include olivine, abundant perovskite, calcite, rutile and clinopyroxene (diopside). Stubby, prismatic apatite (Figure 5a, 6c) with sizes greater than 200 µm also forms part of the kimberlite groundmass.

3.1.3 Mineral Chemistry

Compositions of olivine (Appendix, B2), perovskite (Appendix, B1), and ilmenite (Appendix, B4) are shown in Appendix B. All of the olivines in sample SK-1 and SK-2 are highly serpentinized, therefore only serpentine (Appendix, B3) compositions are shown for these samples in Appendix B.

Microprobe analyses of olivine for the CC-5 kimberlite reveal low CaO (0.02 wt.%), MnO (0.03 wt.%), Cr_20_3 (0.02 wt.%), Al_2O_3 (0.01) and TiO_2 (0.01 wt.%). NiO content averages 0.10 wt. %. Forsterite content varies from 0.80-0.94 in sample CC-5 (Appendix B, Figure1). The relatively low Fo content between 88 to 90 is indicative of micropehnocrystal olivine, and combined with a low NiO content (0.10) classifies the microphenocrystal olivine as kimberlitic. This is supported by petrographic results indicating a hypabyssal kimberlite (HK). SK-1 and SK-2 are highly serpentinized, therefore only serpentine (Appendix, B3) compositions are shown for these samples in Appendix B.

Spinel occurs as euhedral to subhedral grains. Groundmass olivines exhibit corrosion on their rims and larger crystals. The Cr spinel grains in sample CC-5 are rich in MgO with contents close to 16 wt.%. Spinel compositions for sample CC-5 follow both the magmatic trend 1 (magnesian ulvospinel trend) and trend 2 (after Mitchell, 1986; see also Tappe et al., 2014), see appendix B (Figure 2b). The Cr spinel compositions in sample SK-1 are Mg-rich with content of

up to 15 wt.% MgO. The Cr/(Cr +Al) ratios range from 0.72-0.78, the Cr-spinel compositions for sample SK-2 have elevated Cr/(Cr+Al) ratios of up to 0.98. These are characteristics of spinel compositions from Group I kimberlites and evolved calcite kimberlites (Mitchell, 1995). The SK-1 groundmass spinels show limited Ti/ (Ti+Cr+Al) that is restricted to ~0.6. These spinels fall between the magnesian ulvöspinel and titanomagnetite trend. Also, the SK-2 spinel compositions have Ti/(Ti+Cr+Al) ratios (Appendix B, Figure 2a) restricted to above 0.8 and also fall between the two kimberlite trends. Although this feature is uncommon among Group- I kimberlites worldwide, it has been described from numerous hypabyssal kimberlites of the Superior Craton in eastern Canada and ultramafic lamprophyres (UML) of the Greenland-Labrador Diamond Province (Tappe et al.; 2014, and references therein). The groundmass spinel compositions for kimberlites from the DC are poor in Al and Mg in comparison to those of Southern African magmatic kimberlites (Scott-Smith & Skinner, 1984).

Ilmenite macrocrysts are present in the SK-2 kimberlite. Ilmenite occurs as discrete grains up to 3 cm in diameter. Microprobe analyses for the SK-2 kimberlite have compositions typical for kimberlitic ilmenite; from 44.4- 54.4 wt.% TiO_2, 6.9-15.08 wt.% MgO (i.e. an elevated geikielite component, picro-ilmenite), 27.08-37.25 wt.% FeO. The MnO concentrations are also elevated between 0.27-9.13 wt.% Ilmenite compositions of the SK-2 kimberlite are plotted on the ternary system of $FeTiO_3$ (ilmenite) - $MnTiO_3$ (pyrophanite) -$MgTiO_3$ (geikielite), indicative of their kimberlitic nature (Appendix B, Figure 3). Furthermore, groundmass ilmenites from SK-2 fall on the right side of the compositional divide in MgO-TiO_2 space (Wyatt et al., 2004), which is typical for on-craton kimberlite occurrences (Appendix B, Figure 4). This confirms that our kimberlites are indeed on-craton kimberlites. Perovskites for sample CC-5 and sample SK-1 show little variation with CaO content of ~38.4 wt.% and TiO_2 of around ~55 wt.% (Table B1). Total iron (FeO*) ranges from 0.01-1.41 wt.% FeO in sample CC-5, and from 0.83-1.08 wt. % FeO in sample SK-1. This is similar to FeO contents of kimberlitic perovskite elsewhere (Mitchell, 1986; Tappe and Simonetti, 2012; Beyer et al., 2013), indicating little Fe substitution in the Ti site.

3.2 *Groundmass apatite morphologies and compositions*

Apatites in these samples (CC-5, SK-1 & SK-2) are set within the kimberlite groundmass (Figure 7). Apatite grains showed differing crystal habits and were generally anhedral to subhedral with minor euhedral occurrences. Different sizes of apatite grains were observed, ranging from 10-300 µm. Apatites from sample SK-1, and SK-2 are smaller than those from CC-5. There is no evidence of zoning observed, either in BSE images or variation in the composition of individual apatite grains. Furthermore, there is little variation in the composition of apatite grains within a single sample.

Mineral chemistry reveals that apatites analysed in this study are fluorapatite with fluorine ranging from 1.2-4 wt.%. Kimberlite CC-5 shows higher F content in apatite from 2.2 to 4.3 wt. % F. Calcium content ranges from 50-56 wt.% CaO. Phosphorus content ranges from 36-45 wt.% P_2O_5 with an appreciable amount of silica (up to 1.5 wt.% SiO_2) substituting for phosphorus in sample SK-2 (Table 2 & 3). Apatites in this study are clearly magmatic in origin with fluorine dominating over chlorine (<0.05 wt.% Cl), as is typical for most magmatic rocks (Marks et al., 2012).

Figure 8 shows the compositions of apatites from sample CC-5 and SK-2. The SrO content for SK-1 apatites is below the detection limit by EPMA. Sample CC-5 has higher SrO contents in apatites ranging from 0.6-1.7 wt.% in comparison to apatites from sample SK-2, which have low SrO content (0.01-0.52 wt.% SrO). The phosphorus content for sample SK-2 and sample CC-5 are within range from 39-43 wt.%. The CaO content for both sample SK-2 and sample CC-5 range between 53-56 wt.% CaO.

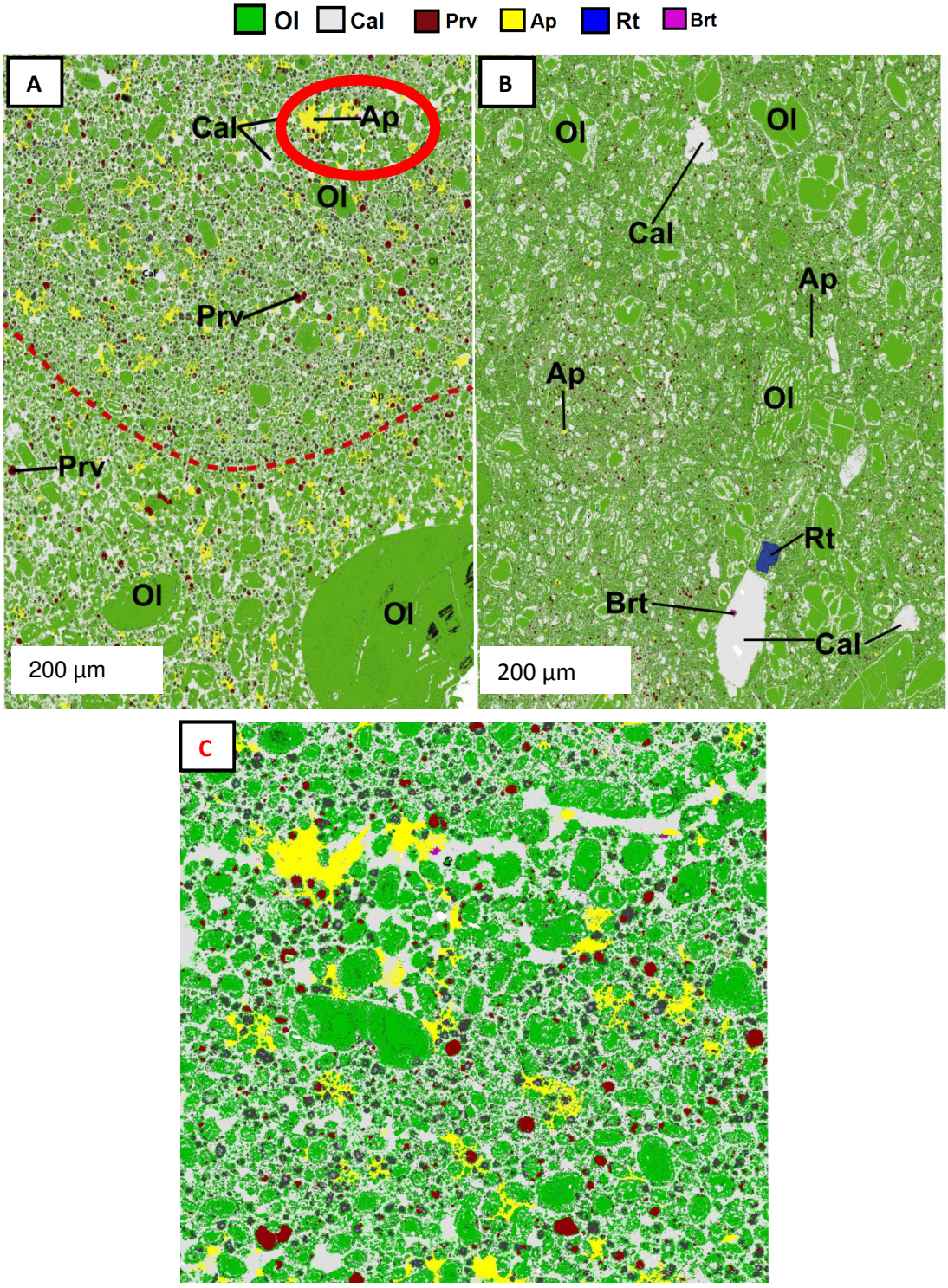

Figure 7: Representative QEMSCAN (BSE) images for the EDC kimberlites (a) CC-5, showing the inequigranuar texture, above the red curve is the autolith, note the difference in grain size (grain sizes in the autolith are smaller than those of the later solidied rock). (c) shows the detailed section of the encircled part of the CC-5 kimberlite, apatite is present as an acicular mineral set in an interstitial calcite matrix. (b) SK-2, shows the textural positions of the groundmass apatite (Ap) grains, the sample is calcite (Cal) rich, with Cal rimming around olivine (Ol) grains Minor ilmenite, barite (Brt) and abundant perovskite (Prv) occur as groundmass minerals.

As stated above, apatites in the CC-5 kimberlite occur as acicular grains (of about 200 µm length, Fig 6a, C), embedded in the groundmass of serpentine, calcite and opaque minerals (likely spinel and ilmenite). Sample SK-2 shows euhedral inclusion free apatite grains (Fig 5a) of about 300 µm length; these are embedded in a serpentine groundmass. Apatites from sample SK-1 are very small (less than 10 µm, Fig 5e) and appear to be interstitial or rimming around other groundmass minerals like calcite and serpentine. Based on modal analysis, olivine was the first mineral to crystallize, followed by calcite, serpentine, phlogopite, ilmenite, apatite and later forming perovskite (see also Tappe et al., 2017). The majority of silicates in these kimberlites have been subjected to carbonatization and serpentinization. Therefore, the compositions of the groundmass oxides played a crucial role in magma type characterisation.

3.3 *Apatite (U-Th)/He Data*

Apatites from kimberlite CC-5 have well developed euhedral crystal faces with no detectable inclusions under the microscope. Most of the grains are broken in half; however, it was possible to infer the original shape of these grains. Apatites from kimberlite SK-2 are long, prismatic and normally fractured with uneven anhedral surfaces (Fig 5a). Although fragmentation can affect AHe ages for certain thermal histories, fragmentation effects are far less significant than the influence of radiation (Stanley et al., 2015 and references therein).

In this study we acquired apatite (U-Th)/He data for 13 grains and two multigrain aliquots from three different kimberlite pipes of the EDC of southern India. All kimberlites analyzed represent exposed hypabyssal root zones of once larger pipes. Analytical uncertainties for individual grain analyses are based on the propagated error from the U, Th, and He analyses and grain dimensions. As is standard practice, the corrected dates reported in Table 5 were corrected for alpha ejection assuming uniform eU distributions. For samples analysed in this study, apatite eU varies from 2.6 to 30.0 ppm. The low (<45µm) spherical radii of some apatite grains seem to be affecting He ages, i.e. they result in older ages. These older ages can be seen in sample CC-5 and SK-2. Most of the apatites are characterised by a low eU of 2.6-9.5 ppm. The highest eU value was from kimberlite SK-1, which represents an outlier in the measured He ages from the sample. The low eU values of apatite grains are important for their low temperature sensitivity, because apatite is prone to He implantation from neighbouring minerals with high eU content (Stanley et al., 2015). During the radioactive decay, alpha-particles are emitted with high kinetic energy and travel significant distances. This presents a complication for the He dating method, as alpha particles may be ejected out of the crystal being dated or alternatively injected from the surrounding mineral grains, such as perovskite in the case of kimberlite rocks (Lisker et al.,

2009). Effects of U and Th of surrounding minerals to apatite (as opposed to He injection or implantation) leads to overcorrection of He ages (Flowers et al., 2009)

Individual AHe ages range from 121 Ma to 320 Ma. The age scatter (dispersion) could be a result of micro-inclusions, which potentially could not be detected prior to analysis. Alternatively, the age scatter could also be a result of crystal fragmentation, with over- or under correction of the alpha-ejection effect.

Despite the scatter, all measured ages are younger than kimberlite pipe emplacement, signalling a major unroofing event (Stanley et al., 2013). The mean average AHe age for CC-5 is 164.9 ± 21.2 Ma (1S.D; n=5) and for SK-1 & SK- 2 combined is 166.3 ± 25.2 Ma (1S.D; n=5). These ages are indicative of a major unroofing event that affected the EDC during the Mesozoic (Middle Jurassic). Both AHe average dates from the two kimberlite clusters are within close range and they all represent or highlight an event during the Middle Jurassic period.

Our EDC kimberlite AHe ages are plotted against their geographic location in Figure 9a, with Mesoproterozoic kimberlite emplacement ages shown by a light grey band. The SK-2 kimberlite (which we combined with the data for SK-1) occurs ~150 km north of the CC-5 kimberlite on the EDC. There is a positive correlation between AHe dates and eU for sample CC-5 (Fig 8B). Flowers and Kelly (2011) suggest that such correlations are the result of protracted cooling through the apatite helium (HePRZ). However, this can also be explained by the radiation damage effect on apatite He retention. Cherniak et al. (2009), in their study of He and zircon (Zr) diffusion, used the behaviour of helium to explore the behaviour of He ages with depth. They observed that the increase of temperature with depth causes a decrease in He ages and therefore termed this relationship as the 'HePRZ'. At temperatures above 100 ºC , He is lost faster than it is produced therefore the measured He ages would be zero (Cherniak et al., 2009; Flowers et al., 2009).

Table 1. EPMA data for apatite compositions for CC-5 kimberlites (EDC).

	CC-5 4	CC-5 7	CC-5 8	CC-5 9	CC-5 10	CC-5 11	CC-5 15	CC-5 16	CC-5 17	CC-5 18	CC-5 19	CC-5 20	CC-5 21	CC-5 26	CC-5 27	CC-5 28	CC-5 34	CC-5 38	CC-5 41
F	3.13	3.05	3.05	3.02	2.85	2.85	3.07	3.07	3.08	2.97	3.02	2.93	3.09	2.79	2.80	2.77	2.94	2.63	3.09
CaO	0.00	54.24	53.64	53.54	53.27	52.68	54.36	53.19	53.31	54.01	53.52	54.44	53.64	53.62	53.20	54.04	53.60	54.08	54.09
SiO_2	0.43	0.68	0.60	0.59	0.60	0.86	0.49	0.55	0.51	0.51	0.34	0.54	0.51	0.73	0.73	0.63	0.79	0.32	0.33
La_2O_3	0.00	0.16	0.06	0.18	0.00	0.00	0.17	0.08	0.08	0.23	0.09	0.11	0.00	0.00	0.00	0.00	0.19	0.00	0.00
Nd_2O_3	0.02	0.02	0.05	0.00	0.03	0.00	0.12	0.00	0.05	0.00	0.03	0.02	0.06	0.00	0.09	0.00	0.07	0.15	0.00
Cl	0.00	0.02	0.00	0.01	0.00	0.01	0.02	0.02	0.02	0.01	0.01	0.02	0.02	0.03	0.01	0.02	0.01	0.00	0.01
SrO	1.18	1.03	1.21	1.04	1.27	1.33	1.20	1.51	1.39	1.54	1.55	1.26	1.48	1.32	1.68	1.31	1.43	1.15	1.06
P_2O_5	41.61	41.38	41.75	42.02	41.92	41.27	41.58	41.20	41.80	41.59	41.42	41.60	41.88	41.78	40.88	41.52	40.96	42.29	41.89
Ce_2O_3	0.00	0.00	0.02	0.10	0.00	0.00	0.00	0.02	0.00	0.00	0.00	0.00	0.00	0.00	0.08	0.02	0.00	0.00	0.00
Total	100.20	100.58	100.38	100.49	99.94	99.00	101.00	99.64	100.23	100.84	99.98	100.93	100.68	100.26	99.47	100.29	99.99	100.61	100.48
									Normalized to 9 cations										
F	0.786	0.765	0.765	0.756	0.718	0.726	0.768	0.778	0.774	0.745	0.763	0.736	0.774	0.702	0.715	0.698	0.745	0.661	0.775
Ca	4.895	4.916	4.860	4.837	4.829	4.824	4.917	4.871	4.841	4.889	4.887	4.917	4.853	4.849	4.878	4.896	4.894	4.866	4.899
Si	0.037	0.058	0.051	0.050	0.051	0.073	0.041	0.047	0.044	0.043	0.029	0.046	0.043	0.062	0.062	0.053	0.067	0.027	0.028
La	0.000	0.005	0.002	0.006	0.000	0.000	0.005	0.003	0.003	0.007	0.003	0.004	0.000	0.000	0.000	0.000	0.006	0.000	0.000
Nd	0.001	0.001	0.002	0.000	0.001	0.000	0.004	0.000	0.001	0.000	0.001	0.001	0.002	0.000	0.003	0.000	0.002	0.004	0.000
Cl	0.000	0.002	0.000	0.001	0.000	0.002	0.003	0.002	0.002	0.001	0.001	0.002	0.003	0.004	0.002	0.002	0.002	0.000	0.001
Sr	0.058	0.050	0.059	0.051	0.062	0.066	0.059	0.075	0.068	0.075	0.077	0.062	0.072	0.065	0.083	0.064	0.070	0.056	0.052
P	2.990	2.964	2.989	3.000	3.003	2.986	2.972	2.982	2.999	2.976	2.989	2.969	2.994	2.985	2.962	2.973	2.956	3.007	2.998
Ce	0.000	0.000	0.001	0.003	0.000	0.000	0.000	0.001	0.000	0.000	0.000	0.000	0.000	0.000	0.003	0.001	0.000	0.000	0.000
Total	8.77	8.76	8.73	8.70	8.66	8.68	8.77	8.76	8.73	8.74	8.75	8.74	8.74	8.67	8.71	8.69	8.74	8.62	8.75

Table 2. EPMA data for apatite compositions of the CC-5, SK-1, and SK-2 and kimberlites (EDC).

	CC-5 43	CC-5 48	CC-5 51	CC-5 53	CC-5 54	CC-5 64	CC-5 65	CC-5 66	CC-5 71	SK-1 78	SK-1 81	SK-1 84	SK-1 87	SK-1 90	SK-1 91	SK-1 92	SK-2 258	SK-2 268	SK-2 269
F	3.16	2.34	3.27	3.14	3.34	3.45	2.41	3.68	3.51	1.66	2.53	2.66	2.93	1.97	1.75	2.04	1.97	1.98	1.79
CaO	53.88	53.98	53.28	53.08	55.32	53.72	54.68	52.12	53.93	52.42	53.11	51.49	50.63	52.74	49.48	52.58	54.76	55.16	55.17
SiO_2	0.42	0.97	0.64	0.79	0.01	0.43	0.53	0.54	0.41	2.60	0.72	1.25	1.48	0.76	3.21	1.36	1.64	1.49	1.40
La_2O_3	0.00	0.33	0.00	0.00	0.39	0.16	0.10	0.15	0.09	0.18	0.16	0.03	0.03	0.14	0.15	0.00	0.26	0.21	0.00
Nd_2O_3	0.00	0.02	0.00	0.00	0.02	0.00	0.00	0.00	0.03	0.00	0.00	0.16	0.08	0.05	0.22	0.40	0.17	0.00	0.04
Cl	0.01	0.00	0.01	0.00	0.13	0.01	0.02	0.02	0.00	0.01	0.00	0.01	0.04	0.01	0.03	0.02	0.02	0.01	0.02
SrO	0.82	1.52	1.10	1.45	0.52	1.03	1.27	1.10	1.17	0.00	0.00	0.00	0.00	0.00	0.00	0.00	0.23	0.13	0.33
P_2O_5	42.31	41.49	41.78	41.15	40.60	42.07	41.17	42.94	41.23	37.80	36.50	38.58	37.55	40.25	36.42	39.16	39.84	41.70	41.67
Ce_2O_3	0.00	0.00	0.00	0.00	0.00	0.01	0.06	0.01	0.00	0.00	0.00	0.00	0.00	0.00	0.00	0.00	0.00	0.00	0.07
Total	100.60	100.66	100.08	99.61	100.31	100.87	100.24	100.55	100.37	94.68	93.03	94.20	92.72	95.91	91.27	95.55	98.89	100.68	100.48
Normalized to 9 cations																			
F	0.787	0.592	0.820	0.794	0.842	0.857	0.614	0.907	0.880	0.447	0.697	0.711	0.792	0.521	0.486	0.542	0.509	0.498	0.453
Ca	4.856	4.863	4.840	4.856	5.083	4.856	4.962	4.700	4.927	4.963	5.242	4.946	4.959	4.929	4.847	4.954	5.001	4.907	4.914
Si	0.035	0.082	0.054	0.067	0.001	0.036	0.045	0.045	0.035	0.229	0.066	0.112	0.135	0.066	0.294	0.119	0.140	0.124	0.116
La	0.000	0.010	0.000	0.000	0.012	0.005	0.003	0.005	0.003	0.006	0.005	0.001	0.001	0.004	0.005	0.000	0.008	0.007	0.000
Nd	0.000	0.001	0.000	0.000	0.001	0.000	0.000	0.000	0.001	0.000	0.000	0.005	0.003	0.002	0.007	0.013	0.005	0.000	0.001
Cl	0.001	0.000	0.001	0.000	0.017	0.001	0.002	0.003	0.000	0.002	0.001	0.002	0.005	0.001	0.005	0.003	0.003	0.002	0.003
Sr	0.040	0.074	0.054	0.072	0.026	0.051	0.062	0.054	0.058	0.000	0.000	0.000	0.000	0.000	0.000	0.000	0.012	0.006	0.016
P	3.013	2.954	2.999	2.975	2.948	3.005	2.952	3.060	2.976	2.828	2.847	2.928	2.906	2.972	2.819	2.915	2.875	2.932	2.933
Ce	0.000	0.000	0.000	0.000	0.000	0.000	0.002	0.000	0.000	0.000	0.000	0.000	0.000	0.000	0.000	0.000	0.000	0.000	0.002
Total	8.73	8.57	8.77	8.76	8.93	8.81	8.64	8.77	8.88	8.47	8.86	8.70	8.80	8.49	8.46	8.55	8.55	8.47	8.44

Table 3. EPMA data for apatite compositions for the SK-2 kimberlites (EDC).

	SK-2 270	SK-2 261	SK-2 262	SK-2 263	SK-2 264	SK-2 265	SK-2 266	SK-2 271	SK-2 274	SK-2 276	SK-2 279	SK-2 285	SK-2 286	SK-2 288	SK-2 289	SK-2 290	SK-2 292	SK-2 294	SK-2 295
F	2.09	2.06	1.48	1.62	1.49	1.64	1.74	2.22	1.92	2.22	1.94	1.82	1.76	1.87	1.89	1.69	2.11	2.05	2.05
CaO	54.57	54.22	55.44	54.08	54.14	53.99	54.16	54.36	53.90	53.59	53.48	53.83	53.63	54.32	54.50	54.88	54.79	54.25	54.69
SiO_2	1.32	1.40	1.54	1.47	1.65	1.65	1.64	1.41	1.42	1.56	1.48	1.48	1.45	1.53	1.67	1.67	1.48	1.60	1.50
La_2O_3	0.00	0.05	0.28	0.00	0.16	0.10	0.00	0.12	0.35	0.15	0.29	0.12	0.18	0.37	0.17	0.00	0.19	0.00	0.00
Nd_2O_3	0.12	0.00	0.05	0.10	0.09	0.08	0.00	0.23	0.05	0.29	0.00	0.03	0.00	0.00	0.00	0.00	0.00	0.03	0.11
Cl	0.02	0.03	0.02	0.02	0.02	0.02	0.02	0.02	0.02	0.03	0.02	0.04	0.04	0.02	0.02	0.01	0.02	0.02	0.01
SrO	0.40	0.29	0.11	0.28	0.19	0.17	0.16	0.25	0.00	0.52	0.40	0.00	0.27	0.10	0.12	0.40	0.28	0.00	0.23
P_2O_5	42.41	40.72	40.92	40.48	40.42	40.13	40.02	39.79	41.03	39.84	41.29	40.20	40.43	40.43	39.82	40.66	41.01	41.76	42.01
Ce_2O_3	0.04	0.00	0.00	0.07	0.00	0.01	0.00	0.00	0.00	0.00	0.00	0.00	0.00	0.00	0.08	0.00	0.06	0.00	0.05
Total	100.97	98.76	99.85	98.12	98.16	97.78	97.74	98.39	98.68	98.21	98.88	97.53	97.75	98.64	98.26	99.30	99.92	99.71	100.64
F	0.523	0.529	0.380	0.422	0.388	0.428	0.453	0.575	0.494	0.576	0.497	0.475	0.457	0.483	0.491	0.433	0.536	0.519	0.516
Ca	4.833	4.931	4.972	4.933	4.929	4.943	4.964	5.000	4.890	4.936	4.838	4.944	4.913	4.945	4.993	4.952	4.933	4.853	4.860
Si	0.109	0.119	0.129	0.125	0.140	0.141	0.140	0.121	0.120	0.134	0.125	0.127	0.124	0.130	0.142	0.140	0.125	0.134	0.124
La	0.000	0.001	0.009	0.000	0.005	0.003	0.000	0.004	0.011	0.005	0.009	0.004	0.006	0.012	0.005	0.000	0.006	0.000	0.000
Nd	0.004	0.000	0.002	0.003	0.003	0.002	0.000	0.007	0.001	0.009	0.000	0.001	0.000	0.000	0.000	0.000	0.000	0.001	0.003
Cl	0.003	0.004	0.003	0.003	0.003	0.002	0.003	0.003	0.003	0.004	0.003	0.006	0.005	0.003	0.003	0.001	0.002	0.003	0.002
Sr	0.019	0.014	0.006	0.014	0.009	0.008	0.008	0.012	0.000	0.026	0.019	0.000	0.014	0.005	0.006	0.019	0.014	0.000	0.011
P	2.969	2.926	2.900	2.918	2.908	2.903	2.899	2.892	2.941	2.900	2.952	2.918	2.927	2.909	2.882	2.899	2.917	2.951	2.950
Ce	0.001	0.000	0.000	0.002	0.000	0.000	0.000	0.000	0.000	0.000	0.000	0.000	0.000	0.000	0.003	0.000	0.002	0.000	0.001
Total	8.46	8.52	8.40	8.42	8.39	8.43	8.47	8.61	8.46	8.59	8.44	8.47	8.45	8.49	8.52	8.45	8.53	8.46	8.47

Table 4. EPMA data for apatite compositions for the SK-2 kimberlites (EDC) continued.

	SK-2 296	SK-2 297	SK-2 298	SK-2 301	SK-2 302	SK-2 303	SK2 304	SK-2 305	SK-2 306	SK-2 309	SK-2 311	SK-2 315	SK-2 317
F	1.39	1.77	1.23	1.84	1.54	1.87	1.68	1.63	1.42	1.97	1.86	1.64	1.81
CaO	56.27	56.31	56.28	54.74	53.16	54.71	53.48	54.33	53.93	54.53	54.71	53.82	54.37
SiO_2	1.35	1.53	1.53	1.52	1.33	1.42	1.73	1.68	1.54	1.61	1.56	1.57	1.15
La_2O_3	0.00	0.19	0.23	0.00	0.06	0.00	0.00	0.08	0.00	0.00	0.17	0.00	0.23
Nd_2O_3	0.10	0.00	0.00	0.00	0.06	0.08	0.18	0.01	0.00	0.10	0.00	0.07	0.11
Cl	0.01	0.03	0.01	0.02	0.02	0.02	0.02	0.02	0.02	0.02	0.01	0.03	0.01
SrO	0.21	0.33	0.12	0.35	0.11	0.14	0.17	0.16	0.05	0.24	0.02	0.13	0.00
P_2O_5	41.55	41.01	41.36	41.20	41.40	41.00	40.83	40.44	40.89	40.96	40.99	40.19	40.08
Ce_2O_3	0.03	0.05	0.00	0.00	0.08	0.03	0.00	0.00	0.04	0.00	0.00	0.05	0.00
Total	100.91	101.22	100.76	99.67	97.75	99.26	98.09	98.33	97.89	99.42	99.31	97.51	97.75
						Normalized to 9 cations							
F	0.353	0.449	0.313	0.469	0.399	0.478	0.435	0.423	0.370	0.502	0.475	0.429	0.472
Ca	4.987	5.010	4.988	4.918	4.830	4.939	4.860	4.939	4.899	4.917	4.931	4.937	5.002
Si	0.111	0.127	0.127	0.127	0.113	0.119	0.147	0.143	0.130	0.136	0.131	0.134	0.098
La	0.000	0.006	0.007	0.000	0.002	0.000	0.000	0.002	0.000	0.000	0.005	0.000	0.007
Nd	0.003	0.000	0.000	0.000	0.002	0.003	0.005	0.000	0.000	0.003	0.000	0.002	0.003
Cl	0.001	0.004	0.002	0.002	0.003	0.003	0.002	0.002	0.003	0.002	0.001	0.005	0.002
Sr	0.010	0.016	0.006	0.017	0.006	0.007	0.009	0.008	0.002	0.012	0.001	0.006	0.000
P	2.910	2.883	2.897	2.924	2.972	2.924	2.932	2.905	2.935	2.918	2.919	2.913	2.914
Ce	0.001	0.002	0.000	0.000	0.002	0.001	0.000	0.000	0.001	0.000	0.000	0.002	0.000
Total	8.38	8.50	8.34	8.46	8.33	8.47	8.39	8.42	8.34	8.49	8.46	8.43	8.50

Table 5. (U-Th)/He thermochronology data for the EDC kimberlites.

Sample	Grains	Mass (µg)	Grain Length	Radius (µm)	Ft	U (ppm)	Th (ppm)	Sm (ppm)	eU (ppm)	4He (nmol/g)	Raw date (Ma)	1 STD	Corr Date (Ma)	Analytical error (Ma)
CC-5 (77.6361 E, 14.5188 N)														
Ap 1	1	2.1	134	50	0.69	2.0	4.1	2.5	2.9	1.5	95.4	11.4	137.9	19.6
Ap 2	1	1.7	110	47	0.66	5.8	6.4	1.3	7.3	6.2	154.8	10.1	235.4	23.6
Ap 3	2	0.8	117	45	0.64	5.5	17.0	3.1	9.5	5.1	98.1	9.5	154.4	25.2
Ap 4	1	12.5	235	78	0.81	3.1	8.8	1.5	5.1	1.1	136.3	3.6	168.0	12.8
Ap 5	1	1.9	136	45	0.68	3.0	6.4	1.6	4.5	0.1	88.2	15.5	128.7	24.8
Ap 6	1	1.5	155	40	0.64	1.9	3.1	0.7	2.6	0.1	148.1	55.8	229.5	92.0
Ap 7	3	-	-	1.53	0.70	19.4	45.2	10.1	30.0	36.4	220.0	8.0	316.9	25.0
SK-2 (77.5543 E, 16.1909 N)														
Ap 1	1	1.8	149	46	0.65	2.0	11.8	1.7	4.8	2.5	97.4	7.7	149.2	19.7
Ap 2	1	1.7	136	45	0.66	4.4	18.9	4.5	8.9	4.0	82.2	3.6	125.3	13.7
Ap 3	1	1.8	180	44	0.62	0.9	7.1	1.9	2.6	2.5	174.4	60.6	283.7	105.7
Ap 4	1	2.4	181	49	0.68	3.0	7.2	2.3	4.7	2.1	82.2	13.1	121.1	22.3
Ap 5	1	4.8	239	62	0.74	0.8	15.9	3.8	4.5	4.8	192.8	13.4	258.4	13.4
SK-1 (77.5543 E, 16.1909 N)														
Ap 1	1	2.8	127	53.9	0.71	1.1	7.8	3.4	3.0	2.0	121.4	20.0	170.7	30.6
Ap 2	1	4.0	216	59.1	0.70	0.7	13.1	1.8	3.8	2.5	119.0	11.7	161.8	19.9
Ap 3	1	9.5	210	78.1	0.80	28.0	4.8	23.4	29.2	52.2	320.3	3.3	320.3	27.3

Analytical error- uncertainty including estimates for the uncertainty in the alpha ejection correction.

eU- effective uranium concentration, weights U and Th for their alpha productivity, computed as [U] + 0.235 * [Th]

Ft- is alpha-ejection correction of Farley et al (2002).

Uncertainty is based on the raw U, Th, He, and grain length measurements. Date corrected using F_{TH} correction

Data for shaded rows are not included in HeFTy modelling.

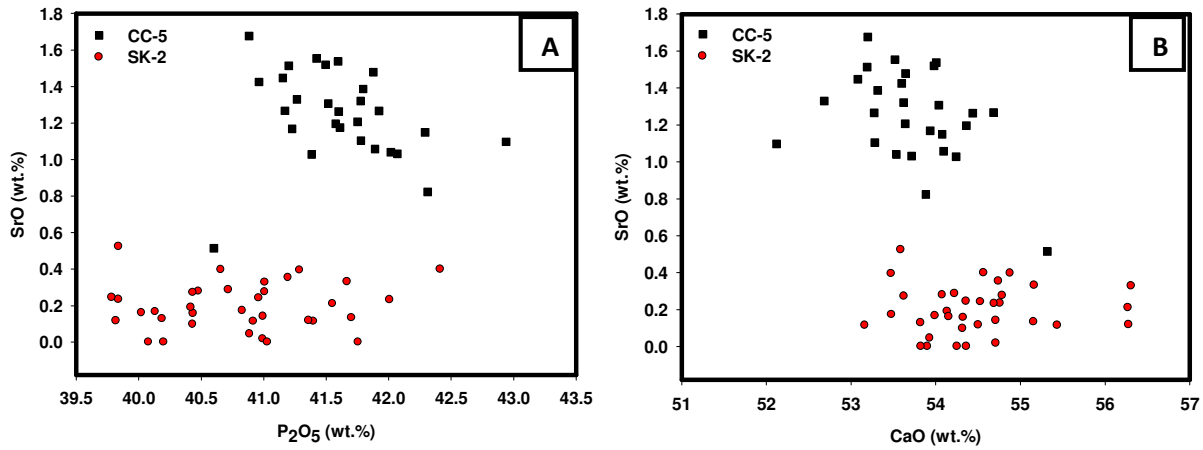

Figure 8. Chemical composition of apatites from the EDC Kimberlites. (a) A plot of SrO versus P_2O_5. (b) SrO versus CaO.

3.4 *(U-Th)/He apatite systematics*

Samples in this study occur in close proximity to each other. Figure 9a shows sample latitude in degrees with the north and south directions depicted on the plot. The SK-1 and SK-2 samples both plot in the north, whereas sample CC-5 plots in the south. As mentioned above, the Siddanpalle kimberlites from the Raichur kimberlite field are situated about 100 km north of the Wajrakarur Kimberlite Field (Chigicherla cluster). Uranium content ranges from 1.9-19.4 ppm, for kimberlite CC-5 with the majority of the grains below 6 ppm. Thorium concentration is variable from 3.1–45.2 ppm. Grain analyses with high eU (20 ppm upwards) and low rs are referred to as outliers. The U and Th concentrations for kimberlite SK-1 and SK-2 seem to vary from grain to grain, whereas eU seems to be restricted to values between 3.0 – 8.9 ppm with an outlier at 29.2 ppm.

Figure 9b shows the correlation between apatite He date and eU. The U and Th contents are generally low throughout the samples. Sample SK-1 and SK-2 have lower U and Th contents (0.7-2.0 ppm U, 4.8-11 ppm Th) than for sample CC-5 (Table1). There is no clear indication/restriction of eU with age scatter, there are grain analyses with low (<6 ppm) eU yielding older ages and there are also grains with high eU (>6 ppm) yielding older ages. The presence of micro-inclusions or helium implantation from surrounding minerals could have resulted in data dispersion. The positive correlation between date and eU (Figure 9b) in both samples suggest slow cooling in the apatite He PRZ (Flowers et al., 2009).

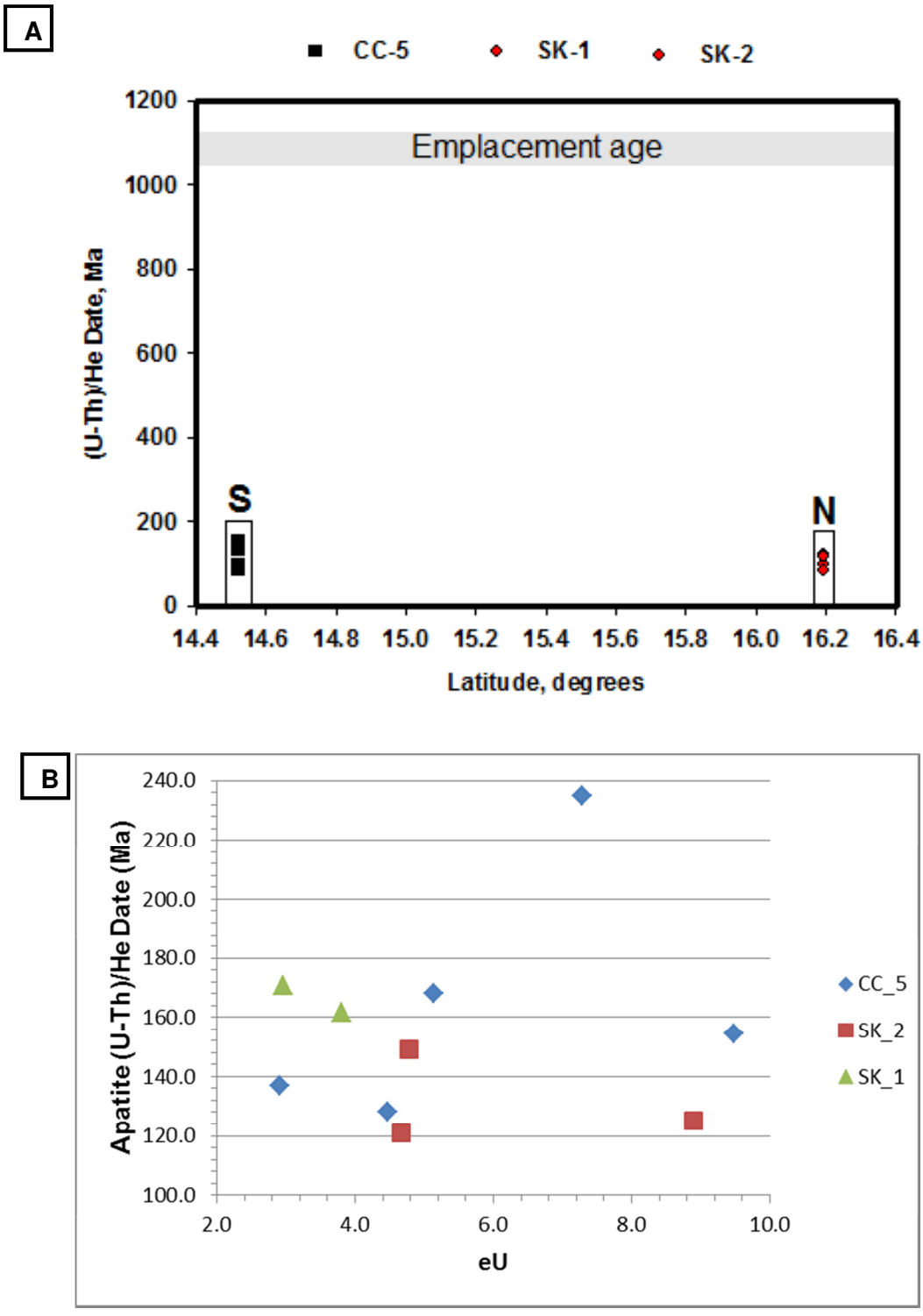

Figure 9: Apatite (U-Th)/He data. (a) Individual grain AHe date or age plotted against sample latitude. (b) Date (Ma) plotted against eU (ppm).

4 Discussion

4.1 *Constraints on the mechanism for uplift and erosion of Peninsular India*

Although we do not know the complete history as to when and how kimberlites were eroded on the EDC, the known kimberlite pipe architectures and t-T modelling using the obtained AHe ages provide new insights. Most kimberlites in the EDC are exposed root zones, but there is some rare record of preserved crater facies kimberlite in the RKF of southern India (Ravi and Satyanarayana, 2007) and in the Tokapal Kimberlite Field of central India (Mainkar et al., 2004). Lorenz & Kurszlaukis (2007) defined a maar-diatreme volcano as connection from bottom of the root zone upwards, including the diatreme and tephra rings. Importantly, subvolcanic root zones of maar-diatreme volcanoes can only develop if the magmatic system breached Earth's surface and eruption of pyroclastic material occurred (i.e. a crater had developed). Maar-diatreme root zones typically form 1.5 to 3 km below the pre-eruptive land surface.

In this section we discuss a model for the erosion of the 1.1 Ga southern Indian kimberlites. The model is constructed using t-T plots from HeFTy software, calculating cooling and denudation rates since time of emplacement. Based on HeFTy modelling results (Model C; Figure 13e, f), we suggest that immediately after emplacement of the kimberlite magmas at ca. 1.1 Ga, with development of complete maar-diatreme volcanic systems, burial occurred and persisted for a period of 500 million years before any significant uplift occurred. This assumption is based on the fact that the punctuated Purana Basin development occurred between ca. 1.6 and 0.7 Ga with predominantly marine sedimentation (Joy et al., 2015; and references therein). A similar, more modern scenario is provided by the Late Cretaceous Fort a la Corne kimberlites in western Canada, which emplaced into marine sediments along the shorelines of the Western Interior Seaway of cratonic North America (Pittari et al., 2008). Importantly, craters and even extra-crater kimberlitic tuffs are still preserved due to continued marine sedimentation during the Late Cretaceous and Early Cenozoic (Zonneveld et al., 2004).

We present cartoons for how the 1.1 Ga EDC kimberlites were eroded down to root zone level (Figure 10). Three cartoons are shown: 1) A complete and fully developed kimberlite pipe at emplacement, 2) Continued deposition of Purana sediments until 800-600 Ma, and 3) The present day exposure of the pipe (this study).

Figure 10A shows a kimberlite pipe from the root zone to the crater; in our estimates we used a vertical pipe dimension of 3 km (Hawthorne, 1975). For CC-5 kimberlite, following pipe emplacement ~ 2.5 km (Figure 10B) of mainly marine sediments were deposited over the kimberlite body for a period of 500 Myr reaching temperatures > 175 °C. This t-T development is independently constrained by 1.1 Ga old kimberlitic zircons (U/Pb age) from the WKF that yielded (U-Th)/He ages of ca. 700 ± 50 Ma (C. Kirkland, pers. comm, 2015), suggesting that cooling to below 200°C occurred only after 800-600 Ma. Following these periods of Purana sedimentation, the EDC crust encasing the 1.1 Ga kimberlite body is brought up slowly near to sea level by 360 Ma. The kimberlite pipe continues to be uplifted and slowly eroded, and by 175 Ma (Figure 12C), ~ 4 km of EDC crust (sediments plus some basement) were removed exposing the root zone of the 1.1 Ga kimberlite pipe. After 175 Ma the pipe contimues to be slowly eroded until exposed currently as the surface area.

For the Siddanpalle kimberlites (SK-1/2), we have the same scenario of erosion history (refer to Figure 10). We have the kimberlite pipe emplaced at 1.1 Ga and buried for a period of 450 Myr until 655 Ma and thereafter followed by a fast period of uplift and erosion between 655 Ma and 500 Ma for a period of 155 Myrs. A period of slow cooling occurred from 500 Ma to 200 Ma (for a period of 300 myrs) until 175 Ma when there is constant period of fast erosion. The SK-1 and SK-2 kimberlite pipes are currently eroded to ~1 km depth (these kimberlites require an initial kimberlite pipe of 6 km as opposed to 3 km pipe required for the CC-5 erosion estimate). The CC-5 kimberlite pipe is eroded to a depth of 1.5 km (see Figure 11).

Denudation rates for the two kimberlite occurences were estimated using the cooling signals or segments from t-T plots; and the geothermal gradient of 20 ºC/km and the following formulas were used from Wu et al. (2014):

$$Cooling\ rate\ (°C/Ma) = \frac{Temperature\ (°C)}{Time\ (Ma)}$$

$$Denudation\ (km/Ma)\ = \frac{Cooling\ rate\ (°C/Ma)}{Geothermal\ Gradient\ (°C/km)}$$

From the estimations, the (SK-1/2) kimberlite pipe underwent a denudation of 2.2 km since the Neoproterozoic while the CC-5 kimberlite underwent 2.6 km of denudation in the same period until present age. These observations from the denudation calculations are significant, these kimberlites are from the same craton, therefore they experiences similar denudation rates with a difference of 0.4 km. The Siddanpalle kimberlitesa are eroded fast to a depth of 1 km whereas the Chigicherla kimberlite pipe eroded to a depth of 1.5 km, which is in agreement with the

current position (elevations) of these areas. The Siddanpalle kimberlite pipes (SK-1/2), sit at a much lower elevation (298 m) than the Chigicherla kimberlite pipe CC-5 (398 m). It is reasonable for the SK-1/2 pipe to be eroded much quicker than the CC-5 pipes which were probably proximal to the depocentre since the inversion of Purana basins. Therefore the SK-1/2 pipe got eroded much quicker as Gondwana began to separate. The use of HeFTy in producing t-T plots have aided in calculating erosion estimates and also the reconstruction of the original ideal pipe for pipe CC-5. Figure 11 shows the reconstructed ideal CC-5 kimberite pipe, and also the current erosion level at 1.5 km depth.

Table 6 shows erosion estimates of some kimberlites from worldwide occurrences, which are grouped based on the magnitude of erosion as shallow, moderate and deeply eroded. Both the SK-1/2 and CC-5 kimberlite pipes fall under the deeply eroded category. The Premier kimberlite (1150 Ma) originally discovered by Wager (1914), being the largest pipe in South Africa originally measured 32 hectares and is comprised of diatreme facies to a depth of 550 m below which it grades into the root zone. According to Bartlett (1998), 300 m of kimberlite have been removed from the top of the Premier pipe (Tukker et al., 2016); this kimberlite would fall under moderately eroded kimberlites.

Table 6. Estimated erosion levels of some kimberlites in the world, from (Brown & Valentine, 2013)

Kimberlite field	Age (Ma)	Erosion estimates (m)
Shallow eroded Kimberlite fields		
Orapa (Botswana)	90	<200 m since emplacement
Northern Lesotho kimberlites	Cretaceous	< 300 m of erosion
Moderately eroded Kimberlites		
Ekati-Lac de Gras, Canada	74-73	<<500
Venetia Kimberlite Field (SA)	520	~500 m
Premier kimberlite	1150	300 m
Deeply eroded		
Kimberley younger group (Group 1)	111-97	~850 m of erosion
The older Kimberley group (Group 2)	119-114	~1250 m of erosion

The emplacement of Indian kimberlites into active Purana basin, the subsequent burial and later unroofing has implications for the source of alluvial diamonds in India. Tension in the basin caused crustal thinning which caused the rocks to crack easily and allowed the pipes to form.

During extension of the basins sediments are being deposited over time, minimal erosion may have occurred before the burial of the kimberlite pipes. Burial of the pipes acted as an insulation (slower cooling) mechanism, which preserved the pipes. Unroofing will speed up cooling and exposed the pipes to erosion. Consequently, the diamonds would move downhill and redistribute in the local and regional drainage systems.

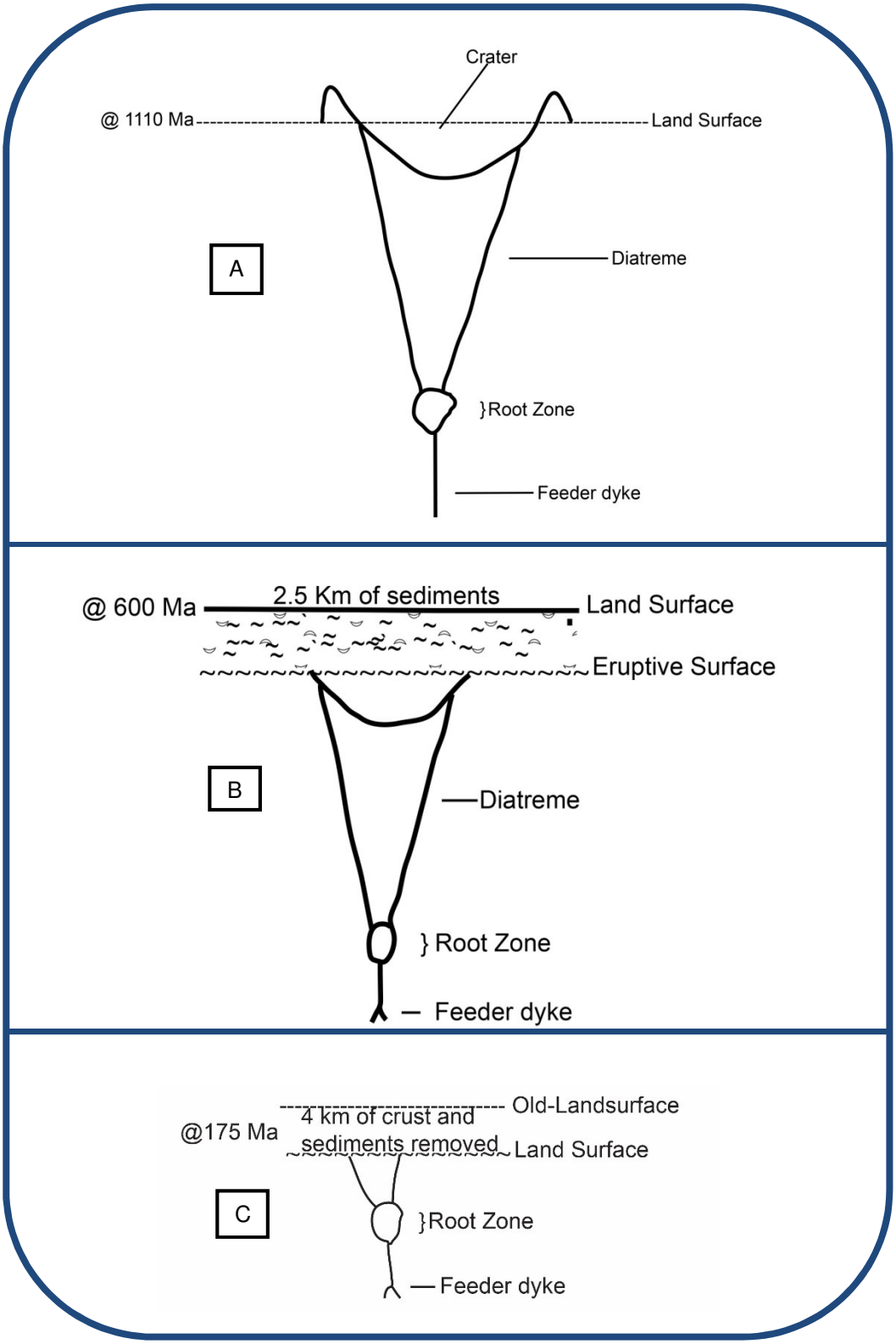

Figure 10: Chigicherla (CC-5) erosion model. (a) Ideal kimberlite pipe at emplacement. (b) Period of Purana sedimentation until ca. 600 Ma. (c) Shows erosion estimate from 175 Ma to present. The current pipe exposure is at root zone. The Chigicherla kimberlite experienced a 4 km erosion of crust including 2.5 km of sediments and 1.5 km of granitic basement.

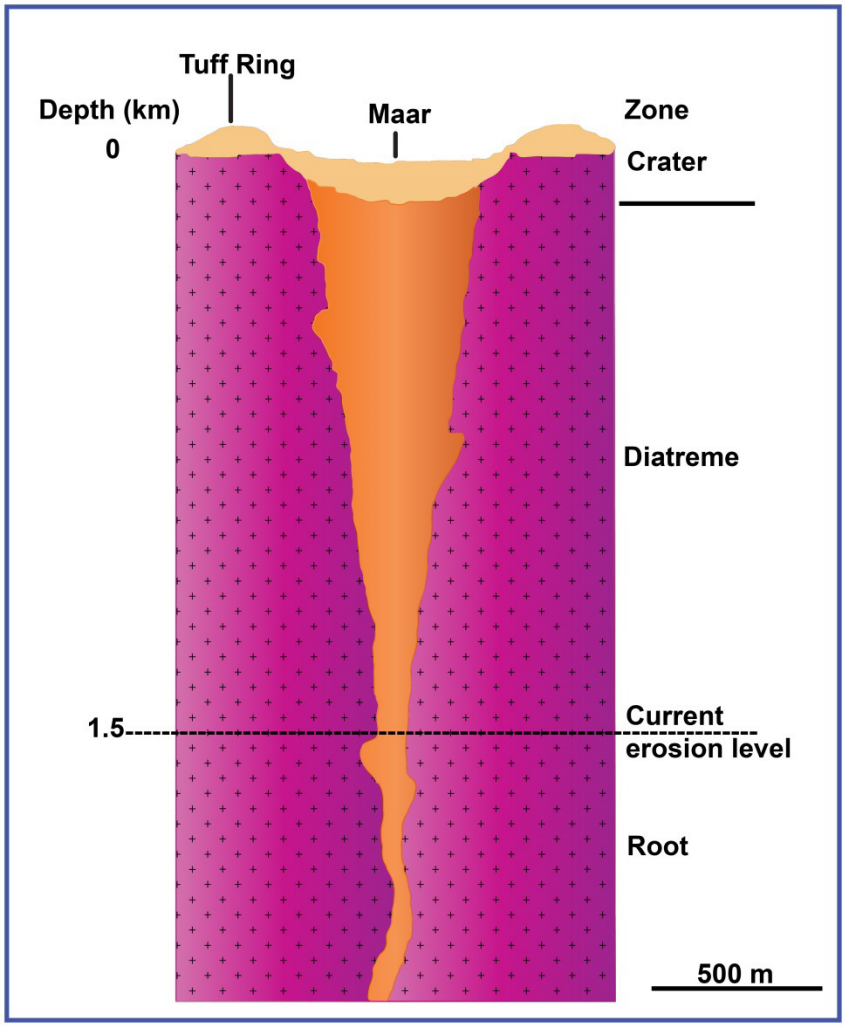

Figure 11: Schematic pipe model for the Chigicherla kimberlite (CC-5), showing the different zones in the pipe and the current erosion surface after Kirkley et al. (1991) and the estimated current erosion surface for the Chigicherla pipe (this study).

4.2 *Time-Temperature Modelling*

4.2.1 Model constraints and assumptions

HeFTy allows use of assumptions where the geologic history of the area is only poorly known. The kimberlite emplacement age serves as one of the important constraints in this study. Figure 12 shows emplacement ages of the kimberlites of the WKF. Kimberlite magmatism in the DC took place essentially in the Mesoproterozoic (~1100 Ma). Although, various dating techniques were employed, there is a strong correlation of ages determined by U-Pb perovskite and K-Ar phlogopite and whole-rock methods. This study used 1100 Ma as the eruption age for the DC kimberlites (Chalapathi Rao et al., 2013; Kumar et al., 2007a). For each t-T plot, the paths were assumed to be monotonic (heating/cooling only) and simulated at 10 000 random Monte Carlo

paths in order to cover a range of possible paths. The U, Th, and Sm concentrations, rs values, and the uncorrected He ages (Table 5), were used for all samples as inputs in the HeFTy software.

The software then incorporates alpha-ejection correction methods after Farley & Stockli (2002) and generates the t-T plots with good fits, acceptable or possible paths (Ketcham, 2005). We present here three models that were tested to constrain the cooling history of the EDC in southern India The first two models are based on assumptions, i.e. Model A and Model B, whereas Model C is based on known geologic processes that occurred on the EDC. The first constraint is always the eruption age of the kimberlite (1110 Ma), at temperatures greater than 120 ˚C.

- In Model A (Figure 13A,B),: we use only the emplacement age at ca. 1100 Ma as the constraint 1 (at temperatures between120-140 °C) with no further constraints other than 20°C present-day surface temperature (annual average for southern India). We do not influence the thermal history of our samples between kimberlite emplacement at depth and present-day exposure at surface, which allows HeFTy to generate random paths to produce t-T plots that will best suit the data.
- We have in Model B (Figure 13C, D), three constraints**:** Constraint 1 is similar to Model A. We further impose that there is no subsequent burial or uplift until 800-500 Ma (Constraint 2), the kimberlite was emplaced in an active basin and subsequently buried. Constraint 2 (at temperatures of 120-140 °C) is based on the known occurrences of sedimentary Purana basins and the fact that kimberlites of the EDC intruded into these long-lived Proterozoic basins (Collins et al., 2014). As a third constraint, we use the AFT data (interior transect with ages between 100 and 200 Ma with AFT temperature sensitivity of ~ 60-120˚C) from Sahu et al. (2013). These authors used basement granite samples from the EDC and suggested accelerated cooling in the Late Cretaceous. The three constraints force paths to pass through the suggested t-T history (Figure 13).

Table 7. Emplacement ages for the kimberlites of the WKF, determined using different dating techniques. All ages are Mesoproterozoic with the exception of Pipe 3.

Sample ID	Occurrence	Emplacement age (Ma)	Age Method	Reference (s)
CC-4	Gollapalle	1117±14	U-Pb (prv)	Rao et al. (2013)
CC-5	Gollapalle	1110±18	U-Pb (prv)	Rao et al. (2013)
CC-5	Gollapalle	1058±8	U-Pb (prv)	This study
P-2	Wajrakarur	1124±5	U-Pb (prv)	Rao et al. (2013)
P-1	Wajrakarur	1091±20	Rb-Sr (phl)	Kumar et al. (1993)
P-2	Wajrakarur	1092±15	Rb-Sr (phl)	Kumar et al. (1993)
P-5	Muligiripalle	1093±20	Rb-Sr (phl)	Chalapathi Rao et al. (1996)
SK-1	Siddanpalle	1093±4	Rb-Sr (phl)	Kumar et al. (2007)
P-3	Lattavaram	933-698	K-Ar (phl)	Basu and Tatsumoto (1979)
P-3	Lattavaram	966±38	K-Ar (W.R)	Paul et al. (1975)
P-4	Lattavaram	1023±40	K-Ar (W.R)	Paul et al. (1975)
P-5	Muligiripalle	1153±17	K-Ar (phl)	Kumar et al. (1993)
P-5	Muligiripalle	1113±3	Ar-Ar (phl, fusion)	Osborne et al. (2011)
P-7	Muligiripalle	1091±10	Rb-Sr (phl)	Kumar et al. (1993)

Phl- Phlogopite, Prv- Perovskite, W.R.- Wall Rock

- In Model C (Figure 13E, F), we also use three constraints: emplacement age at ca. 1100 Ma (Constraint 1) between 120-140 °C with subsequent burial until 800-600 Ma (Constraint 2) at temperatures between 160-180°C. A period of marine, deltaic and fluvial sedimentary sequences known as Purana (Chaudhuri et al., 2001) is thought to have occurred during the Proterozoic from ~1600 Ma until the latest basin inversion reported to have occurred by 520 Ma (Basu & Bickford, 2015). The third constraint is similar to the above, i.e. AFT ages for basement granitoids taken from Sahu et al. (2013).
- It is important to note again that kimberlite pipes SK-1 and SK-2 were modelled together in HeFTy as a single occurrence, because they are from the same kimberlite cluster (Siddanpalle cluster of the Raichur Kimberlite Field) only 2 km apart (Fareeduddin & Mitchell, 2012). They are now referred to as SK-1/2 for the section of thermal history simulations and intepretations.

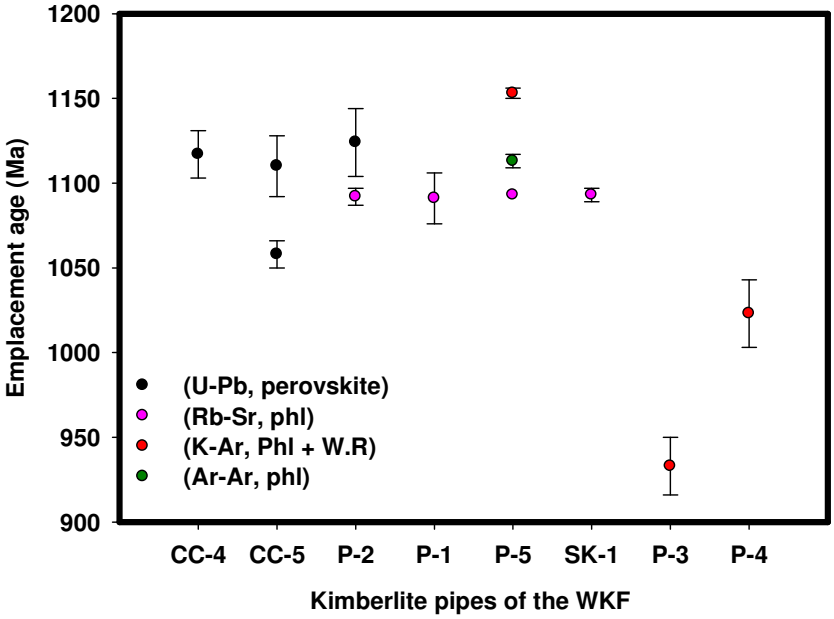

Figure 12: Emplacement ages for the kimberlites of the EDC Dated with different techniques, most of the dates fall within the Mesoproterozoic era (Paul et al., 1975; Basu & Tatsumoto, 1979; Kumar, et al., 1993; Osborne et al., 2011; Chalapathi Rao et al., 2013).

4.2.2 Possible thermal histories recorded by Dharwar Craton kimberlites

All data in Table 5, except for the data highlighted in light grey, are included in the HeFTy modelling. The excluded data have either anomalous eU contents or radius measurements and typically yield unreasonably old AHe dates. Figure 13 shows thermal history simulation results for the kimberlites of the EDC. For each panel or diagram black boxes represent imposed constraints, grey lines represent acceptable paths and black lines represent paths of good fit. The black solid line is a goodness of fit line.

In Model A (Figure 13A,B), for both sample CC-5 and SK-1/2 the paths show slow cooling followed by rapid cooling during the Late Neoproterozoic. Sample CC-5 requires the fast cooling to commence at 550 Ma at a temperature of 95°C, whereas SK-1/2 requires the fast cooling to commence at 450 Ma at temperatures close to 100 °C. The fast cooling recorded at 450-550 Ma can be related to significant uplift and erosion during the final stages of Gondwana amalgamation.

For Model B (Figure 13C, D), the paths allow for burial immediately after kimberlite eruption (~1110 Ma) over a period of marine sedimentation up to until 800-600 Ma, i.e. continued Purana

Basin deposition (Joy et al., 2015; Bickford and Basu, 2015). Paths for CC-5 require intense heating after kimberlite eruption until about 600 Ma followed by very fast cooling between 600 Ma and 175 Ma. During the latter time interval, the sample CC-5 cooled at a constant rate (within the apatite helium PRZ between ~70-30°C) until reaching Earth's surface. Major uplift and cooling takes place at 175 Ma. Paths in SK-1/2 allow for burial from T= 120°C to 135 °C after which the sample slowly cools until 400 Ma. The major cooling signals are observed between 400 Ma and 175 Ma for a period of ca. 200 Myr. The cooling signal until 400 Ma may be linked to Gondwana formation while the cooling signal at 175 Ma can be linked to Gondwana break-up. At 175 Ma the sample cooled extremely fast from T=75-40 °C. In both samples a major cooling signal is recorded at 175 Ma.

In Model C (Figure 13E, F), paths for sample CC-5 allow for burial/heating at 1100 Ma from 130°C to at least 175°C, until 600 Ma (Purana deposition), and then slow uplift/cooling for a period of 200 Myr. Fast cooling commences at 400 Ma until 175 Ma, followed by extremely fast cooling at around 175 Ma. For kimberlite SK-1/2, paths allow for burial/heating at 1110 Ma from 125°C to175°C, until 655 Ma (Purana sedimentation) and fast cooling takes place for a period of 155 Myr (from 655 Ma-500 Ma) at the peak of 500 Ma during Gondwana formation. From 500 Ma cooling continues until 175 Ma, where the sample starts to cool extremely fast. The peak at 150 Ma signals a time when India was moving southward prior the northward movement towards its current position in the Northern Hemisphere.

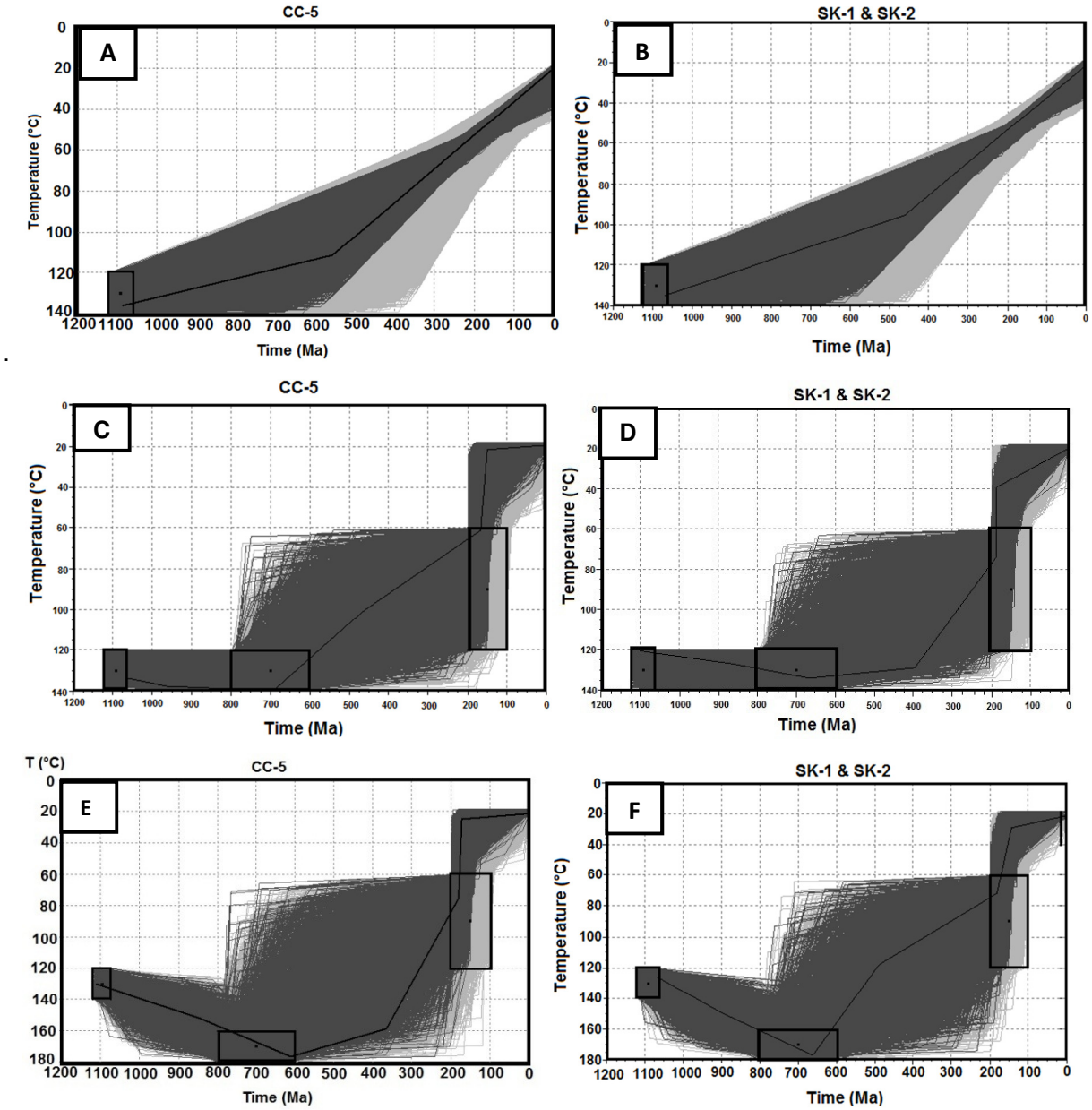

Figure 13: Time-temperature plots depicting the cooling history of southern India (EDC). Black boxes represent imposed constraints. Light grey and dark grey lines represent acceptable and good fits, respectively. The solid line is the goodness of fit line. A-B shows the simple model A for sample CC-5 (a), and SK-1 & SK-2 (b), model A has kimberlite emplacement as the only constraint. (C-D) shows model B for both sample CC-5 (c) and SK-1 & SK-2 (d), model B has three constraints, Constraint 1 is the kimberlite emplacement age at 1100 Ma, Constrain 2 represents known continued Purana sedimentation between 800 and 600 Ma, Constraint 3 is the AFT data from granitic basement rocks (Sahu et al., 2013). (E-F) show model C, constraint 1 starts at 120-140 °C to allow for burial, Constraint 2 and 3 are similar to those of model B.

4.2.3 Preferred Time-Temperature Model

Of importance to note is the Mesozoic cooling signal in all models, despite the different imposed constraints for the samples in the different models. The cooling/uplift during the Middle Jurassic

is a major signal that will aid in explaining the erosion history of the EDC. The cooling signals also record some of the global tectonic activities, which help to understanding the position of India during those times. The cooling signal observed from 175 Ma-100 Ma from the t-T plots in all the three models; is indicative of apatite crystals cooling quickly through the PRZ. This is occurring at temperatures between 75-20 ºC, which is the temperature at which He can be retained, He is only retained below temperatures of 75ºC (Zeitler et al., 1987; Flowers et al., 2009).

Model A, which is the 'erosion-only' model, allows for kimberlite magma emplacement and ignores all other known geological activities. This model shows a signal around 600 Ma, which can be related to Gondwana formation. The model does not necessarily produce paths that relate to the geology of southern India. Model B, which allows for eruption and subsequent kimberlite pipe burial (heating), followed by an unroofing event is also not consistent with the known history of the EDC. This however can be interpreted as a plausible sequence of events based on limited knowledge of parameters and geologic inputs for this region.

Model B shows similarities with Model C, in that at 200 Ma the abrupt cooling signal is prominent in both samples. The SK-1/2 Model B cools slowly within the apatite helium partial retention zone (~75-40 °C) followed by rapid cooling until reaching the surface at 20 Ma (present age). The CC-5 kimberlite is also cooling within the PRZ at ~60-35 °C, but the model appears to require intense heating at greater depths than, this means that the conditions modelled do not satisfy the paths. The emplacement of kimberlites followed by sedimentation using the same temperature ranges does not seem to be the case for the DC kimberlites.

The emplacement of kimberlites into active Purana sedimentary basins and the subsequent burial of the pipes is observed from Figure 13. The kimberlite pipes were buried (heating to greater depths) for a period of 500-550 Ma. Following this, is a period of slow cooling between 600 Ma and 200 Ma, and then a period of drastic cooling begins at 175 Ma: this is related to the period of Gondwana separation.

From our t-T models, it is observed that the EDC has been uplifting and eroding since the onset of the Jurassic and also, after 175 Ma the cooling rate is slower, most likely related to the strong period of uplift and erosion. The Siddanpalle (SK-1/2) kimberlite pipe cools faster than the Chigicherla pipe mainly because the pipe is not as wide (100 m × 65 m) compared to the Chigicherla (CC-5) pipe which is two times wider (220m × 70 m) than the Siddanpalle pipe. This implies that before the uplift period of the EDC, the Siddanpalle pipe was already closer the

surface than the Chigicherla pipe. Therefore the uplift period brought the Siddanpalle pipe closer to the surface, erosion leading to the current exposure of root zones gave rise to faster cooling signal observed in our HeFTy models. We infer the erosion model for the EDC to be Model is C, this model is concordant with the Proterozoic and Phanerozoic geologic history of the EDC of southern India. Kimberlite emplacement in southern India occurred during the assembly of Rodinia between 1300 Ma and 900 Ma (Li et al., 2008). The period of marine sedimentation between 1600 Ma and 800 Ma can be related to the assembly and breakup of Rodinia whilst forming the Gondwana supercontinent.

4.3 *Constraints on the uplift and erosion history of Peninsular India*

The breakup of Gondwana occurred in three main episodes (Hawkesworth et al., 1999). The initial rifting commenced in the Early Jurassic period (180 Ma) when eastern and western Gondwana separated creating a seaway separating South America and Africa from Antarctica, Australia, India and New Zealand. The second stage occurred in the Early Cretaceous period (130 Ma) when South America separated from the African-India plate and the African-India plate itself from Antarctica. The third stage took place in the Late Cretaceous (92-100 Ma) when Australia and New Zealand became separated from Antarctica northwards away from Africa and Antarctica (Murthy et al., 2012).

Here we present plate reconstructions which were modelled using GPlates software (work done in collaboration with Dr. B. Eglington of the University of Saskatchewan). The aim is to correlate plate movements with the associated uplift and erosion of southern India during the Mesozoic-Cenozoic. Figure 14 shows selected plate tectonic reconstructions from 180 Ma to 40 Ma, with a focus on the drift of the Indian plate relative to neighbouring West Gondwanan continents such as Africa and Madagascar (i.e., Africa was held stationary through time). These plate tectonic reconstructions illustrate the separation of India from Africa towards its current position in the Northern Hemisphere. Reconstructions are shown in increments of 5 or 10 Myr for the movement of the Indian plate from the Jurassic period to its current position. The red star depicts southern India (study area).

At 180 Ma, India was still attached to Africa and Madagascar The initial separation of India from Africa began at ca. 165 Ma, but India was still attached to Madagascar, both drifting southward together. The southward movement of India during the Jurassic-Cretaceous was relatively slow; this movement ceased by 115 Ma. India together with Madagascar separated from Antarctica at ca. 120 Ma, and India separated from Madagascar at ca. 110 Ma. Although India resided in the

Southern Hemisphere for most of the Mesozoic as an integral part of Gondwana (Kent & Muttoni, 2008), the Indian tectonic plate drifted towards the Northern Hemisphere after its separation from Madagascar in the Late Cretaceous. The northward movement of India was rapid with speed of 20 cm/a (Pandey & Agrawal, 1999; Kumar et al., 2007) and continued until ca. 60 Ma when it began to collide with Eurasia. By 40 Ma, India had collided with Asia. The fast drift of India after 100 Ma could be a result of the removal of refertilized mantle lithosphere between 175-115 Ma as India was moving southward after its separation from the African plate. This movement of India occurred atop and across the African Superswell, which is considered to be the surface expression of a large thermochemical upwelling or superplume potentially sourced from the core-mantle boundary (Ebinger and Sleep, 1998; Lekic et al., 2012; Braun et al., 2014). Prolonged exposure (i.e. up to 60 Myr) of the Indian Shield cratonic root to the heat and fluid/melt ingress from this superplume may have significantly weakened its stability and caused gradual delamination and sinking of refertilized blocks into the underlying convecting mantle (cf., Tappe et al., 2007; Tappe et al., 2016; Foley, 2008). Although ridge-push and slab-pull are the most critical tectonic parameters that determine the speed of individual plate motions, it has been demonstrated that tectonic plates with high areal proportions of cratonic mantle keels slow down plate velocities (Zahirovic et al., 2015). The Indian tectonic plate has a high proportion of Archean cratonic lithosphere; however, delamination of the anchoring roots upon passage over the African Superswell between 175-115 Ma may have significantly contributed to India's fast drift after 100 Ma. Although similar ideas have been expressed before (Kumar et al., 2007; Griffin et al., 2009), our study provides a new perspective as to the geographic position of cratonic mantle delamination and the response at Earth's surface. Our low-temperature thermochronology data and t-T modeling thereof require a drastic cooling event in the EDC crust at ca. 175 Ma (Figure 13), which is best explained by km-scale uplift and erosion. The onset of this enhanced uplift and erosion episode of the EDC coincides with the above described slow drift of the Indian plate over the African Superswell. Mechanical removal of parts of the cratonic mantle lithosphere may provide a casual link. Interestingly, in our preferred Model C the projected uplift and erosion (i.e. cooling) of the EDC after 100 Ma is rather insignificant (Figure 13e,f), which suggests that Peninsular India had gained most of its elevation during the Jurassic and Early Cretaceous prior to the fast northward drift during the Late Cretaceous and Cenozoic. With regard to the geographic position of cratonic mantle removal, the EDC drift over the African Superswell between 175-115 Ma occurred in the region that is at present occupied by the SW Indian Ocean. Cenozoic oceanic basaltic magmas from this region are isotopically anomalous relative to equivalent lavas from other world ocean basins, i.e. the so-called DUPAL Pb isotope anomaly (Dupre and Allegre, 1983; Hart, 1984). These isotopic anomalies of SW Indian Ocean basalts have been partly ascribed to

contamination of the mantle sources with enriched continental materials (Hart, 1984). Our study suggests that such continental material was introduced into the convecting upper mantle beneath the SW Indian Ocean basin by plume-facilitated delamination of the Indian tectonic plate between 175 and 115 Ma.

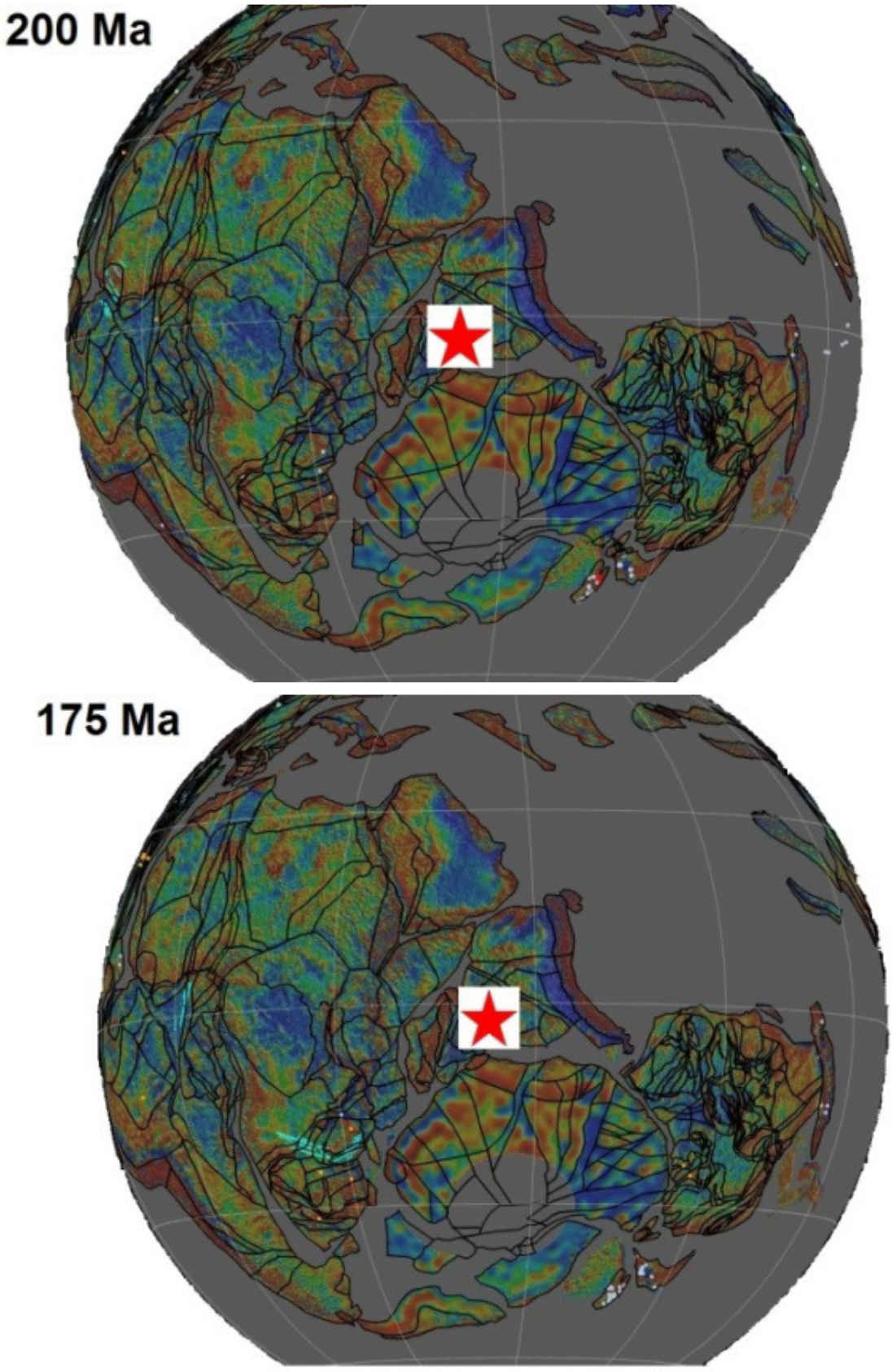

Figure 14a: Representative plate models (GPlates) indicating the movement of the Indian tectonic plate toward its current position in the Northern Hemisphere. At this stage India is still attached to west Gondwana.

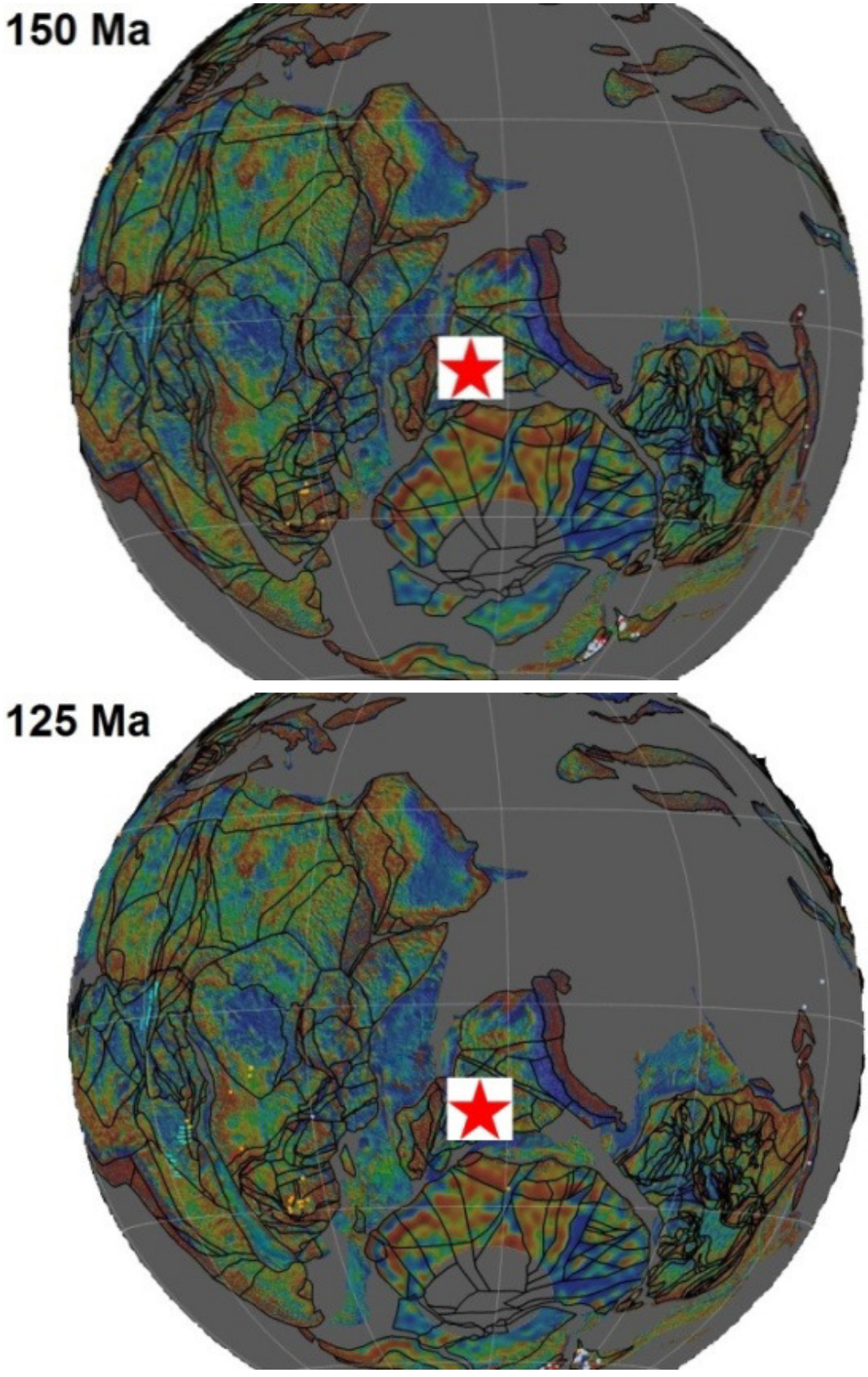

Figure 14b: Representative plate models (GPlates) indicating the southern movement of the Indian tectonic plate since 165 Ma after its breakup from west Gondwana.

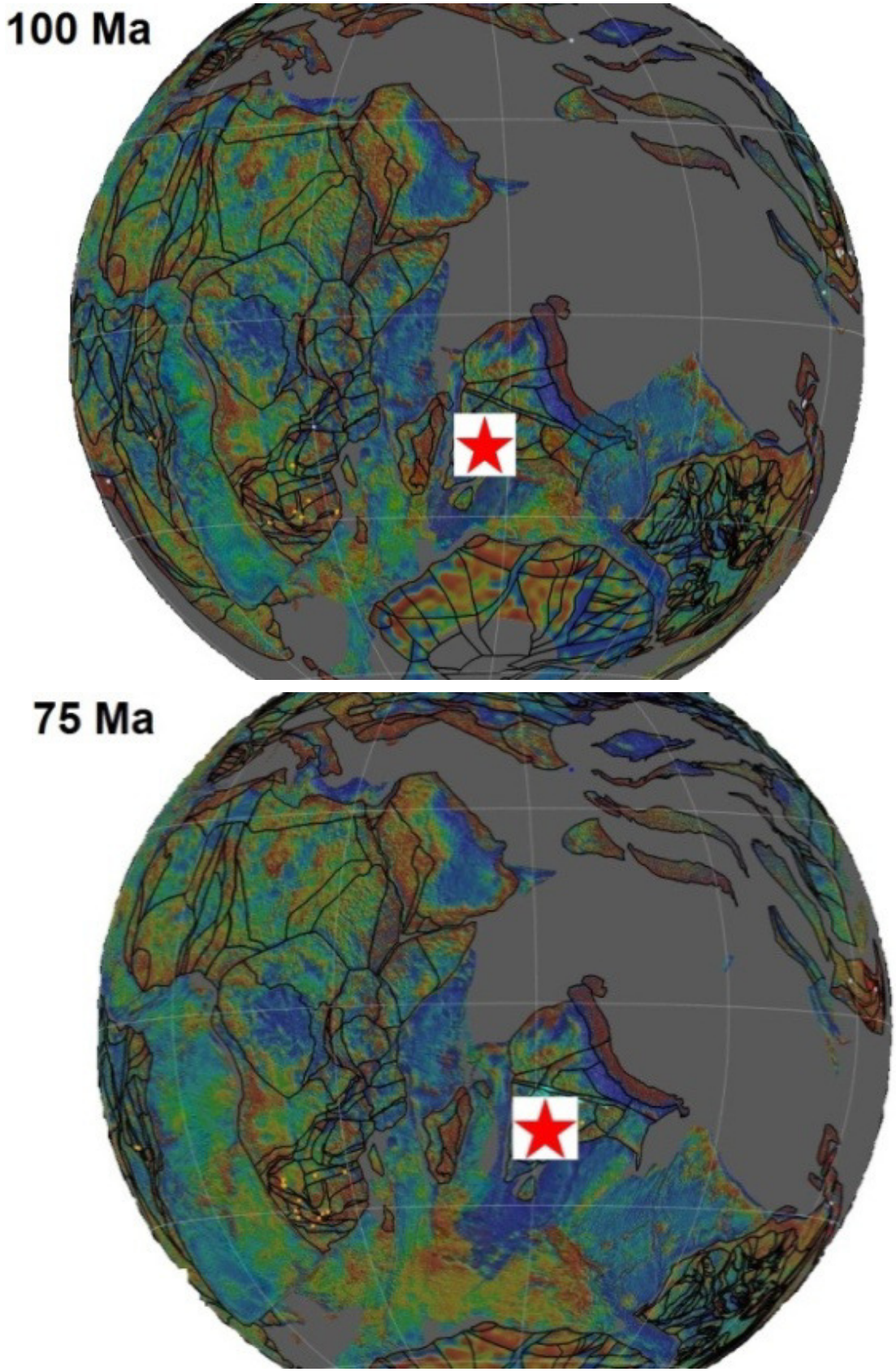

Figure 14c: Representative plate models (GPlates) indicating the rapid speed (20 cm/year) of the Indian tectonic plate toward the north after its separation from Madagascar at 90 Ma.

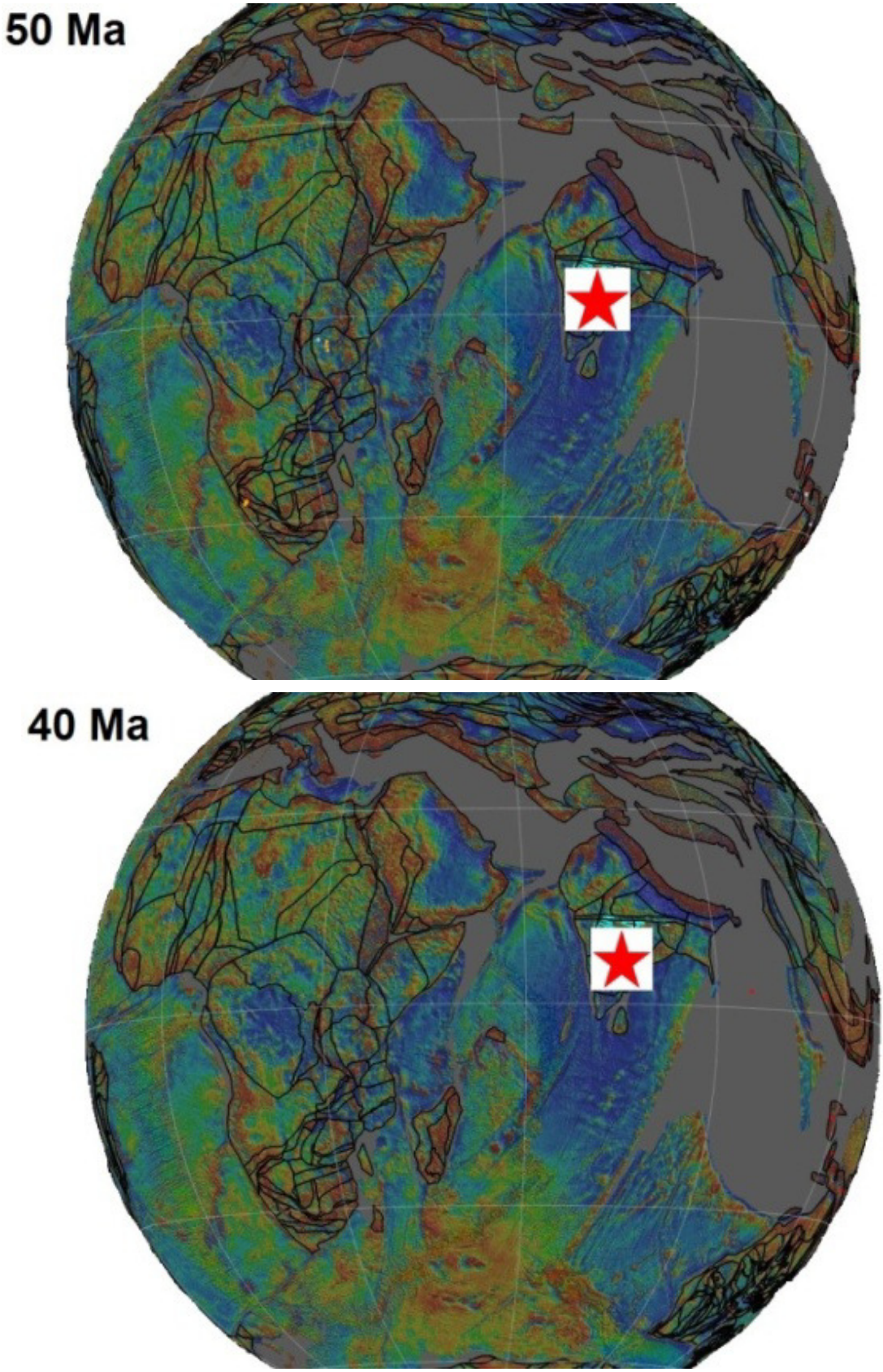

Figure 14d: Representative plate models (GPlates) showing the time period when India was moving northward (90-50 Ma) to collide with Asia (40 Ma) to form the Himalayas.

.

4.4 *Implications for Gondwana break-up and the fast drift of the Indian tectonic plate*

The rapid motion of the Indian plate in the Late Cretaceous period and early Cenozoic era was first recognized from magnetic anomalies on the Central Indian Ridge and Southeast Indian Ridge and later on confirmed by paleomagnetic data (Cande & Stegman, 2011). The fast movement of the Indian plate is a major tectonic puzzle because the velocities of plates are limited by their available driving forces (slab pull and ridge push), and also because plates with high areal extent of continents tend to move slower than the purely oceanic plates (Zahirovic et al., 2015). Although the Indian plate contains coceanic lithosphere offshore, it also contains a significant portion of continental landmass, and it moved faster (18 cm/year) than other Gondwana fragments. The Australian and the African plate moved comparatively shorter distances and at lower speeds of 2-4 cm/year, whereas Antarctica remained almost stationary when Gondwana fragments were separated (Kumar et al., 2007b).

A plausible reason for the fast drift of the Indian plate as compared to the Australian, Antarctica and African plate could also result from the fact that the Indian lithospheric plate has a relatively small area of 15 X 10^6 km^2 (Forsyth & Uyeda, 1975) compared to the other Gondwana fragments. The lithospheric plate of Antarctica covers an area of 61×10^6 km^2, the Australian plate covers an area of 47×10^6 km^2 and the African plate has the largest size (61.3×10^6 km^2) of all these plates. The relatively low speeds of these plates compared with the Indian plate might have been caused by their larger sizes, which hindered fast movements. Some authors relate the fast northward movement of the Indian plate to the subduction of oceanic lithosphere north of India (i.e. Greater India), which closed the Neo-Tethys Ocean. They also relate it to seafloor spreading south of India (double subduction), which created the Indian Ocean (Jagoutz et al., 2015).

Lehmann et al. (2010) discovered a ca. 65 Ma old diamondiferous (Group II) kimberlite in Central India (Bastar Craton) that was synchronous with the Deccan Traps. This may suggest that the lithosphere in the Indian shield was thick at the end of the Cretaceous and therefore India's fast drift to the north before collision with Eurasia cannot be related to its lithospheric thinning during Gondwana break-up starting at 180 Ma (Lehmann et al., 2010; Chalapathi Rao & Srivastava, 2012). However, the current study suggests that the cratonic keel of the Indian lithosphere was partially delaminated as a result of slow plate motion over

the African Superplume during India's separation from the African plate between ca. 175 and 115 Ma.

Lithospheric thinning is common in the cratonic evolution but it is not always associated with craton destruction (Tappe et al., 2007; Tappe et al., 2016); Wu et al., 2014). Most cratons are envisaged to be partially thinned by thermal erosion due to mantle plume activity or mantle upwelling (Bell et al., 2003) which could cause craton destruction (Wu et al., 2014). For example, the evolution of the DC shows geologic records of about 3.6 billion years of which the early evolution is similar to that of the North China Craton (NCC; Wu et al., 2014). However, the Indian Craton unlike the NCC remained stable after its formation (cratonization), i.e. the Proterozoic sedimentary rocks have not been subjected to strong metamorphism and deformation, unlike the NCC that lost its stability due to extensive delamination, magmatism and deformation. For the NCC, xenoliths entrained in the Ordovician kimberlites are indicative of a mantle typical of cratonic character and composition, whilst later Mesozoic-Cenozoic basalts brought up non-cratonic peridotite xenoliths from beneath the NCC crust (Foley, 2008; Wu et al., 2014). This brackets NCC lithosphere removal to a short time in the Late Cretaceous to Early Tertiary (Foley, 2008).

Geophysical and geochemical observations suggest that a significant portion of the continental lithosphere has been recycled into the deeper mantle (Naganjaneyulu & Santosh, 2012) e.g. seismic observations which provide snapshots for present day lithosphere removal events, reveal that the mantle lithosphere is unusually thin beneath cratonic India (LAB at 80-100 km). The separation of Gondwana by a mantle plume could have also affected the lithosphere of the DC. When a plume rises beneath a thick (cold) craton (150-300 km) such as the DC, a little or no partial melting (Figure 15c) may occur near its base, which is largely, refractory in nature. This inhibits passage of the plume-head through cratonic lithosphere. Figure 15 shows the suggested model of lithosphere delamination by a plume impinging on the base of the cratonic lithosphere (modelled after Pandey & Agrawal, 1999; Raval & Veeraswamy 2003). Pandey and Agrawal (1999) stated that 'Persistent thermal reactivations caused by the presence of higher radioactivity and lithophilic elements since at least 1.5 Ga, coupled with Late Cretaceous geodynamic events, have resulted in higher heat flows and large-scale lithospheric mantle root deformation and consequent weakening in the Indian landmass'.

As suggested by various studies (xenoliths, MT and seismic studies), the lithosphere beneath the DC was once thicker extending to within the diamond stability field (Ganguly &

Bhattacharya;1987, Griffinet al., 2009; Kumar et al., 2007b; Naganjaneyulu & Santosh, 2012). Figure 15a shows the cratonic root of the DC (not to scale) and Figure 15b shows the mantle plume situated beneath the DC during rifting of the Indian plate from the African plate. Figure 15c shows plume interaction with the cratonic mantle. We suggest that, based on t-T modelling of our AHe data for 1.1 Ga EDC kimberlites, rifting of the Indian plate from Africa has led to lithospheric removal beneath India by thermal reactivations. As the continents drifted apart, the upwelling mantle pushed onto the base of the lithosphere, which resulted in partial melting of the cratonic roots and therefore deformation.

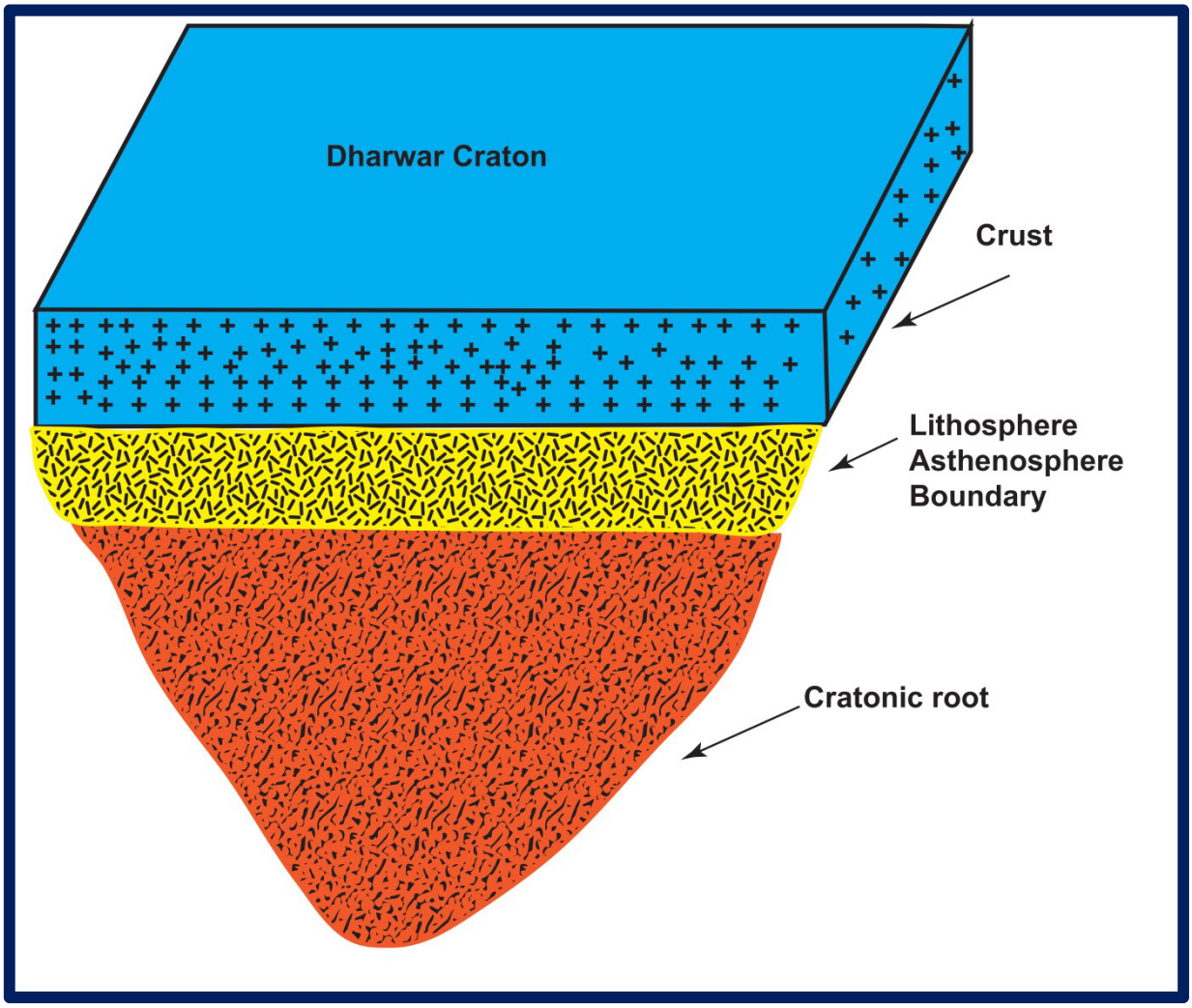

Figure 15(a): Model for the lithosphere delamination: schematic diagram for the Dharwar Craton showing cratonic root.

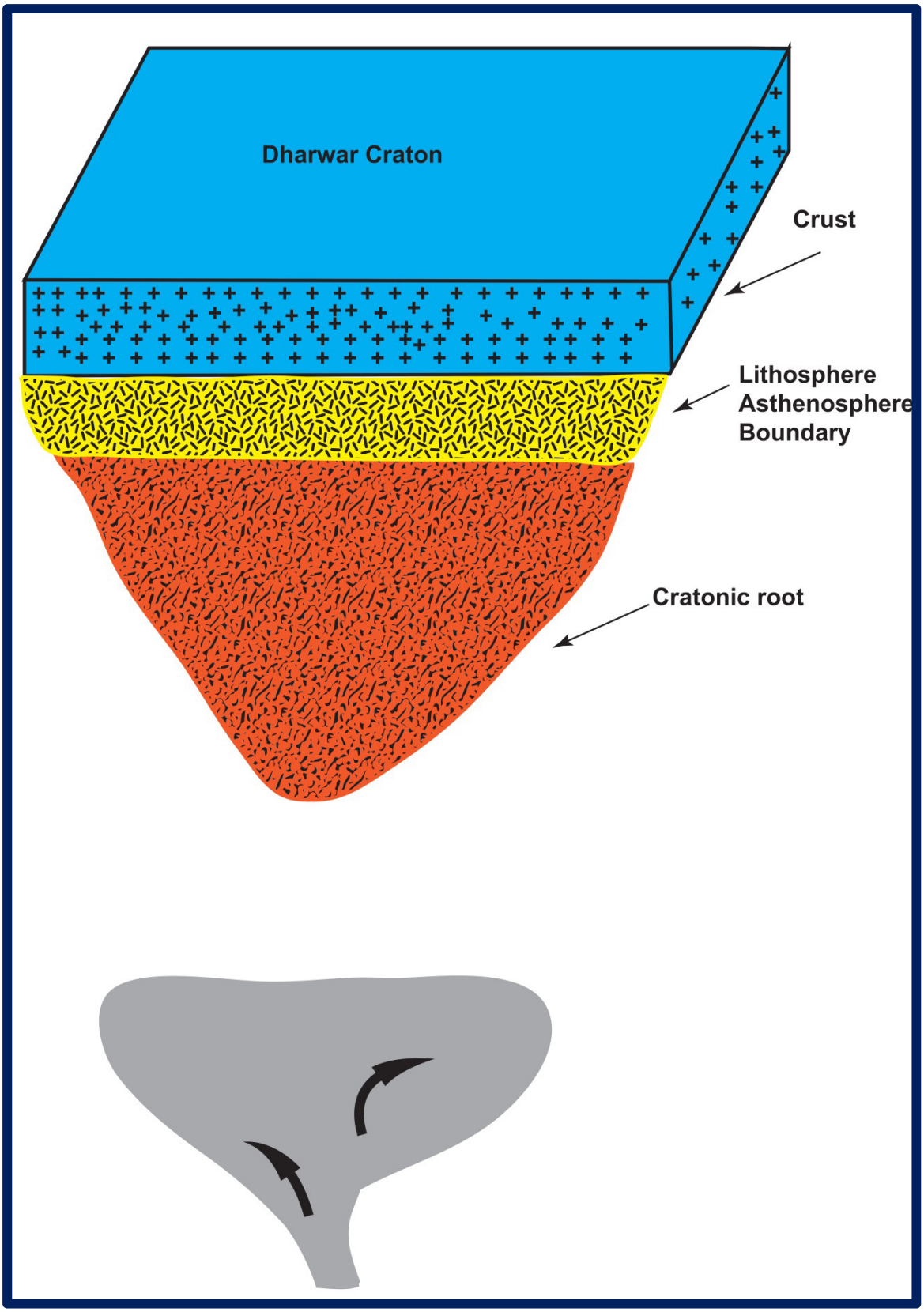

Figure 15(b): Model for the lithosphere delamination: Plume beneath the Dharwar Craton.

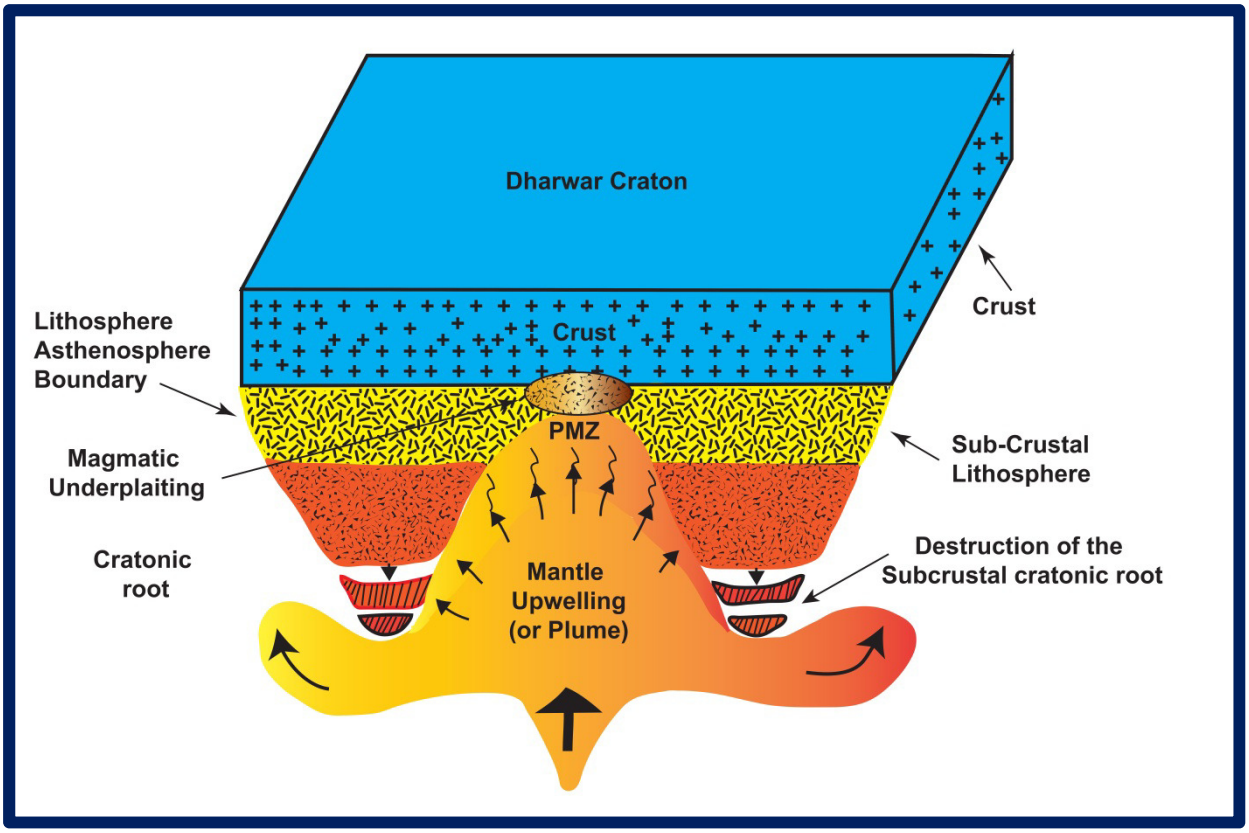

Figure 15(c): Model for the lithosphere delamination: The interaction of the plume with lithosphere leading to cratonic root destruction after Pandey & Agrawal (1999) and Raval & V Veeraswamy (2003). Partial Melting Zone- (PMZ).

The breakup of Gondwana caused the Indian lithosphere to have certain characteristics. This includes the three continental breakups, from Antarctica to Australia at 130 Ma, from Madagascar (90 Ma) to Seychelles at 65 Ma. Also, the three –four mantle plume activities and the development of LIPs during the early Cretaceous intrusives that is over the Rajmahal Traps (117 Ma), the Mid-Cretaceous volcanism over Madagascar and the over the southern Indian Shield (90 Ma) including the world famous Deccan basalts of 65 Ma (Raval & Veeraswamy, 2003).

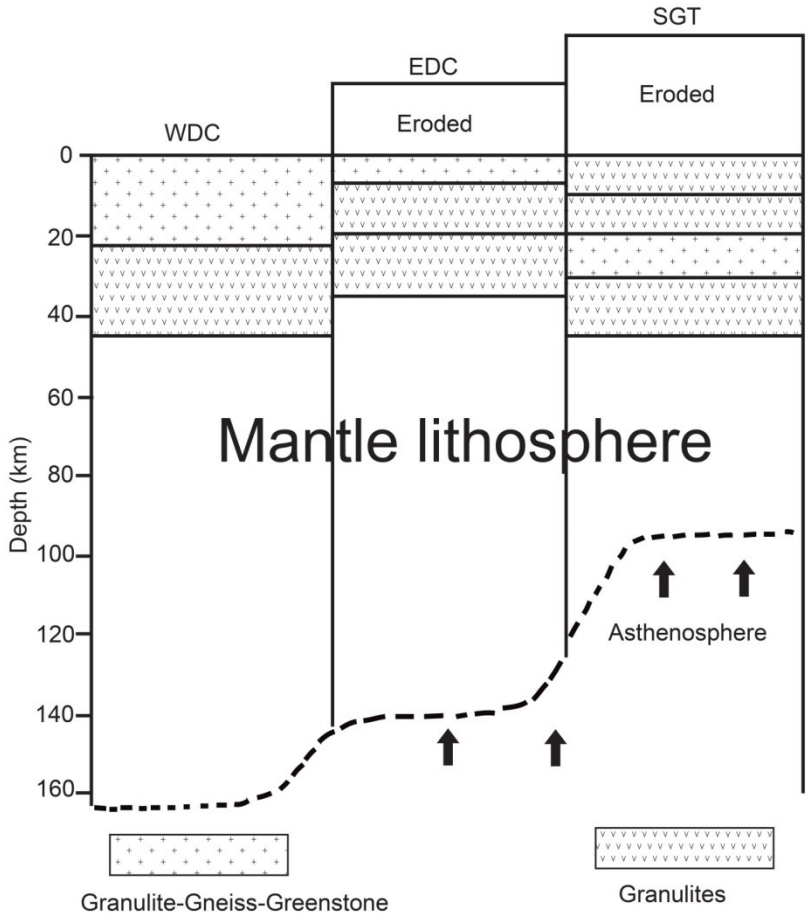

Figure 16: A lithosphere-scale cross section through the EDC, WDC and SGT, inferred from available geological and geophysical data. Adapated from Agrawal & Pandey (2004).

It is generally accepted that plume-lithosphere interactions produce continental flood basalts (Pandey & Agrawal, 1999), and the structures overlying the plume will get modified. Interaction will mostly be concentrated along mobile belts and plume heads will be deflected to areas of thin lithosphere, probably at the margins of cratons (Thompson and Gibson, 1991; Foley, 2008; Tappe et al., 2016)). Indeed, it was recognized that during Gondwana dispersion, separation of India has taken place along its mobile belts with contemporaneous plume activity (Raval & Veeraswamy, 2003).

As the Indian plate continued its southward movement subsequent to its break-up from the African plate beginning at ca. 175 Ma, it passed over the long lived Réunion plume which is envisaged to have aided in delamination of the lithosphere by further melting and infiltrating the Indian cratonic mantle lithosphere. Resultant partial lithosphere delamination then aided the rapid movement of India towards Eurasia. Erosion in the EDC removed the thick column of Purana sedimentary rocks and greenstone sequences leaving only remnants at the surface (Figure 16) (Agrawal & Pandey, 2004).

We support the notion that the Indian plate moved faster (Pandey & Agrawal, 1999) due to lithosphere thinning as suggested by Kumar et al. (2007b). These authors proposed that the Indian lithospheric thickness was modified during northward movement over the Marion, Kerguelen and Réunion hotspots, which were also involved with the separation of India from its Gondwana parts (Pandey & Agrawal, 1999). However, our AHe data and t-T modelling thereof suggest that the Indian lithosphere was already thinned significantly earlier during its southward drift across the African Superswell between 175 and 115 Ma. Therefore, the continental portion of the Indian tectonic plate was relatively thin before commencing its northward movement; and this modified lithospheric architecture may have contributed to the fastest plate motion on record.

5 Concluding Remarks

Mesoproterozoic kimberlites of the Dharwar Craton are characterized by an inequigranular texture imparted on the rock by the presence of two generations of olivine (macrocrysts and microcrysts); in most cases the olivine grains are serpentinized. The groundmass minerals are serpentine, spinel group minerals, phlogopite, perovskite, ilmentite and apatite. The CC-5 kimberlite is characterized by autoliths, the SK-1 and SK-2 kimberlites are carbonate-rich. Based on the petrographic descriptions, mineral chemical composition analysis and discrimination plots, the samples analysed in this study are truly kimberlitic.

Apatites from these samples were extracted for (U-Th)/He thermochonology analysis, in order to determine the rate of cooling and uplift in the Dharwar Craton. The obtained AHe ages are all younger than pipe emplacement, indicative of an erosion event following emplacement of kimberlites. The CC-5 kimberlites of the WKF yielded a mean age of 164.9 ± 21.2 Ma, while the SK-1/2 kimberlites of the RKF yielded a combined mean age of 145.7 ± 21.2 Ma. Both dates suggest an uplift, erosion and cooling event in the EDC crust in the Jurassic. Modelling is consistent with the known tectonic history (development) of the southern Indian shield, in that kimberlites were emplaced into the stable interior of the eastern Dharwar Craton. Subsequent burial (heating) within the Siddanpalle kimberlites shows a greater temperature increase which demonstrates the kimberlites were buried faster and possibly deeper than the Chigicherla kimberlites. This would likely be the result of the Siddanpalle kimberlites being more distal to the depocenter margin and the Chigicherla kimberlite being more proximal. The burial period between 1100 Ma and 850 Ma is associated with the breakup of Rodinia and coincident rifting such as continued Purana basin development. During Gondwana amalgamation (with Purana basin inversion), both EDC kimberlite occurrences record cooling; with the Chigicherla kimberlites cooling faster than the Siddanpalle kimberlites. The Siddanpalle kimberlites experienced more rapid cooling and uplift (erosion) likely because they were more proximal to the axis of basin inversion. During Gondwana quiescence both areas thermally equilibrated.

Both the SK-1/2 and the CC-5 kimberlites, although from the same craton have experienced different erosional histories. The Siddapnalli pipe has an estimated denudation of 2.2 km whilst the CC-5 kimberlite pipe is denuded to 2.6 km since the Neoproterozoic to present; both these pipes are currently exposing the root zone, 1 km and 1.5 km respectively. The different dimensions of the pipe played a role in the different cooling and denudation rates, the Chigicherla pipe was deep in comparison to the Siddanpalle pipe which had a shallower depth, thereby making it more liable to erosion and cooling. The emplacement of kimberlites into active

Purana basins, the subsequent burial and later unroofing event has implications for the provenance of alluvial diamonds in India. Major uplift in southern India occurred by isostatic balance during break up of Gondwana. Subsequent to Gondwana separation, the Indian plate attained a high speed of 18 cm/yr before colliding with Eurasia, which most authors believe is related to the plume that separated Gondwana.

Plate tectonic reconstruction shows the slow southward movement of the Indian plate between 180-150 Ma. Separation of Madagascar from India is related to the fast drift of the Indian plate at 100 Ma. It took India ~100 Myr to drift southward and only 40 Myr to move from the Southern Hemisphere to the Northern Hemisphere (current position). Although theories exist on forces acting on plates, the Indian plate moved anomalously fast (18 cm/yearr). The Zahirovic et al. (2015) notion of oceanic plates moving faster than continental ones does not apply to the Indian plate. Therefore, there must be other factors that affected the fast drift of the Indian plate to the north. We suggest that during Gondwana breakup, the Indian lithosphere was partially melted by the plume that separated Gondwana, as India drifted southward passing over hotspots removal of the lithosphere occurred as the Indian plate passed over the Reunion hotspot which further modified the lithosphere, thereby causing India to attain a high speed during the Late Cretaceous

6 References and Bibliography

Acharyya, S. K. (2000). Breakup of Australia-India-Madagascar Block, Opening of the Indian Ocean and Continental Accretion in Southeast Asia With Special Reference to the Characteristics of the Peri-Indian Collision Zones. Gondwana Research, 3 (4), 425-443.

Agrawal, P. K., & Pandey, O. P. (2004). Unusual lithospheric structure and evolutionary pattern of the cratonic segments of the South Indian shield. Earth Planet Space, 56, 139-150.

Ault, A. K., Flowers, R. M., & Bowring, S. A. (2013). Phanerozoic surface history of the Slave Craton. Tectonics , 32 (doi:10.1002/tect.20069), 1066-1083.

Balasubrahmanyan, M. N. (2006). GEOLOGY AND TECTONICS OF INDIA: AN OVERVIEW, Issue 9 of IAGR memoir. International Association for Gondwana Research.

Balfour, I. (2000). Famous diamonds. London: Christie Manson & Woods Ltd.

Basu, A., & Bickford, M. E. (2015). An alternate perspective on the Opening and Closing of the Intracratonic Purana basins in Peninsular India. Geological Society of India, 85, 5-25.

Bell, D. R., Schmitz, M. D., & Janney, P. E. (2003). Mesozoic thermal evolution of the southern African mantle lithosphere. Lithos, 71, 273-287.

Beyer, C., Bernndt, J., Tappe, S., & Klemme, S. (2013). Trace element partitioning between the perovskite and kimberlite to carbonatite melt: New experimental contsraints. *Chemical Geology , 353*, 132-139.

Biswas, S. K. (2007). Mineral Prospecting. Geological Survey of India, 199-206.

Boyden, J. A., Muller, R. D., Gurnis, M., Torsvik, T. H., Clark, J. A., Turner, M., et al. (2011). Next-generation plate-tectonic reconstructions. Solid Earth Sciences, 95, 95-114.

Braun, J., Guillocheau, F., Robin, C., Baby, G., & Jelsma, H. (2014). Rapid erosion of the Southern African Plateau as it climbs over a mantle superswell. Journal of Geophysical Research, 119, 6093-6112.

Brown, R. J., & Valentine, G. A. (2013). Physical characteristics of kimberlite and basaltic intraplate volcanism and implications of a biased kimberlite record. Geological Society of America Bulletin (doi:10.1130/B30749.1).

Cande, S. C., & Stegman, D. R. (2011). Indian and African plate motions driven by the push force of the Reunion plume head. Nature, 475 (doi:10.1038/nature10174), 47.

Catherine, J. K., & Pandey, O. P. (2005). Differential uplift between Hyderabad and Bangalore geotectonic blocks of Eastern Dharwar Craton, south India. Journal of Geological Society of India, 65, 493-496.

Chalapathi Rao, N. V. (2005). A petrological and geochemical reappraisal of the Mesoproterozoic diamondiferous Majhgawan pipe of central India: evidence for

transitional Kimberlite-Orangeite (group II kimberlite) - lamproite rock type. Mineralogy and Petrology, 84, 69-106.

Chalapathi Rao, N. V., & Dongre, A. A. (2010). Carbonate xenoliths hosted by the Mesoproterozoic Siddanpalli Kimberlite Cluster (Eastern Dharwar craton): implications for the geodynamic evolution of southern India and its diamond and uranium metallogenesis. International Journal of Earth Sciences, 99, 1791-1804.

Chalapathi Rao, N. V., & Dongre, A. N. (2009). Mineralogy and Geochemistry of Kimberlites NK-2 and KK-6, Narayanpet Kimberlite Field, eastern Dharwar Craton, southern India: evidence for a transitional kimberlite signature. The Canadian Mineralogist, 47, 1117-1135.

Chalapathi Rao, N. V., & Lehman, B. (2011). Kimberlites, flood basalts and mantle plumes: New insight from the Deccan Large Igneous Province. Earth-Science Reviews, 107, 315-324.

Chalapathi Rao, N. V., & Lehman, B. (2011). Petrogenesis of the Crater-facies Topakal Kimberlite Pipe, Indravati Basin, Central India. Geoscince Frontiers, 1-10.

Chalapathi Rao, N. V., & Srivastava, K. J. (2012). Kimberlites, Lamproites, Lamprophyres, their Entrained Xenoliths, Mafic Dykes and Dyke Swarms: Highlights of Recent Indian research. Proc Indian nant Sci Acad, 78 (3), 431-444.

Chalapathi Rao, N. V., & Srivastava, R. K. (2009). Petrology and geochemistry of diamondiferous Mesoproterozoic kimberlites from Wajrakarur kimberlite field, Eastern Dharwar craton, Southern India: genesis and constraints on mantle source regions. Contributions to Mineral petrology, 157, 245-265.

Chalapathi Rao, N. V., Dongre, A., Wu, F.-Y., & Lehmann, B. (2015). A Late Cretaceous (ca. 90 Ma) kimberlite event in southern India: Implications for sub-continental lithospheric mantle evolution and diamond exploration. Gondwana Research, doi: 10.1016/j.gr.2015.06.006.

Chalapathi Rao, N. V., Gibson, S. A., Pyle, D. M., & Dickin, A. P. (2004). Petrogenesis of Proterozoic Lamproites and Kimberlites from the Cuddapah Basin and the Dharwar Craton, Southern India. Journal of Petrology, 45 (5), 907-948.

Chalapathi Rao, N. V., Kamde, G., Kale, H. S., & Dongre, A. (2010). Petrogenesis of Proterozoic Lamproites from the Krishna Valley, Eastern Dharwar Craton, Southern India. Journal of Petrology, 177, 103-130.

Chalapathi Rao, N. V., Kumar, A., Sahoo, S., & Dongre, A. N. (2014). Petrology and petrogenesis of Mesoproterozoic lamproites from the Ramadugu field, NW margin of the Cuddapah basin, Eastern Dhawar Craton, southern India. Lithos, 196-197, 150-168.

Chalapathi Rao, N. V., Lehmann, B., Panwar, B. K., Kumar, A., & Mainkar, D. (2014). Petrogenesis of the crater-facies Topakal kimberlite pipe, Indravati Basin, Central India. Geoscience Frontiers, 5, 781-790.

Chalapathi Rao, N. V., Wu, F. Y., Mitchell, R. H., & Li, Q. L. (2013). Mesoproterozoic U-Pb ages, trace element and Sr-Nd isotopic composition of perovskite from kimberlites of the

eastern Dharwar craton, Southern India: Distinct mantle sources and widespread 1.1 Ga tectonomagmatic event. Chemical Geology, 353, 48-64.

Chaudhuri, A. S., Saha, D., Deb, G. K., Deb, S. P., Mukherjee, M. K., & Ghosh, G. (2001). The Purana Basins of Southern Cratonic Province of India-A case of Mesoproterozoic Fossil Rifts. Gondwana Research, 5 (1), 23-33.

Cherniak, D. J., Watson, E. B., & Thomas, J. B. (2009). Diffusion of helium in zircon and apatite. Chemical Geology, 268, 155–166.

Clement, C. R., & Skinner, E. M. (1985). A textural-genetic classification of kimberlites. Transactions of the Geological Society of South Africa, 403-409.

Clement, C. R., Skinner, E. M., & Scott Smith, B. H. (1984). Kimberlite redefined. Journal of Geology, 23, 223-228.

Collins, A. S., Clark, C., & Plavsa, D. (2014). Peninsular India in Gondwana: The tectonothermal evolution of the Southern Granulite Terrain and its Gondwanan counterpart. Gondwana Research, 25 (1), 190-203.

Collins, A. S., Patranabis-Deb, S., Alexander, E., Bertram, C. N., Falster, G. M., Core, R. J., et al. (2014). Detrital mineral age, radiogenic isotopic stratigraphy and tectonic significance of the Cuddapah Basin, India. Gondwana Research,

http://dx.doi.org/10.1016/j.gr.2014.10.013

Dupre, B., & Allegre, C. J. (1983). PB-SR ISOTOPE VARIATION IN INDIAN-OCEAN BASALTS AND MIXING PHENOMENA. Nature, 303, 142-146.

Ebigner, C. J., & Sleep, N. H. (1998). Cenozoic magmatism throughout east Africa resulting from impact of a single plume. Nature, 395, 788-791.

Ehlers, T. A., & Farley, K. A. (2003). Apatite (U-/Th)He thermochronometry : methods and applications to problems in tectonic and surface processes. Elsevier, 206, 1-14.

Ehlers, T. A., & Farley, K. A. (2003). Apatite (U-Th)/He thermochronometry: methods and applications to problems in tectonic and surface problems. Earth and Planetary Science Letters, 206, 1-14.

Fareduddin, & Mitchell, R. (2012). Diamonds and their Source rocks in India (First ed.). Bangalore: Geological Society of India.

Fareeduddin, & Mitchell, R. H. (2012). Diamonds and their source rocks in India (First ed.). Bangalore: Geological Society of India.

Farley, K. A., & Stockli, D. F. (2002). (U-Th)/He dating of Phosphates: Apatite, Monazite, and Xenotime. Reviews in Mineralogy and Geochemistry, 48 (1), 559-577.

Flowers, R. M., & Kelly, S. A. (2011). Interpreting data dispersion and "inverted" dates in apatite (U-Th)/He. Geochimica et Cosmochimica Acta, 75, 5169-5186.

Flowers, R. M., Ketcham, R., Shuster, D., & Farley, K. A. (2009). Apatite (U-Th)/He thermochronometry using a radiation damage accumulation and annealing model. Geochimica et Cosmochimica Acta , 73, 2347-2365.

Foley, S. F. (2008). Rejuvination and erosion of the cratonic lithosphere. Nature Geoscience, 1, 503-510.

Forsyth, D., & Uyeda, S. (1975). On the Relative Importance of the Driving Forces of Plate Motion . Geophys. J. R. asr. coc, 43, 163-200.

Ganguly, J., & Bhattacharya, P. K. (1987). Xenoliths in Proterozoic kimberlites from southern India: petrology and geophysical implications. In P. H. Nixon (Ed.), Mantle xenoliths (p. 17). Wiley-Interscience.

Grifffin, W. L., Kobussen, A. F., Babu, E. V., O'Reilly, S. Z., Norris, R., & Sengupta, P. (2009). Craton, A translithospheric suture in the vanished 1-Ga lithospheric root of South India: Evidence from contrasting lithosphere sections in the Dharwar. Lithos, 1109-1119.

Griffin, W. L., Kobussen, A. F., Babu, E. V., O'Reilly, S. Y., Norris, R., & Sengupta, P. (2009). A translithospheric suture in the vanished 1-Ga lithospheric root of South India: Evidence from contrasting lithosphere sections in the Dharwar Craton. Lithos, 112S, 1109-1119.

Gunnell, Y., Gallagher, K., Carter, A., Widdowson, M., & Hurford, A. J. (2003). Denudation history of the continental margin of western peninsular India since the early Mesozoic - reconciling apatite ¢ssion-track data with geomorphology. ESPL (doi:10.1016/S0012-821X(03)00380-7).

Haggerty, S. E., & Birkett, T. (2004). Geological setting and chemistry of kimberlite clan rocks in the Dharwar Craton, India. Lithos, 76, 535-549.

Haggerty, S. E., & Birkett, T. (2004). Geological setting and chemistry of kimberlite clan rocks in the Dharwar Craton, India. Lithos, 76, 535-549.

Harris, P. G., & Middlemost, E. A. (1969). The evolution of kimberlites. Lithos, 3, 77-78.

Hart, S. R. (1984). A large-scale isotope anomaly in the Southern Hemisphere mantle. Nature, 309, 753-757.

Hawkesworth, C., Kelly, S., Turner, S., Le Roex, A., & Storey, B. (1999). Mantle processes during Gondwana break-up and dispersal. Journal of African Earth Sciences, 28 (1), 239-261.

Hawthorne, J. B. (1975). Model of a kimberlite pipe. Phys Chem Earth , 9, 1-15.

Jagoutz, O., Royden, L., Holt, A. F., & Becker, T. W. (2015). Anomalously fast convergence of India and Eurasia caused by double subduction. Nature, 8, DOI:10.1038/NGE02418.

Joy, S., Jelsma, H., Tappe, S., & Armstrong, R. (2015). SHRIMP U-Pb zircon provenance of the Sullavai Group of Pranhita-Godaravi Basin and Bairenkoda Quatzite of Cuddapah Basin, with implications for the Southern Indian Proterozoic tectonic architecture. Journal of Asian Earth Sciences (http://dx.doi.org/10.1016/j.jseas.2015.07.023)

Kale, V. S., & Phansalkar, V. G. (1991). Purana Basins of peninsular India: A review. Basin Research, 3, 1-36.

Karmalkar, N. R., Duraiswami, R. A., Chalapathi Rao, N. V., & Paul, D. K. (2009). Mantle-derived Mafic-ultramafic Xenoliths and the Nature of Indian Sub-continental Lithosphere. JOURNAL GEOLOGICAL SOCIETY OF INDIA, 73, 657-679.

Kent, D. V., & Muttoni, G. (2008). Equatorial convergence of India and early Cenozoic climate trends. PNAS, 105 (42), 16065-16070.

Kent, R. (1991). Lithospheric uplift in the eastern Gondwana: evidence for a long-lived mantle plume system? The Geological Society of America, 19, 19-23.

Ketcham, R. A. (2005). Foward and Inverse Modeling of Low-Temperature Thermochronometry Data. Reviews in Mineralogy and Geochemistry, 58 (11), 275-314.

Kirkley, M. B., Gurney, J. J., & Levinson, A. A. (1991). Age, Origin, and emplacement of Diamonds: Scientific Advances in the last Decade. Gemological Institute of America, 27 (1), 2-25.

Kjarsgaard, B. A., Pearson, D. G., Tappe, S., Nowell, G. M., & Dowall, D. P. (2009). Geochemistry of hypabbysal kimberlites from the Lac De Gras, Canada: Comparisons to a global database and applications to the parent magma problem. Lithos, 112S, 236-248.

Kumar, A., Heamn, L., & Manikyamba, C. (2007a). Mesoproterozoic kimberlites in south India: A possible link to ~1.1 Ga global magmatism. Precambriam Research, 154, 192-204.

Kumar, P., Yuan, X., Kumar, M. R., Kind, R., Li, X., & Chadha, R. K. (2007b). The rapid drift of the Indian tectonic plate. Nature, 449 (doi:10.1038/nature06214), 894-897.

Kumar, V. P., Prakasam, K. S., Rai, S. S., & Gupta, S. (2015). Upper-mantle anisotropy beneath the south Indian Shield: Influenced by ancient and recent Earth processes. Lithosphere, 7 (2), 108-116.

Lehmann, B. (2010). Diamondiferous kimberlites in central India syncronous with Deccan flood basalts. Earth and Planetary Science Letters, 290, 142-149.

Lekic, V., Cottaar, S., Dziewonski, A., & Romanowics, B. (2012). Cluster analysis of global lower mantle tomography: A new class of structure and implications for chemical heterogeneity. Earth and Planetary Science Letters, 357, 68-77.

Li, Z. X., Bogdanova, S. V., Collins, A. S., Davidson, A., De Waele, B., Ernst, R. E., et al. (2008). Assembly, configuration, and break-up history of Rodinia: A synthesis. Precambrian Research, 160, 179-210.

Lisker, F., Ventura, B., & & Glasmacher, U. A. (2009). Apatite thermochronology in modern geology (324 ed.). London: Geological Society.

Lorenz, V., & Kurszlaukis, S. (2007). Root zone processes in the phreatomagmatic pipe emplacement model and consequences for the evolution of maar-diatreme volcanoes. Journal of volcanology and Geothermal Research, 159, 4-32.

Lynn, M., Joy, S., & Preston, R. (2013). The Geology and Geochemistry of the Wadagera Kimberlite and Characteristics of the Underlying Subcontinental Lithosphere Mantle, Dharwar Craton, India. In Proceedings of the 10th International Kimberlite Province (pp. 167-181). Bangalore: Society of India.

Mahadevan, T. M. (2013). Evolution of the Indian Continental Lithosphere: Insights from episodes of crustal evolution and geophysical models. Journal of Indian Geophysics, 17 (1), 9-38.

Mainkar, D., Gupta, T., Patel, S. C., Lehmann, B., Diwan, P., Kamisky, F. V., et al. (2013). Diamonds from the Behradih Kimberlite Pipe, Bastar Crtaon, India: A Reconnaissance Study. In D. G. Pearson, H. S. Grütter, J. W. Harris, B. A. Kjarsgaard, H. O'Brien, N. V. Chalapathi Rao, et al. (Eds.), Proceedings of 10th International Kimberlite Conference (10.1007/978-81-322-1170-9_20 ed., p. Volume 1). Special Issue of the Journal of the Society of India.

Mainkar, D., Lehman, B., & Haggerty, S. E. (2004). The crater-facies kimberlite system of Topakal, Bastar District, Chhattisgarh, India. Lithos, 76, 201-217.

Mandal, S. K., Fellin, M. G., Burg, J., & C, M. (2015). Phanerozoic surface history of southern Peninsular India from apatite (U-Th-Sm)/He data. Geochemistry, Geophysics, Geosystem (DOI 10.1002/2015GC005977).

Mange, M. A., & Maurer, H. (1992). Heavy Minerals in Colour (First ed.). London: Chapnam and Hall.

Marks, M. A., Wenzel, T., Whitehouse, M. J., Loose, M., Zack, T., Barth, M., et al. (2012). The volatite inventory (F, Cl, Br, S, C) of magmatic apatite: An integrated analytical approach. Chemical Geology, 291, 241-225.

Mazumder, R., & Saha, D. (2012). Paleoproterozoic of India. In Paleoproterozoic sedimentation in the Cuddapah Basin, south India and regional tectonic: a review (p. 289). United Kingdom: Geological Society of London.

Miller, J. S., Santosh, M., & Pressley, R. A. (1996). A Pan-African Thermal event in southern India. Journal of Southeast Asian Earth Sciences, 14 (3/4), 127-136.

Mitchell, R. H. (1995). Kimberlites, Orangeites and Related Rocks. New York: Plenum Press.

Mitchell, R. H. (1995). Kimberlites: Mineralogy, Geochemistry and Petrology. New York: Plenum Press.

Mitchell, R. H. (2008). Petrology of Hypabyssal kimberlites: relevance to primary magma compositions. Journal of Volcanology and Geothermal Research, 174, 1-8.

Murthy, D. S., & Dayal, A. M. (2001). Geochemical characteristics of kimberlite rocks of the Anatapur and Mahbubnagar districts, Andra Pradesh, South India. Journal of Asian Earth Sciences, 19, 311-319.

Murthy, K. S., Subrahmanyan, A. S., & Subrahmanyan, V. (2012). Tectonics of the eastern continental margin of India. New Delhli: The Energy and Resources Institute (TERI).

Naganjaneyulu, K., & Santosh, M. (2012). The nature and thickness of the lithosphere beneath the Archean Dharwar Craton, South India: A magnetotelluric model. Journal of Asian Earth Sciences, 49, 349-361.

Osborne, I., Sherlock, S., Anand, M., & Argles, T. (2011). New Ar-Ar ages of southern Indian kimberlites and a lamproite and their geochemical evolution. Precambrian Research, 189, 91-103.

Pandey, O. P., & Agrawal, P. K. (1999). Lithospheric Mantle Deformation beneath the Indian Cratons. The Journal of Geology, 107 (6), 683-692.

Patel, C. (2009). Identifying the asthenospheric component of kimberlite magmas from the Dharwar craton, India. Lithos, 112S, 296-310.

Patel, S. C., Ravi, S., Anilkumar, Y., Naik, A., Thakur, S. S., Pati, J. K., et al. (2009). Mafic xenoliths in Proterozoic kimberlites from Eastern Dharwar Craton, India: Mineralogy and P–T regime. Journal of Asian Earth Science, 34, 336-346.

Pittari, A., Cas, R. A., Lefebvre, N., Robey, J., Kurszlaukis, S., & K, W. (2008.). Eruption processes and facies architecture of the Orion Central kimberlite volcanic complex, Fort à la Corne, Saskatchewan: Kimberlite mass flow deposits in a sedimentary basin. Volcanol Geotherm Res, 174, 152-170.

Poller, U., Huth, J., Hopper, P., & Williams, I. S. (2001). REE, U, Th, and Hf distribution in zircon from western Carpathian Variscan Granitoids: A combined Cathodoluminiscence and Ion microprobe study. American Journal of Science, 301, 858-876.

Pradhan, V. R., Meert, J. G., Pandit, M. K., & Kamenov, G. (2010). India's changing place in global Proterozoic reconstructions: A review of geochronologic constraints and paleomagnetic poles from the Dharwar, Bundelkhand and Marwar cratons. Journal of Geodynamics, 50, 224-242.

Ram, B., Sing, N. P., & Murthy, A. S. (2007). A note on the qualitative appraisal of aeromagnetic image of Chhattisgarh basin. Journal of Indian Geophysics, 129-133.

Raval, U., & Veeraswamy, K. (2003). Modification of geological and geophysical regimes due to interaction of mantle plume with Indian lithosphere. Journal of the Virtual Explorer, 12, 117-143.

Ravi, S., Nayak, S. S., & Rao, K. S. (2012). Field guide to Southern Indian Kimberlites: guide for the 10th international kimberlite conference. Bangalore: Geological survey of India.

Reiners, P. W., K, H. J., & Brandon, M. T. (2005). U-Th zonation-dependent alpha ejection in (U-Th)/He chronometry. Geochimica et Cosmochimica Acta, 69 (13), 3349-3365.

Reiners, P. W., Spell, T. L., Nicolescu, S., & Zannetti, K. A. (2004). Zircon (U-Th)/He thermochronometry: He diffusion and comparison with 40Ar/39Ar dating. Geochimica et Cosmochimica Acta, 68 (8), 1857-1887.

Rogers, J. J., & Santosh, M. (2003). Supercontinents in Earth History. Gondwana Research, 357-368.

Rogers, R. W. (1986). The Dharwar Craton and the Assembly of Peninsular India. The Journal of Geology, 94 (2), 129-143.

Rogers, W. (1996). A History of Continents in the past three Billion Years. The Journal of Geology, 104 (1), 91-107.

Roy, S., & Rao, R. U. (2000). Heat flow in the Indian shield. Journal of Geophysical Research, 105 (B11), 22587-25604.

Saha, D., & Patranabis, S. (2013). Proterozoic evolution of the Eastern Dharwar and Bastar cratons, India- An overview of the intracratonic basins, craton margins and mobile belts. Journal of Asian Earth Sciences, http://dx.doi.org/10.1016/j.jseaes.2013.09.020.

Sahu, H. S., Raab, M. J., Kohn, B. P., Gleadow, A. J., & Kumar, D. (2013). Denudation history of Eastern Indian Peninsula from apatite fission track analysis: Linking possible plume-related uplift and the sedimentary record. Tectonophysics, 608, 1413-1428.

Sahu, N., Gupta, T., Patel, S. C., Khuntia, D. B., Behera, D., Pande, K., et al. (2013). Petrology of lamproites from the Nuapada Lamproite Field, Bastar Craton. In D. G. Pearson, H. S. Grütter, J. W. Harris, B. A. Kjarsgaard, H. O'Brien, N. V. Chalapathi Rao, et al. (Eds.), Proceedings od 10th International Kimberlite Conference: Volume 1 (p. 350). London: Journal of the Geological Society of India.

Sahu, N., Gupta, T., Patel, S. C., Khuntia, D. B., Pande, K., & Das, S. K. (2013). Petrology of Lamproites from the Naupada Lamproite Field, Bastar Craton, India. In D. G. Pearson, H. S. Grütter, J. W. Harris, B. A. Kjarsgaard, H. O'Brien, N. V. Chalapathi Rao, et al. (Eds.), Proceedings of 10th International Kimberlite Conference: Volume One (p. 350).

Scott Smith, B. H. (1987). Contrasting Kimberlites and Lamproites. Beijing.

Sharma, M., & Shukla, Y. (2012). Occurence of helically coiled microfossil Obruchevella in the Owk Shale of the Kurnool Group and its significance. Journal of Earth Systems, 121 (3), 755-768.

Smith, C. B. (1983). Pb, Sr, and Nd isotopic evidences for sources of southern African Cretaceous Kimberlites. Nature Geoscience, 304, 51-54.

Stanley, J. R., Flowers, R. M., & Bell, D. R. (2015). Erosion patterns and mantle sources of topographic change across the southern African Plateau derived from shallow and deep records of kimberlites. Geochemistry, Geoophysics, Geosystems, 16

(doi: 10.1002/2015GC005969).

Stanley, J. R., Flowers, R. M., & Bell, D. R. (2013). Kimberlite (U-Th)/He dating links surface erosion with lithospheric heating, thinning and metasomatism. Geology, 41, 1243-1246.

Sunder Raju, P. V., Eriksson, P. G., Catuneanu, O., Sarkar, S., & Banerjee, S. (2014). A review of the inferred geodynamic evolution of the Dharwar craton over the ca. 3.5–2.5 Ga period, and possible implications for global tectonics. Canadian Journal of Earth Sciences, 51, 312–325.

Swami, N. J., Ramakrishnan, M., & Viswanatha, M. N. (1976). Dharwar stratigraphic model and Karnataka cratonic evolution. Geological Survey of India, 107, 149-175.

Tappe, S., & Simonetti, A. (2012). Combined U-Pb geochronology and Sr-Nd isotope analysis of the ice river perovskite standard, implications for kimberlite and alkaline rock petrogenesis. *Chemical Geology , 304-305*, 10-17.

Tappe, S., Brand, N. B., Stracke, A., Van Acken, D., Liu, C. -Z., Strauss, H., Wu, F. –Y., Luguet, A., Mitchell, R.H. (2016). Plates or plumes in the origin of kimberlites: U/Pb perovskite and Sr-Nd-Hf-Os-C-O isotope constraints from the Superior craton (canada). *Chemical Geology , DOI: 10.1016/j.chemgeo.2016.08.019*.

Tappe, S., Foley, S. F., Stracke, A., Romer, R. L., Kjarsgaard, B. A., Heaman, L. M., Joyce, N. (2007). Craton reactivation on the Labrador sea margins: $^{40}Ar/^{39}Ar$ age and Sr-Nd-Hf-Pb isotope contrsaints from alkaline and carbonatite intrusives. Earth and Planetary Science Letters, 256, 433-454.

Tappe, S., Foley, S. F., Jenner, G. A., & Kjarsgaard, B. A. (2005). Integrating ultramafic lamprophyres into the IUGS classification of igneous rocks: Rational and Implications . *Journal of Petrology , 46*, 1893-1900.

Tappe, S., Kjarsgaard, B. A., Kurszlaukis, S., Nowell, G. M., & Phillips, D. (2014). Petrology and Nd-Hf Isotope Geochemistry of Neoproterozoic Amon Kimberlite Sills, Baffin Island (Canada): Evidence for Deep Mantle Magmatic Activity Linked to Supercontinent Cycles. Journal of Petrology, 55 (10), 2003-2014.

Tappe, S., Pearson, D. G., & Prevelic, D. (2013). Kimberlite, Carbonatite, and potassic magmatism as part of the geochemical cycle. Chemical Geology, 353, 1-3.

Tappe, S., Smart, K. A., Stracke, A., Romer, R. L., & van den Bogaard, T. (2016). Melt evolution beneath a rifted craton edge $^{40}Ar/^{39}Ar$ geochronology and Sr-Nd-Hf-Pb isotope systematics of primitive alkaline basalts and lamprophyres from the SW Baltic Shield. *Geochim Cosmochim Acta , 173*, 1-36.

Thompson, R. N., & Gibson, S. A. (1991). Subcontinental mantle plumes, hotspots and pre-existing thin spots. Journal of the Geological Society of London, 148, 973-977.

Tukker, H., Holder, A., Swarts, B., van Strijp, T., Grobler, E. (2016). The CCUT block cave design for Cullinan Diamond Mine. Journal of the Southern African Institute of Mining and Metallurgy, 6,8.

Wildman, M., Brown, R., Beucher, R., Persano, C., & Stuart, F. (2013). Resolving the chronology of the South African landscape through jointinverse modelling of AFT and apatite (U-Th)/He data. Geophysical Research Abstracts, 15, 1-2.

Williams, S. E., Landgrebe, T. C., & Whittaker, J. M. (2012). An open-source software environment for visualizing and refining plate tectonic reconstructions using high-resolution geological and geophysical data sets. GSA Today, 22 (4/5), doi: 10.1130/GSATG139A.1.

Winter, J. D. (2001). Principles of Igneous and Metamorphic Petrology. United States of America: Prentice Hall.

Wu, F. Y., Xu, Y. G., Zhu, R. X., & Zhang, G. W. (2014). Thinning and destruction of the cratonic lithosphere: A global perspective. Earth Sciences, 57 (12), 2878–2890.

Wyatt, B. A., Baumgartnerb, M., Anckarc, E., & Grutter, H. (2004). Compositional classification of ‘‘kimberlitic’’ and ‘‘non-kimberlitic’’ ilmenite. Lithos, 77, 819– 840.

Zahirovic, S., Muller, R. D., Seton, M., & Flament, N. (2015). Tectonic speed limits for plate kinematic reconstructions. Earth and Planetary Science Letters, 418, 40-52.

Zeitler, P., Herczeg, A., McDougall, I., & Honda, M. (1987). U-Th dating of apatite: A potential thermochronometer. Geochimica et Cosmochimica Acta, 51, 2865-2868.

Zonneveld, J. P., Kjarsgaard, B. A., Harvey, S. E., Heaman, L. M., McNeil, D. H., & Marcia, K. Y. (2004). Sedimentologic and stratigraphic constraints on the emplacement of the Star kimberlite east-central Saskatchewan. Lithos, 76, 115-138.

Appendix A- Petrographic Descriptions

Table A1. Petrographic descriptions of kimberlite samples and related rocks.

	Sample ID	Field	Rock Description
DHARWAR CRATON	CC-1	WKF	Coarse grained melanocratic rock consisting of megacryts, macrocrysts and microphenocrysts of olivine (serpentinized) in a groundmass of phlogopite, perovskite, opaques and apatite needles. Perovskite and rutile forms a necklace around olivine.
	CC-4	WKF	Greenish-black melanocratic rock comprising of megacryst and macrocryst of olivine and phlogopite and pelletal lapilli (including calcite or other minerals). Groundmass is made up of serpentine, calcite, diopside, phlogopite, perovskite and opaque minerals. Olivine is highly serpentinized.
	CC-5	WKF	Melano-mesocratic fine grained rock with macrocrysts of serpentinized olivine, calcite, phlogopite and opaque minerals forms part of the groundmass minerals. Also contains autolith, olivines in the autolith are fresh compared to other parts of the rock. Apatite occurs as radial (acicular) grains in the groundmass minerals.
	KL-3	WKF	Fine grained melanocratic rock comprising of megacrysts of olivine and ilmenite macrocrysts. Olivine is highly serpentinized and perovskite rims around its edges. The matrix consists of olivine, phlogopite and perovskite.
	KL-4	WKF	Coarse grained mesocratic rock comprising of two generations of olivines (megacryst and macrocrystst) of olivines, and phlogopite showing kink banding. Groundmass comprise of calcite, apatite and opaques. There are altered and unaltered olivine grains. Presence of carbonate rich pelletal lapilli.
	P-1	WKF	Fine grained dark-green rock made mostly of calcite, in a groundmass of phlogopite, serpentine with calcite-serpentine segregations textures. Pelletal lapilli and presence of garnet.
	P-2-N	WKF	Phlogopite rich rock with olivine macrocryst in a fine grained matrix of olivine, phlogopite and perovskite. Apatite occurs as needles in the groundmass.
	P-2-M	WKF	Highly serpentinized rock with euhedral altered olivines and perosvskite and carbonates forming the groundmass minerals.
	P-3	WKF	Greenish-black rock with olivine macrocryts and calcite pseudomorphed by serpentine, in a groudmass of olivine is (occasionally altered), phlogopite and opaques.
	P-4	WKF	Fine grained rock comprising of fresh olivines in a groundmass of olivine, serpentine and opaques minerals.
	P-5	WKF	Fine grained (macrocrytic) phlogopite rich rock with fresh olivine macrocrysts in a phlogopite rich groundmass.
	SK-1	RKF	Fine grained rock with serpentinized olivines, rock contains abundant opaque minerals and perovskite in the groundmass. Appatite occurs as needles.
	SK-2	RKF	Highly altered olivine grains in a serpentine and perovskite rich groundmass. Large apatite needles forms part of the groundmass.
	SK-3	RKF	Carbonate rich rock with calcite-serpentine segregations. Presence of opaque minerals and serpentinized olivine.
	EHJ 223		Black heavily carbonated rock with megacrysts of calcite-serpentine segregations, comprising of minor phlogopite with occasional serpentime and perovskite in the groundmass.

	EHJ 222		Grey rock made entirely of calcite and anhedral phlogopite grains pseudomorphed by calcite.
	KK	WKF	Fine grained rock composed of serpentinized olivine macrocrysts and elongated (subhedral) opaque minerals (Ilmenite). Apatite, calcite, perovskite and k-fledpsar forms part of the groundmass.
	KK-1	NKF	Fine grained melanocratic rock consisting of megacrytst and macrocrysts of sepenrtinized olivine. Calcite and phlogopite occur as in the groundmass minerals.
	KK-2	NKF	Fine grained melanocratic rock consisting of pyroxene macrocryst in a phlogopite, two generations of olivine (altered & unaltered) perovskite and opaque minerals in the groundmass.
	KK-6	NKF	Leucocratic coarse grained rock containing abundant opaque minerals and some megacryst of opaque mineral. .Olivine is highly serpentinized, clinopyroxene present in a serpentine and opaque rich groundmass (calcite rich).
	MK-1	NKF	Hard black rock with fresh olivine grains, groundmass is made up of microlithic diopside laths, opaque minerals and serpentine.
	MK-5	NKF	Grey rock with altered olivine grains (both macro and microphenocryst) serpentine. Olivine habit varies from rounded to ellipsoidal.
	NK-1	NKF	Dark-green rock with serpentinized olivines in a groundmass of serpentine, phlogopite and perovskite.
	NK-5	NKF	Dark rock with olivine macrocryts of olivine surrounded by phlogopite and serpentine, with the presence of phlogopite inclusions in olivine. Cpx and perovskite forms part of the groundmass minerals.
	PC-A	KLF	Black rock with lots of macrocrystal and microphenocrysts of mica (phlogopite), and minor feldspars and opaque minerals.
	PC-B	KLF	Fine grained greyish-black rock with the presence of feldspars and opaque minerals.
	R3	RLF	Greyish black rock with salt and pepper texture comprising mainly calcite.
	R8	RLF	Darkgreen rock with abundant opaque minerals. There is calcite present, phlogopite laths, feldspars and clinopyroxene..
	MH-EHJ814		Calcite-rich, reddish-brown rock with olivine macrocryst replaced by calcite. Groundmass contains subrounded to rounded perovskite grains with occasional serpentine-calcite segregations.
	MH-EHJ823		Bownish rock with rounded opaque macrocryts in a fine grained matrix. The groundmass is composed of skeletal texture of serpentine and clinopyroxene.
	MH-EHJ824		Calcite rich, greenish-brown rock with the presence of phlogopite, euhedral grains of calcite enclosed by serpentine and olivine is replacement by calcite. Rock fragments of sandtone/ quartz.are present.
	MH-EHJ825		Black- greyish rock with calcite segregatory texture. Calcite show occasional kink bands.
	MH-EHJ826		Greenish rock with a tint of red minerals, diopside microphenocrysts in a serpentine rich groundmass comprising of diopside.
BUNDELKHAND CRATON	BK-PK001/7		Medium to coarse grained rock. Diopside and orthopyroxene are present, contains minor opaque minerals and olivines are highly serpentinized.
	BK-PK001/8		Dark coloured rock mica minerals observed in thin section. Comprise of anhedral crystals of serpentinized clinopyroxene and orthopyroxene (amphibole)
	BK-PK001/9		Fine grained rock consisting of megacryts of clinopyroxene with minor phlogopite and feldspar minerals
	BK-PK001/2		Fine grained rock with a greenish appearance in thin section. Consists of anhedral macrocryts of carbonates and feldspar minerals. Serpentine is present and surrounds the rims of other minerals.
	BK-PK001/4		Fine grained rock with a greenish appearance consisting of anhedral alteration minerals. This rock composes mainly of altered minerals. No calcite encountered in this rock

BK-PK001/56	MKF	Yellowish green looking rock, medium to coarse grained, comprises of magmaclast, minor opaque minerals and the presence of K-feldspar with its diagnostic tartan texture. Quartz surrounds all the minerals
BK-PK002/10	MKF	Brown rock with serpentinized olivine macrocryst in a muddy (calcite) groundmass of subhedral olivine grains and opaque minerals.
BK-PK001/12	MKF	Sample was too soft to make a thin section.
BK-PK001/72		Soft green rock with an abundance of opaque minerals and serpentine-calcite segregations.
BK-EHY152		Yellowish green rock containing serpentinized olivines, two generations of phlogopite (macrocryst) and microphenocryts laths (in he groundmass) and couple opaque minerals in the groundmass
UDP	WFK	Black unaltered rock comprising of green core cpx with occasional mica and some opaque minerals.
CHL	CBL	Yellowish brown fine grained rock showing the presence of phlogopite, diopside and opaques. The groundmass is made up of calcite and opaque minerals, post-kinematic texture of phlogopite around the opaque minerals.
VD	KLF	Highly altered green rock with feldspar grains and perovskite forming a necklace around the grains
ALB		Grey rock comprising of altered olivine with abundant of phlogopite laths, occasional calcite and opaques.

Table A2. Rock types and classification of the Dharwar Craton samples

Sample	Rock Type	Facies	Sample	Rock Type	Facies
CC-1	Kimberlite	Hypabyssal	NK-5	Kimberlite	Hypabyssal
CC-4	Kimberlite	Hypabyssal	PC-A	Lamproite	-
CC-5	Kimberlite	Hypabyssal	PC-B	Lamproite	-
KL-3	Kimberlite	Hypabyssal	R3	Lamproite	-
KL-4	Kimberlite	Hypabyssal	R8	Lamproite	-
P-1	Kimberlite	Diatreme	MH-EHJ814	lamproites	-
P-2-N	Kimberlite	Hypabyssal	MH-EHJ823	-	-
P-2-M	Kimberlite	Hypabyssal	MH-EHJ824	-	-
P-3	Kimberlite	Hypabyssal	MH-EHJ825	-	-
P-4	Kimberlite	Hypabyssal	MH-EHJ826	-	-
P-5	Kimberlite	Hypabyssal	BK-PK001/7	-	-
SK-1	Kimberlite	Hypabyssal	BK-PK001/8	-	-
SK-2	Kimberlite	Hypabyssal	BK-PK001/9	-	-
SK-3	Kimberlite	Hypabyssal	BK-PK001/2	-	-
EHJ 223	Lamproite	-	BK-PK001/4	-	-
EHJ 222	Lamproite	-	BK-PK001/56	-	-
KK	Lamprophyre	Hypabyssal	BK-PK002/10	-	-
KK-1	Kimberlite	Hypabyssal	BK-PK001/12	-	Diatreme
KK-2	Kimberlite	Hypabyssal	BK-PK001/72	-	-
KK-6	Kimberlite	Hypabyssal	UDP	Lamprophyre	-
MK-1	Kimberlite	Hypabyssal	CHL	Lamproite	Hypabyssal
MK-5	Kimberlite	Hypabyssal	VD	Lamproite	-
NK-1	Kimberlite	Hypabyssal	ALB	Lamproite	-

- Indicates sample is not yet classified

Appendix B- Mineral compositions and plots.

Table B1: Perovskite compositions for EDC Kimberlites.

	CC-5 1	CC-5 2	CC-5 3	CC-5 4	CC-5 5	CC-5 6	CC-5 7	SK-1 1	SK-1 2	SK-1 3	SK-1 4	SK-1 5	SK-1 6	SK-1 7	SK-1 8
SiO_2	0.01	0.02	0.02	0.02	0.01	0.02	0.02	0.04	0.05	0.04	0.03	0.01	0.03	0.06	0.00
CaO	39.57	39.34	39.46	38.50	38.73	37.97	38.54	37.67	37.61	38.19	38.41	37.56	35.19	39.42	39.05
TiO_2	54.83	55.25	55.37	54.59	55.45	55.01	55.39	54.55	55.05	55.08	55.22	54.89	53.58	55.92	55.95
Al_2O3	0.32	0.32	0.26	0.29	0.32	0.30	0.31	0.26	0.26	0.26	0.29	0.26	0.28	0.32	0.23
MgO	0.05	0.04	0.07	0.07	0.05	0.04	0.05	0.14	0.03	0.04	0.08	0.07	0.06	0.04	0.07
FeO	0.60	0.98	0.54	0.01	0.81	0.44	0.21	1.04	1.02	1.20	0.87	1.08	0.83	0.94	1.00
La_2O_3	0.68	0.45	0.45	1.13	0.83	1.46	0.43	0.61	0.66	0.09	1.02	0.48	1.01	0.00	0.18
Nd_2O_3	1.04	1.22	1.27	0.00	1.13	1.41	0.01	0.97	1.44	1.24	0.54	1.26	1.26	0.11	0.63
MnO	0.00	0.06	0.03	0.02	0.00	0.00	0.00	0.01	0.02	0.00	0.01	0.00	0.00	0.00	0.01
Nb_2O_5	0.39	0.49	0.36	0.23	0.18	0.33	0.31	0.45	0.47	0.36	0.19	0.47	0.55	0.36	0.32
Na2O	0.31	0.30	0.30	0.38	0.49	0.42	0.35	0.39	0.54	0.40	0.36	0.46	0.69	0.24	0.27
SrO	0.89	0.79	0.83	0.94	0.82	0.77	0.87	0.70	0.71	0.79	0.86	0.82	0.85	0.80	0.83
Cr_2O_3	0.01	0.07	0.06	0.09	0.09	0.03	0.01	0.09	0.07	0.03	0.00	0.03	0.05	0.13	0.01
Ce_2O_3	1.25	1.11	1.24	1.43	1.64	1.74	1.24	1.19	1.89	1.40	1.00	1.76	2.73	0.44	0.83
Total	99.94	100.44	100.25	97.69	100.56	99.93	97.73	98.11	99.82	99.11	98.87	99.17	97.11	98.79	99.38
Si	0.000	0.000	0.001	0.000	0.000	0.001	0.000	0.001	0.001	0.001	0.001	0.000	0.001	0.001	0.000
Ca	0.986	0.974	0.978	0.977	0.961	0.950	0.972	0.954	0.942	0.958	0.964	0.946	0.911	0.979	0.970
Ti	0.959	0.961	0.963	0.972	0.966	0.966	0.980	0.970	0.968	0.970	0.973	0.970	0.973	0.975	0.976
Al	0.009	0.009	0.007	0.008	0.009	0.008	0.009	0.007	0.007	0.007	0.008	0.007	0.008	0.009	0.006
Mg	0.002	0.001	0.002	0.003	0.002	0.001	0.002	0.005	0.001	0.002	0.003	0.003	0.002	0.001	0.003
Fe	0.005	0.008	0.005	0.000	0.007	0.004	0.002	0.021	0.020	0.023	0.017	0.021	0.017	0.018	0.019
La	0.006	0.004	0.004	0.010	0.007	0.012	0.004	0.005	0.006	0.001	0.009	0.004	0.009	0.000	0.002
Nd	0.020	0.024	0.025	0.000	0.022	0.028	0.000	0.008	0.012	0.010	0.005	0.011	0.011	0.001	0.005
Mn	0.000	0.001	0.001	0.000	0.000	0.000	0.000	0.000	0.000	0.000	0.000	0.000	0.000	0.000	0.000

Nb	0.004	0.005	0.004	0.003	0.002	0.004	0.003	0.005	0.005	0.004	0.002	0.005	0.006	0.004	0.003
Na	0.014	0.013	0.013	0.017	0.022	0.019	0.016	0.018	0.025	0.018	0.016	0.021	0.032	0.011	0.012
Sr	0.012	0.011	0.011	0.013	0.011	0.011	0.012	0.010	0.010	0.011	0.012	0.011	0.012	0.011	0.011
Cr	0.000	0.001	0.001	0.002	0.002	0.001	0.000	0.002	0.001	0.001	0.000	0.001	0.001	0.002	0.000
Ce	0.011	0.009	0.011	0.012	0.014	0.015	0.011	0.010	0.016	0.012	0.009	0.015	0.024	0.004	0.007
Total	2.03	2.02	2.02	2.02	2.02	2.02	2.01	2.02	2.01	2.02	2.02	2.01	2.01	2.02	2.02

Table B2**:** Olivine compositions for kimberlite CC-5, Mg-number is defined as 100MgO/(MgO + FeO)) in mole per cent.

	CC-5 1	CC-5 2	CC-5 3	CC-5 4	CC-5 5	CC-5 6	CC-5 7	CC-5 8	CC-5 9	CC-5 10	CC-5 11	CC-5 12	CC-5 13	CC-5 14	CC-5 15	CC-5 16	CC-5 17
SiO_2	41.09	40.70	40.52	40.83	40.85	40.84	40.05	40.03	41.45	40.75	41.19	41.22	39.93	40.00	39.76	41.14	40.07
CaO	0.07	0.06	0.09	0.09	0.06	0.11	0.08	0.10	0.02	0.00	0.02	0.04	0.09	0.10	0.07	0.06	0.09
Al_2O_3	0.08	0.02	0.01	0.03	0.02	0.04	0.01	0.01	0.02	0.02	0.01	0.02	0.02	0.01	0.03	0.02	0.01
MgO	50.88	50.80	50.86	51.17	51.05	50.27	47.11	47.31	52.84	52.21	52.71	50.45	47.85	47.68	45.89	51.02	47.26
FeO	7.76	7.52	7.77	7.05	7.86	8.29	11.97	12.16	5.74	5.92	5.89	8.27	11.87	11.36	13.87	7.49	11.95
MnO	0.04	0.03	0.04	0.04	0.06	0.06	0.07	0.07	0.06	0.02	0.02	0.03	0.06	0.07	0.09	0.06	0.08
NiO	0.09	0.14	0.12	0.10	0.08	0.04	0.01	0.05	0.08	0.05	0.05	0.12	0.23	0.23	0.07	0.11	0.05
Cr_2O_3	0.09	0.03	0.09	0.02	0.07	0.06	0.00	0.05	0.10	0.11	0.01	0.09	0.11	0.03	0.05	0.13	0.03
TiO_2	0.02	0.00	0.01	0.00	0.00	0.01	0.03	0.00	0.00	0.00	0.00	0.00	0.04	0.01	0.02	0.00	0.00
Total	100.11	99.30	99.49	99.31	100.04	99.73	99.33	99.77	100.30	99.08	99.90	100.24	100.18	99.49	99.85	100.03	99.54
							Normalized to 3 Cations										
Si	0.996	0.995	0.990	0.995	0.992	0.997	0.998	0.994	0.994	0.991	0.993	1.000	0.988	0.994	0.995	0.997	0.997
Ca	0.002	0.002	0.002	0.002	0.002	0.003	0.002	0.003	0.000	0.000	0.000	0.001	0.002	0.003	0.002	0.002	0.002
Al	0.002	0.001	0.000	0.001	0.001	0.001	0.000	0.000	0.001	0.001	0.000	0.001	0.001	0.000	0.001	0.000	0.000
Mg	1.839	1.851	1.853	1.859	1.849	1.829	1.750	1.752	1.890	1.893	1.894	1.825	1.765	1.766	1.712	1.844	1.752
Fe^{2+}	0.158	0.154	0.159	0.144	0.160	0.169	0.249	0.253	0.115	0.120	0.119	0.168	0.246	0.236	0.290	0.152	0.249
Mn	0.001	0.001	0.001	0.001	0.001	0.001	0.001	0.002	0.001	0.000	0.000	0.001	0.001	0.001	0.002	0.001	0.002
Ni	0.002	0.003	0.002	0.002	0.002	0.001	0.000	0.001	0.002	0.001	0.001	0.002	0.005	0.005	0.002	0.002	0.001
Cr	0.002	0.001	0.002	0.000	0.001	0.001	0.000	0.001	0.002	0.002	0.000	0.002	0.002	0.001	0.001	0.002	0.001

Ti	0.000	0.000	0.000	0.000	0.000	0.000	0.001	0.000	0.000	0.000	0.000	0.000	0.001	0.000	0.000	0.000	0.000
Total	3.002	3.005	3.009	3.004	3.007	3.002	3.002	3.005	3.004	3.008	3.007	2.999	3.010	3.006	3.004	3.001	3.003
Mg#	0.92	0.92	0.92	0.93	0.92	0.92	0.88	0.87	0.94	0.94	0.94	0.92	0.88	0.88	0.86	0.92	0.88

Table B3. Serpentine compositions for kimberlite SK-1 and SK-2.

	SK-1 52	SK-1 54	SK-1 55	SK-1 56	SK-1 57	SK-1 58	SK-1 60	SK-1 59	SK-1 64	SK-1 63	SK-2 113	SK-2 114	SK-2 115	SK-2 123	SK-2 124	SK-2 125
SiO_2	40.78	40.35	40.22	39.98	40.13	39.45	38.33	38.44	40.45	40.86	37.10	38.52	37.60	38.87	39.26	38.22
CaO	0.09	0.06	0.04	0.03	0.05	0.06	0.06	0.09	0.07	0.07	0.10	0.08	0.07	0.07	0.08	0.06
Al_2O_3	0.97	1.37	1.74	1.79	1.55	3.44	1.51	1.87	1.30	0.90	1.62	1.34	1.60	0.93	0.95	1.06
MgO	38.90	37.35	37.53	37.45	36.75	36.55	36.79	35.58	38.37	38.89	33.63	34.72	34.68	35.94	35.22	34.90
FeO	2.56	6.79	6.65	6.42	6.71	5.15	7.48	7.45	2.60	2.68	10.72	9.83	10.91	9.91	9.61	10.44
MnO	0.02	0.04	0.03	0.03	0.05	0.03	0.04	0.05	0.02	0.03	0.00	0.00	0.00	0.01	0.00	0.00
NiO	0.05	0.00	0.00	0.00	0.00	0.03	0.01	0.02	0.02	0.02	0.00	0.00	0.00	0.00	0.00	0.00
Cr_2O_3	0.09	0.01	0.03	0.03	0.02	0.00	0.01	0.01	0.06	0.00	0.45	0.48	0.40	0.11	0.10	0.15
TiO_2	0.06	0.03	0.04	0.03	0.04	0.11	0.03	0.03	0.07	0.08	0.09	0.06	0.08	0.06	0.06	0.06
Total	83.51	85.98	86.28	85.75	85.30	84.82	84.25	83.53	82.96	83.52	83.72	85.04	85.35	85.90	85.27	84.89

Table B4: Ilmenite compositions for the kimberlite CC-5 and SK-1. FeO* - the total iron content.

	CC-5 1	CC-5 2	CC-5 3	CC-5 4	CC-5 5	CC-5 6	CC-5 7	SK-1 1	SK-1 2	SK-1 3	SK-1 4	SK-1 5	SK-1 6	SK-1 7	SK-1 8
SiO_2	0.01	0.02	0.02	0.02	0.01	0.02	0.02	0.04	0.05	0.04	0.03	0.01	0.03	0.06	0.00
CaO	39.57	39.34	39.46	38.50	38.73	37.97	38.54	37.67	37.61	38.19	38.41	37.56	35.19	39.42	39.05
TiO_2	54.83	55.25	55.37	54.59	55.45	55.01	55.39	54.55	55.05	55.08	55.22	54.89	53.58	55.92	55.95
Al_2O3	0.32	0.32	0.26	0.29	0.32	0.30	0.31	0.26	0.26	0.26	0.29	0.26	0.28	0.32	0.23
MgO	0.05	0.04	0.07	0.07	0.05	0.04	0.05	0.14	0.03	0.04	0.08	0.07	0.06	0.04	0.07
FeO	0.60	0.98	0.54	0.01	0.81	0.44	0.21	1.04	1.02	1.20	0.87	1.08	0.83	0.94	1.00
La_2O_3	0.68	0.45	0.45	1.13	0.83	1.46	0.43	0.61	0.66	0.09	1.02	0.48	1.01	0.00	0.18
Nd_2O_3	1.04	1.22	1.27	0.00	1.13	1.41	0.01	0.97	1.44	1.24	0.54	1.26	1.26	0.11	0.63
MnO	0.00	0.06	0.03	0.02	0.00	0.00	0.00	0.01	0.02	0.00	0.01	0.00	0.00	0.00	0.01
Nb_2O_5	0.39	0.49	0.36	0.23	0.18	0.33	0.31	0.45	0.47	0.36	0.19	0.47	0.55	0.36	0.32
Na2O	0.31	0.30	0.30	0.38	0.49	0.42	0.35	0.39	0.54	0.40	0.36	0.46	0.69	0.24	0.27
SrO	0.89	0.79	0.83	0.94	0.82	0.77	0.87	0.70	0.71	0.79	0.86	0.82	0.85	0.80	0.83
Cr_2O_3	0.01	0.07	0.06	0.09	0.09	0.03	0.01	0.09	0.07	0.03	0.00	0.03	0.05	0.13	0.01
Ce_2O_3	1.25	1.11	1.24	1.43	1.64	1.74	1.24	1.19	1.89	1.40	1.00	1.76	2.73	0.44	0.83
Total	99.94	100.44	100.25	97.69	100.56	99.93	97.73	98.11	99.82	99.11	98.87	99.17	97.11	98.79	99.38
Si	0.000	0.000	0.001	0.000	0.000	0.001	0.000	0.001	0.001	0.001	0.001	0.000	0.001	0.001	0.000
Ca	0.986	0.974	0.978	0.977	0.961	0.950	0.972	0.954	0.942	0.958	0.964	0.946	0.911	0.979	0.970
Ti	0.959	0.961	0.963	0.972	0.966	0.966	0.980	0.970	0.968	0.970	0.973	0.970	0.973	0.975	0.976
Al	0.009	0.009	0.007	0.008	0.009	0.008	0.009	0.007	0.007	0.007	0.008	0.007	0.008	0.009	0.006
Mg	0.002	0.001	0.002	0.003	0.002	0.001	0.002	0.005	0.001	0.002	0.003	0.003	0.002	0.001	0.003
Fe	0.005	0.008	0.005	0.000	0.007	0.004	0.002	0.021	0.020	0.023	0.017	0.021	0.017	0.018	0.019
La	0.006	0.004	0.004	0.010	0.007	0.012	0.004	0.005	0.006	0.001	0.009	0.004	0.009	0.000	0.002
Nd	0.020	0.024	0.025	0.000	0.022	0.028	0.000	0.008	0.012	0.010	0.005	0.011	0.011	0.001	0.005
Mn	0.000	0.001	0.001	0.000	0.000	0.000	0.000	0.000	0.000	0.000	0.000	0.000	0.000	0.000	0.000

Nb	0.004	0.005	0.004	0.003	0.002	0.004	0.003	0.005	0.005	0.004	0.002	0.005	0.006	0.004	0.003
Na	0.014	0.013	0.013	0.017	0.022	0.019	0.016	0.018	0.025	0.018	0.016	0.021	0.032	0.011	0.012
Sr	0.012	0.011	0.011	0.013	0.011	0.011	0.012	0.010	0.010	0.011	0.012	0.011	0.012	0.011	0.011
Cr	0.000	0.001	0.001	0.002	0.002	0.001	0.000	0.002	0.001	0.001	0.000	0.001	0.001	0.002	0.000
Ce	0.011	0.009	0.011	0.012	0.014	0.015	0.011	0.010	0.016	0.012	0.009	0.015	0.024	0.004	0.007
Total	2.03	2.02	2.02	2.02	2.02	2.02	2.01	2.02	2.01	2.02	2.02	2.01	2.01	2.02	2.02

Table B5: Ilmenite compositions for kimberlite SK-2. FeO* - the total iron content.

	SK-2 78	SK-2 79	SK-2 80	SK-2 81	SK-2 84	SK-2 101	SK-2 107	SK-2 108	SK-2 116	SK-2 117	SK-2 118	SK-2 119
SiO_2	0.58	1.91	0.07	0.09	0.27	0.19	0.08	0.06	0.09	0.17	0.21	0.76
TiO_2	52.51	44.45	53.96	53.82	51.35	54.41	53.69	53.43	53.01	53.24	53.88	53.03
Al_2O_3	0.3	0.36	0.28	0.27	0.37	0.33	0.52	0.53	0.24	0.26	0.37	0.42
Cr_2O_3	0.00	0.00	0.00	0.00	0.00	0.00	0.00	0.00	0.00	0.00	0.00	0.00
V_2O_3	0.00	0.00	0.00	0.00	0.00	0.00	0.00	0.00	0.00	0.00	0.00	0.00
Fe_2O_3	9.49	17.28	6.70	6.88	6.95	6.17	8.05	8.16	7.53	7.06	7.40	8.28
FeO	20.35	16.31	22.90	22.38	26.73	21.89	19.81	19.74	22.15	22.61	20.91	20.17
FeO*	28.89	31.86	28.93	28.57	32.98	27.45	27.06	27.08	28.92	28.96	27.57	27.62
MnO	0.31	1.68	0.3	0.27	1.31	0.44	0.48	0.41	0.34	0.31	0.43	0.40
MgO	14.45	10.13	13.88	14.12	9.86	14.63	15.37	15.33	13.90	13.81	15.08	15.23
CaO	1.08	4.75	0.43	0.47	0.63	0.50	0.50	0.47	0.30	0.33	0.30	0.61
NiO	0.1	0.08	0.1	0.08	0.07	0.09	0.04	0.05	0.11	0.10	0.07	0.10
ZnO	0.02	0.03	0.02	0.01	0	0.02	0.01	0.00	0.03	0.03	0.04	0.00
Total	99.19	96.98	98.64	98.39	97.54	98.68	98.56	98.18	97.69	97.92	98.69	99.00
					Normalized to two cations							
Si	0.013	0.045	0.002	0.002	0.006	0.004	0.002	0.001	0.002	0.004	0.005	0.017
Ti	0.901	0.795	0.936	0.935	0.926	0.938	0.922	0.921	0.929	0.931	0.927	0.906
Al	0.008	0.010	0.008	0.007	0.010	0.009	0.014	0.014	0.007	0.007	0.010	0.011
Cr	0.000	0.000	0.000	0.000	0.000	0.000	0.000	0.000	0.000	0.000	0.000	0.000
V^{3+}	0.000	0.000	0.000	0.000	0.000	0.000	0.000	0.000	0.000	0.000	0.000	0.000
Fe^{3+}	0.163	0.309	0.116	0.119	0.125	0.107	0.138	0.141	0.132	0.123	0.127	0.142
Fe^{2+}	0.388	0.324	0.442	0.432	0.536	0.420	0.378	0.378	0.431	0.440	0.400	0.383
Mn	0.006	0.034	0.006	0.005	0.027	0.009	0.009	0.008	0.007	0.006	0.008	0.008
Mg	0.491	0.359	0.477	0.486	0.352	0.500	0.523	0.524	0.483	0.478	0.514	0.516
Ca	0.026	0.121	0.011	0.012	0.016	0.012	0.012	0.012	0.007	0.008	0.007	0.015
Ni	0.002	0.002	0.002	0.001	0.001	0.002	0.001	0.001	0.002	0.002	0.001	0.002
Zn	0.000	0.001	0.000	0.000	0.000	0.000	0.000	0.000	0.001	0.001	0.001	0.000
Total	2.000	2.000	2.000	2.000	2.000	2.000	2.000	2.000	2.000	2.000	2.000	2.000
					End Members							
$FeSiO_3$	1.34	4.84	0.16	0.21	0.65	0.44	0.18	0.14	0.21	0.40	0.48	1.74
$FeTiO_3$	40.95	42.82	45.60	44.63	55.17	43.26	39.22	39.19	44.14	44.84	40.59	38.60
Al_2O_3	0.41	0.54	0.38	0.37	0.53	0.45	0.70	0.72	0.33	0.36	0.50	0.57
Cr_2O_3	0.00	0.00	0.00	0.00	0.00	0.00	0.00	0.00	0.00	0.00	0.00	0.00
Fe_2O_3	6.81	9.91	5.20	5.34	5.44	4.64	6.30	6.46	6.12	5.67	5.93	6.29
$MnTiO_3$	0.61	3.60	0.59	0.53	2.68	0.86	0.93	0.80	0.67	0.61	0.84	0.78
$MgTiO_3$	49.84	38.23	48.02	48.90	35.53	50.32	52.64	52.70	48.47	48.07	51.59	52.02
ZnTiO3	0.03	0.06	0.03	0.02	0.00	0.03	0.02	0.00	0.05	0.05	0.07	0.00

V_2O_3	0.00	0.00	0.00	0.00	0.00	0.00	0.00	0.00	0.00	0.00	0.00	0.00
Total	100.00	100.00	100.00	100.00	100.00	100.00	100.00	100.00	100.00	100.00	100.00	100.00

Table B5: Ilmenite compositions for kimberlite SK-2 continued, FeO* - the total iron content.

	SK-2 78	SK-2 79	SK-2 80	SK-2 81	SK-2 84	SK-2 101	SK-2 107	SK-2 108	SK-2 116	SK-2 117	SK-2 118	SK-2 119	SK-2 120
SiO_2	0.58	1.91	0.07	0.09	0.27	0.19	0.08	0.06	0.09	0.17	0.21	0.76	0.07
TiO_2	52.51	44.45	53.96	53.82	51.35	54.41	53.69	53.43	53.01	53.24	53.88	53.03	53.44
Al_2O_3	0.3	0.36	0.28	0.27	0.37	0.33	0.52	0.53	0.24	0.26	0.37	0.42	0.40
Cr_2O_3	0.00	0.00	0.00	0.00	0.00	0.00	0.00	0.00	0.00	0.00	0.00	0.00	0.00
V_2O_3	0.00	0.00	0.00	0.00	0.00	0.00	0.00	0.00	0.00	0.00	0.00	0.00	0.00
Fe_2O_3	9.49	17.28	6.70	6.88	6.95	6.17	8.05	8.16	7.53	7.06	7.40	8.28	7.69
FeO	20.35	16.31	22.90	22.38	26.73	21.89	19.81	19.74	22.15	22.61	20.91	20.17	20.98
FeO*	28.89	31.86	28.93	28.57	32.98	27.45	27.06	27.08	28.92	28.96	27.57	27.62	27.90
MnO	0.31	1.68	0.3	0.27	1.31	0.44	0.48	0.41	0.34	0.31	0.43	0.40	0.40
MgO	14.45	10.13	13.88	14.12	9.86	14.63	15.37	15.33	13.90	13.81	15.08	15.23	14.78
CaO	1.08	4.75	0.43	0.47	0.63	0.50	0.50	0.47	0.30	0.33	0.30	0.61	0.26
NiO	0.1	0.08	0.1	0.08	0.07	0.09	0.04	0.05	0.11	0.10	0.07	0.10	0.07
ZnO	0.02	0.03	0.02	0.01	0	0.02	0.01	0.00	0.03	0.03	0.04	0.00	0.02
Total	99.19	96.98	98.64	98.39	97.54	98.68	98.56	98.18	97.69	97.92	98.69	99.00	98.11
					Normalized to two cations								
Si	0.013	0.045	0.002	0.002	0.006	0.004	0.002	0.001	0.002	0.004	0.005	0.017	0.002
Ti	0.901	0.795	0.936	0.935	0.926	0.938	0.922	0.921	0.929	0.931	0.927	0.906	0.926
Al	0.008	0.010	0.008	0.007	0.010	0.009	0.014	0.014	0.007	0.007	0.010	0.011	0.011
Cr	0.000	0.000	0.000	0.000	0.000	0.000	0.000	0.000	0.000	0.000	0.000	0.000	0.000
V^{3+}	0.000	0.000	0.000	0.000	0.000	0.000	0.000	0.000	0.000	0.000	0.000	0.000	0.000
Fe^{3+}	0.163	0.309	0.116	0.119	0.125	0.107	0.138	0.141	0.132	0.123	0.127	0.142	0.133
Fe^{2+}	0.388	0.324	0.442	0.432	0.536	0.420	0.378	0.378	0.431	0.440	0.400	0.383	0.404
Mn	0.006	0.034	0.006	0.005	0.027	0.009	0.009	0.008	0.007	0.006	0.008	0.008	0.008
Mg	0.491	0.359	0.477	0.486	0.352	0.500	0.523	0.524	0.483	0.478	0.514	0.516	0.508
Ca	0.026	0.121	0.011	0.012	0.016	0.012	0.012	0.012	0.007	0.008	0.007	0.015	0.006
Ni	0.002	0.002	0.002	0.001	0.001	0.002	0.001	0.001	0.002	0.002	0.001	0.002	0.001
Zn	0.000	0.001	0.000	0.000	0.000	0.000	0.000	0.000	0.001	0.001	0.001	0.000	0.000
Total	2.000	2.000	2.000	2.000	2.000	2.000	2.000	2.000	2.000	2.000	2.000	2.000	2.000
					End Members								
$FeSiO_3$	1.34	4.84	0.16	0.21	0.65	0.44	0.18	0.14	0.21	0.40	0.48	1.74	0.16
$FeTiO_3$	40.95	42.82	45.60	44.63	55.17	43.26	39.22	39.19	44.14	44.84	40.59	38.60	41.23
Al_2O_3	0.41	0.54	0.38	0.37	0.53	0.45	0.70	0.72	0.33	0.36	0.50	0.57	0.55
Cr_2O_3	0.00	0.00	0.00	0.00	0.00	0.00	0.00	0.00	0.00	0.00	0.00	0.00	0.00
Fe_2O_3	6.81	9.91	5.20	5.34	5.44	4.64	6.30	6.46	6.12	5.67	5.93	6.29	6.29
$MnTiO_3$	0.61	3.60	0.59	0.53	2.68	0.86	0.93	0.80	0.67	0.61	0.84	0.78	0.78

$MgTiO_3$	49.84	38.23	48.02	48.90	35.53	50.32	52.64	52.70	48.47	48.07	51.59	52.02	50.95
ZnTiO3	0.03	0.06	0.03	0.02	0.00	0.03	0.02	0.00	0.05	0.05	0.07	0.00	0.03
V_2O_3	0.00	0.00	0.00	0.00	0.00	0.00	0.00	0.00	0.00	0.00	0.00	0.00	0.00
Total	100.00	100.00	100.00	100.00	100.00	100.00	100.00	100.00	100.00	100.00	100.00	100.00	100.00

Table B5: Ilmenite compositions for kimberlite SK-2 continued, FeO* - the total iron content.

	SK-2 129	SK-2 130	SK-2 131	SK-2 133	SK-2 134	SK-2 135	SK-2 136	SK-2 137	SK-2 138	SK-2 139	SK-2 140	SK-2 142	SK-2 143
SiO_2	0.25	0.05	0.10	0.04	0.08	1.74	0.09	0.09	0.10	0.13	0.07	0.23	0.06
TiO_2	53.05	50.37	51.00	53.95	54.10	52.05	53.91	54.20	51.18	51.58	50.74	50.13	51.42
Al_2O_3	0.39	0.02	0.02	0.36	0.36	0.41	0.39	0.41	0.36	0.31	0.01	0.01	0.02
Cr_2O_3	0.00	0.00	0.00	0.00	0.00	0.00	0.00	0.00	0.00	0.00	0.00	0.00	0.00
V_2O_3	0.00	0.00	0.00	0.00	0.00	0.00	0.00	0.00	0.00	0.00	0.00	0.00	0.00
Fe_2O_3	6.65	3.48	2.20	6.18	6.43	5.32	3.82	4.44	6.37	4.02	1.29	1.49	1.44
FeO	23.28	35.07	35.49	23.30	23.42	23.49	25.31	24.79	27.87	30.32	35.62	35.34	35.95
FeO*	29.26	38.20	37.47	28.86	29.20	28.27	28.74	28.78	33.60	33.94	36.78	36.68	37.25
MnO	0.34	8.62	8.80	0.35	0.33	0.32	0.31	0.24	1.97	1.99	9.13	8.93	9.4
MgO	12.29	0.17	0.22	13.45	13.49	13.02	12.23	12.79	7.79	6.90	0.1	0.15	0.14
CaO	1.77	0.96	0.91	0.66	0.67	1.36	0.81	0.68	1.79	1.39	0.5	0.55	0.46
NiO	0.13	0.02	0.00	0.10	0.10	0.12	0.13	0.15	0.11	0.12	0.03	0.00	0.00
ZnO	0.10	0.00	0.02	0.00	0.00	0.02	0.01	0.01	0.00	0.01	0.00	0.00	0.00
Total	98.25	98.76	98.76	98.39	98.97	97.84	97.00	97.79	97.54	96.77	97.49	96.83	98.89
						End Members							
Si	0.006	0.001	0.003	0.001	0.002	0.040	0.002	0.002	0.002	0.003	0.002	0.006	0.002
Ti	0.930	0.965	0.976	0.940	0.938	0.908	0.958	0.953	0.934	0.955	0.985	0.979	0.984
Al	0.011	0.001	0.001	0.010	0.010	0.011	0.011	0.011	0.010	0.009	0.000	0.000	0.001
Cr	0.000	0.000	0.000	0.000	0.000	0.000	0.000	0.000	0.000	0.000	0.000	0.000	0.000
V^{3+}	0.000	0.000	0.000	0.000	0.000	0.000	0.000	0.000	0.000	0.000	0.000	0.000	0.000
Fe^{3+}	0.117	0.067	0.042	0.108	0.111	0.093	0.068	0.078	0.116	0.074	0.025	0.029	0.028
Fe^{2+}	0.454	0.747	0.755	0.452	0.451	0.455	0.500	0.485	0.566	0.624	0.769	0.768	0.765
Mn	0.007	0.186	0.190	0.007	0.006	0.006	0.006	0.005	0.041	0.042	0.200	0.196	0.203
Mg	0.427	0.006	0.008	0.465	0.463	0.450	0.431	0.446	0.282	0.253	0.004	0.006	0.005
Ca	0.044	0.026	0.025	0.016	0.017	0.034	0.021	0.017	0.047	0.037	0.014	0.015	0.013
Ni	0.002	0.000	0.000	0.002	0.002	0.002	0.002	0.003	0.002	0.002	0.001	0.000	0.000
Zn	0.002	0.000	0.000	0.000	0.000	0.000	0.000	0.000	0.000	0.000	0.000	0.000	0.000
Total	2.000	2.000	2.000	2.000	2.000	2.000	2.000	2.000	2.000	2.000	2.000	2.000	2.000
						End members							
$FeSiO_3$	0.60	0.13	0.26	0.09	0.19	4.11	0.22	0.21	0.25	0.33	0.18	0.60	0.15
$FeTiO_3$	50.80	78.30	78.77	47.32	47.22	45.97	52.74	50.77	62.72	67.35	78.76	78.30	78.13
Al_2O_3	0.55	0.03	0.03	0.50	0.49	0.57	0.55	0.57	0.53	0.46	0.02	0.02	0.03
Cr_2O_3	0.00	0.00	0.00	0.00	0.00	0.00	0.00	0.00	0.00	0.00	0.00	0.00	0.00

Fe_2O_3	3.49	2.03	0.86	4.52	4.70	2.87	2.26	2.93	3.47	1.80	0.54	0.70	0.76
$MnTiO_3$	0.69	18.85	19.20	0.69	0.65	0.64	0.63	0.48	4.15	4.23	20.12	19.80	20.40
$MgTiO_3$	43.70	0.65	0.84	46.88	46.76	45.81	43.59	45.02	28.88	25.82	0.39	0.59	0.53
ZnTiO3	0.18	0.00	0.04	0.00	0.00	0.03	0.02	0.02	0.00	0.02	0.00	0.00	0.00
V_2O_3	0.00	0.00	0.00	0.00	0.00	0.00	0.00	0.00	0.00	0.00	0.00	0.00	0.00
Total	100.00	100.00	100.00	100.00	100.00	100.00	100.00	100.00	100.00	100.00	100.00	100.00	100.00

Table B6. Spinel compositions for samples SK-1.

	SK-1 1-a	SK-1 3-a	SK-1 4-a	SK-1 5-a	SK-1 6-a	SK-1 7-a	SK-1 8-a	SK-1 9-a	SK-1 10-a	SK-1 11-a	SK-1 12-a	SK-1 13-a	SK-1 14-a	SK-1 15-a	SK-1 16-a	SK-1 17-a	SK-1 22-a	SK-1 23-a
SiO_2	0.15	0.11	0.12	0.12	0.11	0.09	0.09	0.21	0.09	0.18	0.18	0.11	0.14	0.09	0.11	0.08	0.1	0.09
TiO_2	5.58	13.81	13.96	13.55	17.21	16.75	14.92	13.72	14.15	6.04	5.96	14.77	13.71	15.98	16.13	15	15.86	15.82
Al_2O_3	11.08	6.43	5.88	5.39	6.13	6.52	7.86	8.48	7.59	11.66	11.73	6.24	7.38	7.37	7.5	7.6	7.49	7.13
$Cr2O_3$	43.21	4.52	6.13	3.33	3.84	1.83	0.18	0.1	0.18	42.36	42.43	1.99	0.98	0.18	0.13	0.27	0.11	0.39
V_2O_3	0.23	0.03	0.07	0.05	0.05	0.05	0.04	0.05	0.06	0.26	0.23	0.04	0.09	0.06	0.04	0.05	0.05	0.04
Fe_2O_3	8.25	29.29	28.61	32.12	32.58	34.28	34.74	35.04	33.89	7.28	7.44	30.00	32.12	36.10	35.19	31.59	34.05	33.33
FeO	17.01	40.17	37.51	37.32	23.16	22.12	26.97	27.87	31.17	17.57	17.76	38.96	36.93	22.82	22.72	33.06	24.77	27.02
MnO	0.38	1.5	1.86	1.57	0.7	0.54	0.57	0.64	0.85	0.37	0.34	1.8	1.48	0.5	0.47	1.1	0.46	0.61
MgO	13.98	1.39	3.12	2.96	15.64	15.85	11.49	10.17	7.88	13.93	13.81	2.57	3.47	15.07	15.09	6.98	13.32	11.65
CaO	0.07	0.15	0.1	0.1	0.17	0.19	0.2	0.22	0.2	0.08	0.11	0.19	0.24	0.22	0.24	0.16	0.32	0.35
ZnO	0.05	0.69	0.3	0.22	0.08	0.1	0.05	0.08	0.05	0.06	0.08	0.09	0.27	0.04	0.08	0.08	0.06	0.05
Total	99.99	98.09	97.66	96.74	99.67	98.31	97.11	96.58	96.11	99.79	100.07	96.76	96.81	98.44	97.70	95.97	96.59	96.48
								Calculated to 24 cations										
Si	0.039	0.032	0.035	0.036	0.029	0.024	0.025	0.058	0.026	0.046	0.046	0.033	0.041	0.024	0.029	0.023	0.027	0.025
Ti	1.078	3.066	3.077	3.030	3.399	3.341	3.085	2.869	3.035	1.166	1.148	3.293	3.021	3.191	3.239	3.240	3.255	3.294
Al	3.353	2.237	2.031	1.888	1.897	2.038	2.546	2.779	2.551	3.526	3.540	2.180	2.548	2.306	2.359	2.573	2.409	2.326
Cr	8.773	1.055	1.420	0.783	0.797	0.384	0.039	0.022	0.041	8.592	8.591	0.466	0.227	0.038	0.027	0.061	0.024	0.085
V	0.047	0.007	0.016	0.012	0.011	0.011	0.009	0.011	0.014	0.053	0.047	0.010	0.021	0.013	0.009	0.012	0.011	0.009
Fe(iii)	1.594	6.506	6.308	7.186	6.439	6.839	7.186	7.332	7.273	1.405	1.434	6.692	7.080	7.213	7.069	6.828	6.992	6.942
Fe(ii)	3.653	9.914	9.191	9.278	5.086	4.904	6.199	6.479	7.434	3.770	3.802	9.658	9.045	5.067	5.072	7.941	5.652	6.254
Mn	0.083	0.375	0.462	0.395	0.156	0.121	0.133	0.151	0.205	0.080	0.074	0.452	0.367	0.112	0.106	0.268	0.106	0.143
Mg	5.352	0.612	1.363	1.312	6.123	6.266	4.709	4.216	3.350	5.328	5.273	1.136	1.515	5.965	6.005	2.989	5.419	4.808
Ca	0.019	0.047	0.031	0.032	0.048	0.054	0.059	0.066	0.061	0.022	0.030	0.060	0.075	0.063	0.069	0.049	0.094	0.104
Zn	0.009	0.150	0.065	0.048	0.016	0.020	0.010	0.016	0.011	0.011	0.015	0.020	0.058	0.008	0.016	0.017	0.012	0.010
Total	24.000	24.000	24.000	24.000	24.000	24.000	24.000	24.000	24.000	24.000	24.000	24.000	24.000	24.000	24.000	24.000	24.000	24.000
Ti/(Ti+Cr+Al)	0.082	0.482	0.471	0.531	0.558	0.580	0.544	0.506	0.539	0.088	0.086	0.554	0.521	0.577	0.576	0.552	0.572	0.577
$Fe^{2+}/(Fe^{2+}+Mg)$	0.406	0.942	0.871	0.876	0.454	0.439	0.568	0.606	0.689	0.414	0.419	0.895	0.857	0.459	0.458	0.727	0.511	0.565

Table B6. Spinel compositions for samples SK-1 continued.

	SK-1 24-a	SK-1 1 /-b	SK-1 2-b	SK-1 3-b	SK-1 4-b	SK-1 5-b	SK-1 6-b	SK-1 7-	SK-1 7-b	SK-1 9-b	SK-1 10-b	SK-1 11-b	SK-1 12-b	SK-1 13-b	SK-1 14-b	SK-1 15-b	SK-1 16-b	SK-1 17-b
SiO_2	0.08	0.12	0.12	0.09	0.08	0.05	0.15	0.13	0.08	0.12	0.1	0.09	0.07	0.1	0.09	0.16	0.09	0.18
TiO_2	11.22	13.65	15.37	15.72	17.88	17.3	5.65	5.63	17.27	17.87	19.28	19.2	17.91	15.62	6.61	6.14	19.27	15.44
Al_2O_3	7.87	7.86	7.44	7.57	8.23	6.79	10.51	9.68	6.64	6.26	6.03	5.96	5.82	6.04	8.03	11.6	5.69	8.01
$Cr2O_3$	0.01	0	0.06	0.21	0.61	0.07	44.08	44.4	0.52	0.93	0.77	2.23	1.99	7.36	39.6	41.7	1.18	0.25
V_2O_3	0.04	0.03	0.04	0.04	0.06	0.04	0.21	0.21	0.04	0.05	0.06	0.06	0.06	0.04	0.15	0.22	0.05	0.03
Fe_2O_3	37.62	34.69	33.05	34.42	30.36	34.30	8.48	8.65	28.68	26.49	28.83	28.56	25.03	24.67	13.38	8.70	30.15	32.07
FeO	34.60	31.26	29.41	24.56	27.15	25.41	16.13	16.31	31.73	36.54	26.64	26.08	37.78	38.83	16.93	17.11	25.09	28.66
MnO	1.12	0.89	0.72	0.49	0.54	0.53	0.49	0.5	1.07	1.64	0.65	0.72	1.66	1.63	0.48	0.36	0.67	0.58
MgO	3.58	7.49	9.77	13.39	13.61	14.23	14.52	14.15	8.98	6.08	14	14.49	5.05	3.57	14.02	14.42	15.12	10.58
CaO	0.43	0.34	0.39	0.35	0.1	0.12	0.1	0.11	0.17	0.11	0.17	0.14	0.14	0.13	0.08	0.09	0.19	0.19
ZnO	0.23	0.06	0.05	0.06	0.05	0.05	0.05	0.06	0.07	0.05	0.07	0.07	0.09	0.21	0.07	0.04	0.08	0.07
Total	96.80	96.38	96.42	96.90	98.67	98.89	100.3	99.84	95.25	96.14	96.60	97.60	95.60	98.20	99.44	100.5	97.58	96.05
								Calculated to 24 cations										
Si	0.023	0.034	0.034	0.024	0.021	0.013	0.038	0.034	0.023	0.035	0.027	0.024	0.021	0.029	0.024	0.041	0.024	0.050
Ti	2.470	2.925	3.240	3.215	3.578	3.469	1.086	1.094	3.712	3.895	3.955	3.891	3.962	3.403	1.302	1.174	3.895	3.238
Al	2.715	2.639	2.458	2.426	2.581	2.133	3.167	2.948	2.236	2.138	1.938	1.892	2.017	2.062	2.479	3.476	1.802	2.632
Cr	0.002	0.000	0.013	0.045	0.128	0.015	8.909	9.071	0.117	0.213	0.166	0.475	0.463	1.686	8.201	8.384	0.251	0.055
V	0.009	0.007	0.009	0.009	0.013	0.009	0.043	0.044	0.009	0.012	0.013	0.013	0.014	0.009	0.032	0.045	0.011	0.007
Fe(iii)	8.286	7.436	6.972	7.041	6.079	6.880	1.632	1.682	6.167	5.777	5.917	5.789	5.540	5.378	2.637	1.665	6.097	6.728
Fe(ii)	8.469	7.447	6.893	5.585	6.041	5.663	3.448	3.525	7.583	8.856	6.076	5.876	9.291	9.405	3.708	3.639	5.638	6.682
Mn	0.278	0.215	0.171	0.113	0.122	0.120	0.106	0.109	0.259	0.403	0.150	0.164	0.414	0.400	0.106	0.078	0.153	0.137
Mg	1.562	3.181	4.083	5.428	5.399	5.655	5.534	5.451	3.826	2.627	5.693	5.820	2.214	1.542	5.475	5.467	6.058	4.399
Ca	0.135	0.104	0.117	0.102	0.029	0.034	0.027	0.030	0.052	0.034	0.050	0.040	0.044	0.040	0.022	0.025	0.055	0.057
Zn	0.050	0.013	0.010	0.012	0.010	0.010	0.009	0.011	0.015	0.011	0.014	0.014	0.020	0.045	0.014	0.008	0.016	0.014
Total	24.000	24.000	24.000	24.000	24.000	24.000	24.000	24.000	24.000	24.000	24.000	24.000	24.000	24.000	24.000	24.000	24.000	24.000
Ti/(Ti+Cr+Al)	0.476	0.526	0.567	0.565	0.569	0.618	0.083	0.083	0.612	0.624	0.653	0.622	0.615	0.476	0.109	0.090	0.655	0.546
$Fe^{2+}/(Fe^{2+}+Mg)$	0.844	0.701	0.628	0.507	0.528	0.500	0.384	0.393	0.665	0.771	0.516	0.502	0.808	0.859	0.404	0.400	0.482	0.603

Table B6. Spinel compositions for samples SK-1 continued.

	SK-1 24-b	SK-1 25	SK-1 26	SK-1 27	SK-1 28	SK-1 29	SK-1 30	SK-1 31	SK-1 32	SK-1 33	SK-1 34	SK-1 35	SK-1 36	SK-1 37	SK-1 38	SK-1 39	SK-1 42	SK-1 43
SiO_2	0.1	0.06	0.07	0.06	0.05	0.06	0.08	0.16	0.1	0.23	0.07	0.07	0.07	0.46	0.75	0.13	0.12	0.09
TiO_2	5.78	7.73	17.03	16.44	17.88	18.53	17.4	6.13	5.61	16.68	12.74	6.55	12.73	21.47	21.55	14	5.93	17.79
Al_2O_3	8.1	7.91	7.2	5.92	7.94	7.89	6.95	11.56	9.18	5.49	5.94	8.14	7.26	0.62	0.96	6.09	9.51	6.45
$Cr2O_3$	45.82	33.89	0.25	1.04	1.4	0.78	0.64	42.02	45.22	3.37	10.31	43.41	21.21	0.2	0.17	8.32	39.44	0.54
V_2O_3	0.17	0.12	0.05	0.05	0.07	0.05	0.07	0.22	0.2	0.07	0.05	0.16	0.08	0.04	0.05	0.05	0.18	0.03
Fe_2O_3	8.43	17.25	32.98	29.53	31.26	30.29	34.23	8.00	8.00	25.87	26.26	9.80	23.10	22.66	21.54	25.81	14.28	33.09
FeO	19.07	19.51	25.11	37.66	24.61	25.58	23.70	18.28	17.11	43.43	40.40	17.98	19.70	45.44	45.05	40.49	14.21	24.01
MnO	0.37	0.48	0.49	1.47	0.64	0.65	0.56	0.25	0.35	1.72	1.7	0.45	0.7	2.28	2.26	1.84	0.48	0.55
MgO	12.5	13.07	13.95	4.41	15.24	14.93	15.46	13.71	13.52	0.74	0.62	13.52	15.69	1.02	1.65	1.42	15.58	15.11
CaO	0.06	0.09	0.27	0.49	0.12	0.1	0.19	0.1	0.18	0.41	0.18	0.06	0.12	0.68	0.55	0.11	0.2	0.28
ZnO	0.08	0.06	0.04	0.06	0.06	0.08	0.06	0.02	0.08	0.77	0.6	0.08	0.12	0.03	0.05	0.38	0.09	0.06
Total	100.48	100.17	97.43	97.13	99.27	98.94	99.34	100.45	99.55	98.78	98.87	100.22	100.78	94.90	94.59	98.63	100.02	98.00
								Calculated to 24 cations										
Si	0.026	0.016	0.019	0.017	0.013	0.016	0.021	0.041	0.026	0.068	0.021	0.018	0.018	0.144	0.233	0.038	0.031	0.024
Ti	1.138	1.526	3.456	3.603	3.525	3.671	3.442	1.179	1.100	3.703	2.826	1.284	2.468	5.048	5.042	3.089	1.143	3.575
Al	2.498	2.448	2.290	2.033	2.453	2.449	2.154	3.483	2.820	1.910	2.064	2.500	2.206	0.228	0.352	2.106	2.872	2.031
Cr	9.479	7.035	0.053	0.240	0.290	0.162	0.133	8.494	9.318	0.786	2.404	8.942	4.323	0.049	0.042	1.930	7.990	0.114
V	0.036	0.025	0.011	0.012	0.015	0.011	0.015	0.045	0.042	0.017	0.012	0.033	0.017	0.010	0.012	0.012	0.037	0.006
Fe(iii)	1.660	3.408	6.695	6.474	6.165	6.004	6.773	1.539	1.569	5.746	5.827	1.921	4.482	5.329	5.043	5.698	2.753	6.652
Fe(ii)	4.173	4.283	5.665	9.176	5.395	5.635	5.212	3.909	3.729	10.718	9.962	3.919	4.247	11.878	11.720	9.932	3.045	5.364
Mn	0.082	0.107	0.112	0.363	0.142	0.145	0.125	0.054	0.077	0.430	0.425	0.099	0.153	0.604	0.595	0.457	0.104	0.124
Mg	4.876	5.116	5.612	1.916	5.956	5.863	6.061	5.226	5.253	0.326	0.273	5.252	6.030	0.475	0.765	0.621	5.952	6.018
Ca	0.017	0.025	0.078	0.153	0.034	0.028	0.054	0.027	0.050	0.130	0.057	0.017	0.033	0.228	0.183	0.035	0.055	0.080
Zn	0.015	0.012	0.008	0.013	0.012	0.016	0.012	0.004	0.015	0.168	0.131	0.015	0.023	0.007	0.011	0.082	0.017	0.012
Total	24.000	24.000	24.000	24.000	24.000	24.000	24.000	24.000	24.000	24.000	24.000	24.000	24.000	24.000	24.000	24.000	24.000	24.000
Ti/(Ti+Cr+Al)	0.087	0.139	0.596	0.613	0.562	0.584	0.601	0.090	0.083	0.579	0.387	0.101	0.274	0.948	0.928	0.434	0.095	0.625
$Fe^{2+/}(Fe^{2+}+Mg)$	0.461	0.456	0.502	0.827	0.475	0.490	0.462	0.428	0.415	0.971	0.973	0.427	0.413	0.962	0.939	0.941	0.338	0.471

Table B6. Spinel compositions for samples SK-1 continued.

	SK-1 44	SK-1 45	SK-1 46	SK-1 47	SK-1 48	SK-1 49	SK-1 50	SK-1 51	SK-1 52	SK-1 53	SK-1 54	SK-1 55	SK-1 56	SK-1 57	SK-1 58	SK-1 59	SK-1 60	SK-1 61
SiO_2	0.13	0.11	0.09	0.38	0.18	0.17	0.11	0.1	0.18	0.17	0.12	0.1	0.08	0.08	0.17	0.14	0.23	0.2
TiO_2	5.56	5.75	15.82	15.73	5.66	5.74	17.04	15.62	5.82	5.7	18.11	19.45	18.14	15.66	5.51	6.14	12.23	6.34
Al_2O_3	8.79	9.09	6.65	5.74	10.76	10.5	5.47	5.32	11.27	11.29	5.36	5.33	6.35	7.2	10.71	8.77	8.04	10.86
$Cr2O_3$	44.11	41.12	2.24	2.86	43.09	43.75	2.03	2.11	42.68	42.58	4.4	2.24	0.54	0.04	40.44	36.34	0.2	41.83
V_2O_3	0.17	0.16	0.07	0.05	0.24	0.21	0.06	0.03	0.22	0.21	0.06	0.07	0.07	0.04	0.19	0.12	0.02	0.23
Fe_2O_3	9.97	12.87	28.04	26.13	8.36	8.68	25.73	28.78	7.55	7.67	22.80	22.70	32.29	32.66	12.79	17.83	33.66	8.60
FeO	17.15	16.37	37.50	42.39	17.02	17.05	43.53	42.31	18.02	17.73	42.35	42.32	24.71	30.42	13.13	13.37	39.27	17.77
MnO	0.44	0.47	1.6	1.73	0.34	0.35	1.66	1.61	0.25	0.32	2.39	2.3	0.59	0.91	0.47	0.53	1.29	0.4
MgO	13.53	14.17	4.3	0.85	13.77	14.03	0.83	0.57	13.48	13.46	2.18	3.05	14.89	9.29	15.94	15.8	0.98	13.93
CaO	0.1	0.1	0.17	0.16	0.36	0.27	0.26	0.42	0.11	0.14	0.12	0.12	0.16	0.15	0.55	0.48	0.33	0.17
ZnO	0.09	0.09	0.07	0.59	0.08	0.06	0.36	0.63	0.08	0.07	0.22	0.06	0.06	0.08	0.11	0.14	0.81	0.07
Total	100.04	100.30	96.55	96.61	99.86	100.81	97.08	97.49	99.67	99.34	98.11	97.73	97.88	96.53	100.01	99.67	97.06	100.40
								Calculated to 24 cations										
Si	0.034	0.028	0.026	0.114	0.046	0.043	0.033	0.030	0.046	0.044	0.035	0.029	0.021	0.023	0.043	0.036	0.068	0.051
Ti	1.088	1.118	3.478	3.562	1.097	1.103	3.846	3.526	1.130	1.110	4.000	4.283	3.656	3.316	1.053	1.190	2.734	1.221
Al	2.695	2.769	2.291	2.036	3.267	3.161	1.935	1.882	3.428	3.444	1.855	1.839	2.005	2.389	3.206	2.663	2.816	3.278
Cr	9.074	8.403	0.518	0.681	8.776	8.835	0.482	0.501	8.708	8.713	1.022	0.519	0.114	0.009	8.120	7.403	0.047	8.471
V	0.035	0.033	0.016	0.012	0.050	0.043	0.014	0.007	0.046	0.044	0.014	0.016	0.015	0.009	0.039	0.025	0.005	0.047
Fe(iii)	1.952	2.503	6.166	5.919	1.621	1.668	5.811	6.499	1.467	1.493	5.038	5.001	6.511	6.917	2.444	3.457	7.527	1.658
Fe(ii)	3.731	3.538	9.166	10.671	3.666	3.642	10.923	10.617	3.890	3.838	10.401	10.360	5.537	7.161	2.789	2.882	9.761	3.806
Mn	0.097	0.103	0.396	0.441	0.074	0.076	0.422	0.409	0.055	0.070	0.594	0.570	0.134	0.217	0.101	0.116	0.325	0.087
Mg	5.248	5.460	1.874	0.381	5.289	5.343	0.371	0.255	5.186	5.194	0.954	1.331	5.948	3.899	6.036	6.069	0.434	5.320
Ca	0.028	0.028	0.053	0.052	0.099	0.074	0.084	0.135	0.030	0.039	0.038	0.038	0.046	0.045	0.150	0.133	0.105	0.047
Zn	0.017	0.017	0.015	0.131	0.015	0.011	0.080	0.140	0.015	0.013	0.048	0.013	0.012	0.017	0.021	0.027	0.178	0.013
Total	24.000	24.000	24.000	24.000	24.000	24.000	24.000	24.000	24.000	24.000	24.000	24.000	24.000	24.000	24.000	24.000	24.000	24.000
Ti/(Ti+Cr+Al)	0.085	0.091	0.553	0.567	0.083	0.084	0.614	0.597	0.085	0.084	0.582	0.645	0.633	0.580	0.085	0.106	0.488	0.094
$Fe^{2+}/(Fe^{2+}+Mg)$	0.416	0.393	0.830	0.965	0.409	0.405	0.967	0.977	0.429	0.425	0.916	0.886	0.482	0.647	0.316	0.322	0.957	0.417

Table B7. Spinel compositions for samples SK-1 and SK-2.

	SK-1 62	SK-1 63	SK-1 64	SK-1 65	SK-1 66	SK-1 67	SK-1 68	SK-1 69	SK-1 70	SK-1 71	SK-1 72	SK-1 73	SK-1 75	SK-1 76	SK-1 77	SK-2 81	SK-2 84	SK-2 86
SiO_2	0.09	0.1	0.08	0.13	0.15	0.08	0.27	0.16	0.14	0.1	0.2	0.08	0.1	0.1	0.09	0.07	0.09	0.27
TiO_2	10.72	18.63	16.99	6.17	6.28	19.21	18.36	6.08	5.88	5.63	16.79	18.43	15.34	6	16.61	53.96	53.82	51.35
Al_2O_3	8	5.59	5.54	11.22	11.09	5.79	5.08	11.5	10.97	9.03	5.64	5.71	6.06	8.36	5.64	0.28	0.27	0.37
$Cr2O_3$	31.16	1.97	4.87	42.43	42.84	2.67	0.84	42.84	42.91	45.98	1.84	2.46	7.21	44.16	1.76	1.64	1.63	1.95
V_2O_3	0.13	0.04	0.09	0.24	0.26	0.06	0.05	0.22	0.23	0.16	0.03	0.05	0.07	0.16	0.06	0.08	0.11	0.07
Fe_2O_3	14.85	24.54	25.00	7.70	7.39	22.28	24.41	7.32	8.01	8.11	26.66	24.11	24.90	10.05	27.17	0	0	0
FeO	20.34	37.38	38.46	18.76	19.27	40.70	44.43	18.40	17.89	17.72	43.30	41.15	41.98	16.78	43.19	28.93	28.57	32.98
MnO	0.43	1.78	2.01	0.34	0.37	2.16	1.69	0.31	0.35	0.4	1.65	2.23	2.08	0.56	1.66	0.3	0.27	1.31
MgO	14.4	5.74	4.18	13.32	13.14	3.95	1.08	13.58	13.59	13.43	1.15	3.21	1.17	13.91	0.83	13.88	14.12	9.86
CaO	0.08	0.18	0.14	0.02	0.04	0.09	0.15	0.07	0.08	0.05	0.13	0.17	0.07	0.13	0.29	0.43	0.47	0.63
ZnO	0.07	0.04	0.14	0.09	0.06	0.11	0.45	0.07	0.07	0.06	0.4	0.06	0.55	0.1	0.49	0.02	0.01	0
Total	100.27	96.00	97.50	100.42	100.89	97.10	96.81	100.54	100.12	100.67	97.79	97.66	99.53	100.31	97.79	99.59	99.36	98.79
Calculated to 24 cations																		
Si	0.023	0.029	0.023	0.033	0.038	0.023	0.081	0.041	0.036	0.026	0.059	0.023	0.029	0.026	0.027	0.019	0.025	0.076
Ti	2.093	4.086	3.719	1.192	1.210	4.218	4.152	1.169	1.138	1.095	3.752	4.052	3.362	1.171	3.723	11.074	11.047	10.907
Al	2.447	1.921	1.900	3.396	3.348	1.992	1.800	3.466	3.326	2.751	1.975	1.967	2.081	2.556	1.981	0.090	0.087	0.123
Cr	6.394	0.454	1.120	8.615	8.676	0.616	0.200	8.661	8.728	9.398	0.432	0.568	1.661	9.056	0.415	0.354	0.352	0.435
V	0.027	0.009	0.021	0.049	0.053	0.014	0.012	0.045	0.047	0.033	0.007	0.012	0.016	0.033	0.014	0.018	0.024	0.016
Fe(iii)	2.900	5.385	5.475	1.489	1.425	4.894	5.523	1.408	1.550	1.577	5.962	5.303	5.460	1.962	6.092	0.000	0.000	0.000
Fe(ii)	4.414	9.115	9.359	4.029	4.127	9.936	11.170	3.934	3.850	3.832	10.758	10.058	10.229	3.639	10.761	6.601	6.520	7.788
Mn	0.095	0.440	0.495	0.074	0.080	0.534	0.430	0.067	0.076	0.088	0.415	0.552	0.513	0.123	0.419	0.069	0.062	0.313
Mg	5.572	2.495	1.813	5.100	5.018	1.719	0.484	5.177	5.213	5.176	0.509	1.399	0.508	5.379	0.369	5.646	5.745	4.151
Ca	0.022	0.056	0.044	0.006	0.011	0.028	0.048	0.019	0.022	0.014	0.041	0.053	0.022	0.036	0.093	0.126	0.137	0.191
Zn	0.013	0.009	0.030	0.017	0.011	0.024	0.100	0.013	0.013	0.011	0.088	0.013	0.118	0.019	0.108	0.004	0.002	0.000
Total	24.000	24.000	24.000	24.000	24.000	24.000	24.000	24.000	24.000	24.000	24.000	24.000	24.000	24.000	24.000	24.000	24.000	24.000
Ti/(Ti+Cr+Al)	0.191	0.632	0.552	0.090	0.091	0.618	0.675	0.088	0.086	0.083	0.609	0.615	0.473	0.092	0.608	0.961	0.962	0.951
$Fe^{2+}/(Fe^{2+}+Mg)$	0.442	0.785	0.838	0.441	0.451	0.852	0.958	0.432	0.425	0.425	0.955	0.878	0.953	0.404	0.967	0.539	0.532	0.652

Table B8. Spinel compositions for samples SK-2.

	SK-2 104	SK-2 107	SK-2 108	SK-2 109	SK-2 110	SK-2 111	SK-2 115	SK-2 116	SK-2 117	SK-2 118	SK-2 119	SK-2 120	SK-2 125	SK-2 131	SK-2 132	SK-2 134	SK-2 135	SK-2 137
SiO_2	0.19	0.09	0.08	0.06	0.02	0	0.07	0.13	0.09	0.17	0.21	0.76	0.07	0.05	0.1	0.04	0.08	0.09
TiO_2	54.41	52.41	53.69	53.43	61.41	61.76	49.4	49.64	53.01	53.24	53.88	53.03	53.44	50.37	51	53.95	54.1	53.91
Al_2O_3	0.33	0.02	0.52	0.53	0.23	0.22	0.38	0.38	0.24	0.26	0.37	0.42	0.4	0.02	0.02	0.36	0.36	0.39
$Cr2O_3$	2.06	0.02	2.18	2.02	14.79	14.48	1.66	1.55	2.09	2.04	1.72	1.58	1.7	0.03	0.04	2.17	2.34	1.9
V_2O_3	0.09	0	0.05	0.07	0.3	0.34	0.14	0.12	0.08	0.07	0.02	0.03	0.05	0.03	0.01	0.13	0.1	0.12
Fe_2O_3	0	0	0	0	0	0	0	0	0	0	0	0	0	0	0	0	0	0
FeO	27.45	35.93	27.06	27.08	8.73	8.81	39.24	38.96	28.92	28.96	27.57	27.62	27.9	38.2	37.47	28.86	29.2	28.74
MnO	0.44	8.88	0.48	0.41	0.1	0.13	5.21	5.28	0.34	0.31	0.43	0.4	0.4	8.62	8.8	0.35	0.33	0.31
MgO	14.63	0.05	15.37	15.33	3.71	3.47	1.1	1.18	13.9	13.81	15.08	15.23	14.78	0.17	0.22	13.45	13.49	12.23
CaO	0.5	0.94	0.5	0.47	0.83	0.81	0.33	0.37	0.3	0.33	0.3	0.61	0.26	0.96	0.91	0.66	0.67	0.81
ZnO	0.02	0.02	0.01	0	0.01	0	0.02	0.02	0.03	0.03	0.04	0	0.02	0	0.02	0	0	0.01
Total	100.12	98.36	99.94	99.4	90.13	90.02	97.55	97.63	99	99.22	99.62	99.68	99.02	98.45	98.59	99.97	100.67	98.51
							Calculated to 24 cations											
Si	0.051	0.028	0.021	0.016	0.007	0.000	0.021	0.040	0.025	0.047	0.057	0.204	0.019	0.015	0.031	0.011	0.022	0.025
Ti	11.049	12.096	10.849	10.852	15.348	15.495	11.384	11.421	10.936	10.967	10.953	10.731	10.948	11.578	11.709	11.060	11.016	11.303
Al	0.105	0.007	0.165	0.169	0.090	0.086	0.137	0.137	0.078	0.084	0.118	0.133	0.128	0.007	0.007	0.116	0.115	0.128
Cr	0.440	0.005	0.463	0.431	3.885	3.819	0.402	0.375	0.453	0.442	0.368	0.336	0.366	0.007	0.010	0.468	0.501	0.419
V	0.019	0.000	0.011	0.015	0.080	0.091	0.034	0.029	0.018	0.015	0.004	0.006	0.011	0.007	0.002	0.028	0.022	0.027
Fe(iii)	0.000	0.000	0.000	0.000	0.000	0.000	0.000	0.000	0.000	0.000	0.000	0.000	0.000	0.000	0.000	0.000	0.000	0.000
Fe(ii)	6.197	9.220	6.079	6.115	2.426	2.457	10.053	9.966	6.633	6.632	6.231	6.214	6.354	9.762	9.564	6.578	6.610	6.699
Mn	0.101	2.308	0.109	0.094	0.028	0.037	1.352	1.368	0.079	0.072	0.098	0.091	0.092	2.231	2.275	0.081	0.076	0.073
Mg	5.889	0.023	6.156	6.172	1.838	1.726	0.502	0.538	5.684	5.639	6.076	6.109	6.002	0.077	0.100	5.466	5.445	5.082
Ca	0.145	0.309	0.144	0.136	0.295	0.289	0.108	0.121	0.088	0.097	0.087	0.176	0.076	0.314	0.298	0.193	0.194	0.242
Zn	0.004	0.005	0.002	0.000	0.002	0.000	0.005	0.005	0.006	0.006	0.008	0.000	0.004	0.000	0.005	0.000	0.000	0.002
Total	24.000	24.000	24.000	24.000	24.000	24.000	24.000	24.000	24.000	24.000	24.000	24.000	24.000	24.000	24.000	24.000	24.000	24.000
Ti/(Ti+Cr+Al)	0.953	0.999	0.945	0.948	0.794	0.799	0.955	0.957	0.954	0.954	0.958	0.958	0.957	0.999	0.999	0.950	0.947	0.954
$Fe^{2+}/(Fe^{2+}+Mg)$	0.513	0.998	0.497	0.498	0.569	0.587	0.952	0.949	0.539	0.540	0.506	0.504	0.514	0.992	0.990	0.546	0.548	0.569

Table B5. Spinel compositions for samples SK-2 continued.

	SK-2 138	SK-2 141	SK-2 142	SK-2 143	SK-2 144	SK-2 145	SK-2 146	SK-2 147	SK-2 149	SK-2 150	SK-2 152	SK-2 153	SK-2 154	SK-2 156
SiO_2	0.09	0.07	0.13	0.23	0.06	0.11	0.13	0.38	0.05	0.01	0.02	0.06	0.06	0.1
TiO_2	54.2	50.74	50.97	50.13	51.42	51.31	50.74	29.51	3.52	3.54	3.43	52.85	53.19	51.26
Al_2O_3	0.41	0.01	0.02	0.01	0.02	0	0.04	0.93	0.59	0.6	0.6	0.4	0.4	0.01
$Cr2O_3$	2	0	0	0	0	0.02	0.02	2.08	58.82	58.9	58.48	2.55	2.61	0
V_2O_3	0.08	0	0	0.02	0	0.01	0.02	0.03	0.41	0.41	0.39	0.11	0.09	0.03
Fe_2O_3	0	0	0	0	0	0	0	4.82	5.68	5.84	6.63	0	0	0
FeO	28.78	36.78	36.98	36.68	37.25	37.21	37.91	52.94	21.93	21.79	20.80	29.39	29	37.13
MnO	0.24	9.13	9.02	8.93	9.4	9.21	8.8	3.49	0.34	0.3	0.43	0.39	0.33	9.13
MgO	12.79	0.1	0.1	0.15	0.14	0.14	0.19	0.17	8.36	8.46	8.88	13.15	13.32	0.16
CaO	0.68	0.5	0.42	0.55	0.46	0.5	0.37	0.51	0.13	0.17	0.22	0.35	0.29	0.24
ZnO	0.01	0	0	0	0	0.03	0	0.44	0.09	0.1	0.12	0.03	0.01	0.01
Total	99.28	97.33	97.64	96.7	98.75	98.54	98.22	95.29	99.92	100.13	100.00	99.28	99.30	98.07
						Calculated to 24 cations								
Si	0.025	0.022	0.040	0.072	0.018	0.034	0.040	0.118	0.014	0.003	0.006	0.016	0.016	0.031
Ti	11.238	11.831	11.849	11.751	11.814	11.813	11.712	6.890	0.741	0.743	0.719	10.929	10.988	11.867
Al	0.133	0.004	0.007	0.004	0.007	0.000	0.014	0.340	0.195	0.197	0.197	0.130	0.129	0.004
Cr	0.436	0.000	0.000	0.000	0.000	0.005	0.005	0.510	13.009	12.993	12.878	0.554	0.567	0.000
V	0.018	0.000	0.000	0.005	0.000	0.002	0.005	0.007	0.092	0.092	0.087	0.024	0.020	0.007
Fe(iii)	0.000	0.000	0.000	0.000	0.000	0.000	0.000	1.125	1.195	1.227	1.390	0.000	0.000	0.000
Fe(ii)	6.634	9.534	9.557	9.559	9.515	9.524	9.728	13.742	5.130	5.084	4.845	6.757	6.661	9.556
Mn	0.056	2.397	2.361	2.357	2.432	2.388	2.287	0.918	0.081	0.071	0.101	0.091	0.077	2.380
Mg	5.257	0.046	0.046	0.070	0.064	0.064	0.087	0.079	3.487	3.519	3.687	5.390	5.454	0.073
Ca	0.201	0.166	0.139	0.184	0.151	0.164	0.122	0.170	0.039	0.051	0.066	0.103	0.085	0.079
Zn	0.002	0.000	0.000	0.000	0.000	0.007	0.000	0.101	0.019	0.021	0.025	0.006	0.002	0.002
Total	24.000	24.000	24.000	24.000	24.000	24.000	24.000	24.000	24.000	24.000	24.000	24.000	24.000	24.000
Ti/(Ti+Cr+Al)	0.952	1.000	0.999	1.000	0.999	1.000	0.998	0.890	0.053	0.053	0.052	0.941	0.940	1.000
$Fe^{2+}/(Fe^{2+}+Mg)$	0.558	0.995	0.995	0.993	0.993	0.993	0.991	0.994	0.595	0.591	0.568	0.556	0.550	0.992

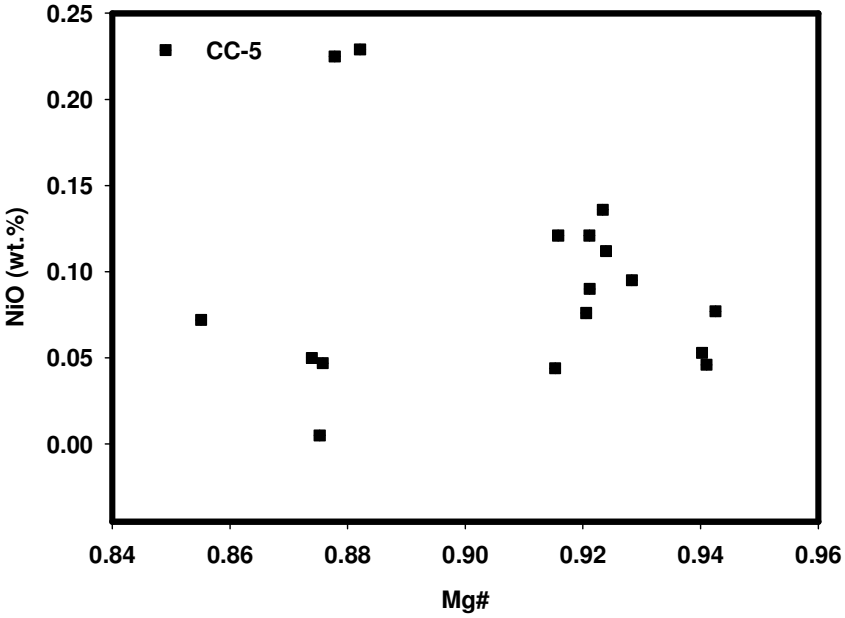

Figure 1. Variation of Mg# and NiO contents in olivines of the CC-5 Kimberlites.

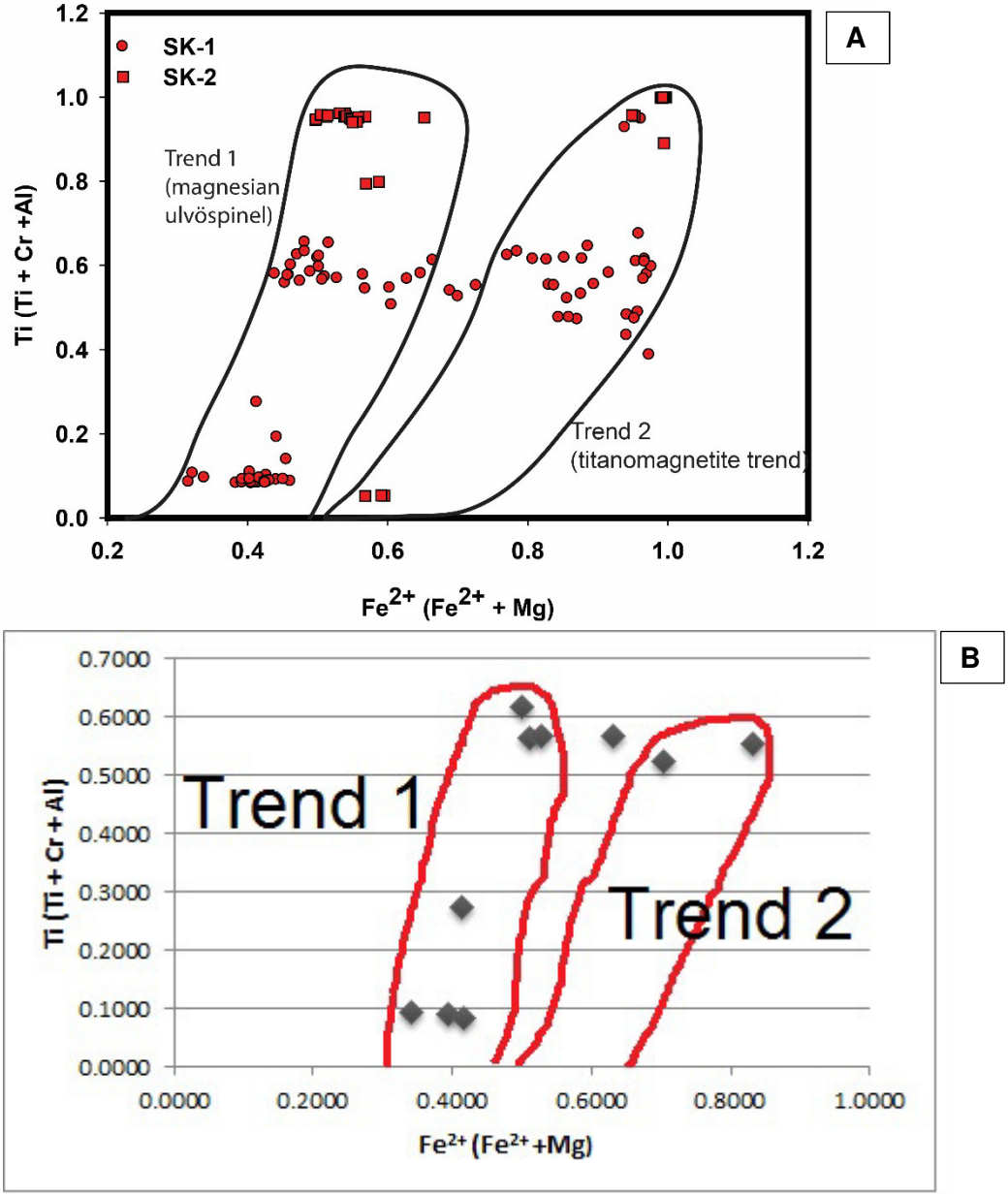

Figure 2. $Fe^{2+/(}Fe^{2+}$ + Mg) vs Ti/(Ti+C+Al) in (mol fraction) for groundmass spinels of the the Eastern Dharwar Craton kimberlites. (a) Siddanpalle kimberlites (b) Chigicherla kimberlites.

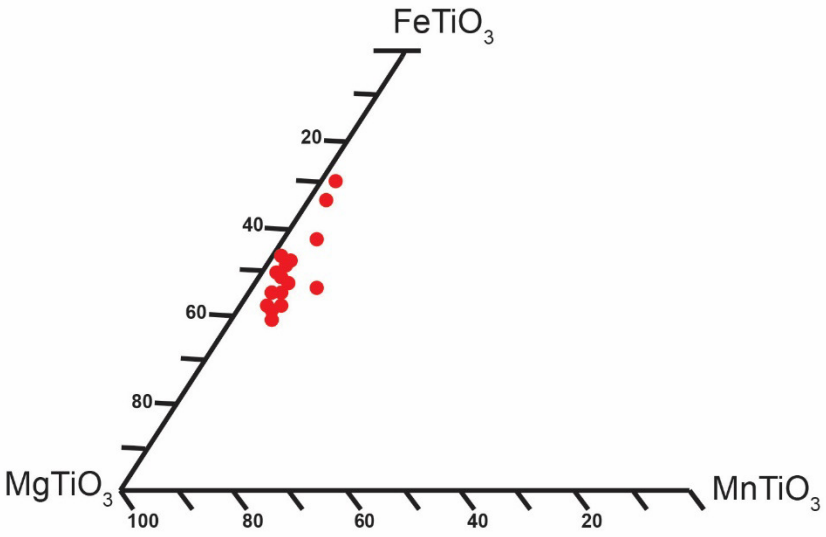

Figure 3. Ilmenite compositions (mol%) from the Siddanpalle (SK-2) kimberlite, plotted in the ternary system $FeTiO_3$ (ilmenite)-$MnTiO_3$ (pyrophanite)-$MgTiO_3$ (geikielite).

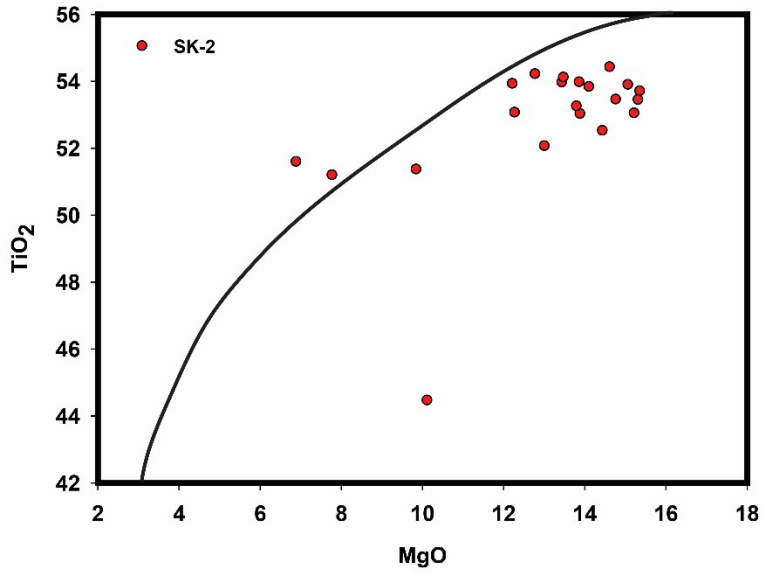

Figure 4. TiO_2 (wt.%) vs MgO (wt.%) for the SK-2 ilmenite comspositions, showing ilmenites plotting to the right of the kimberlite ilmenite field. The black line represents the bounding reference line of the kimberlitic ilmenite field (Wyatt-et al., 2004)

Appendix C- Apatite Thermochronometry

Application of low temperature thermochronometry is a powerful technique for constraining thermal history information on samples as they pass through isotherms in the upper crust. A critical consideration when selecting which low temperature technique method to use are the closure temperatures associated with each system (Wildman et al., 2013). Phosphates such as apatite, monazite and xenotime quantitatively retain He at Earth surface temperatures and as a result these minerals can be used to accurately date the formation of rapidly cooled rocks such as lava flows. Apatite (U-Th)/He thermochronometry has emerged as an important tool for quantifying the cooling histories of rocks as they pass through the upper 1-3 km of the crust (Ehlers & Farley, 2003) and has been used for reconstructing geodynamic processes of the upper crust including the land surface. Determination of apatite He (AHe) ages involves three steps: measurements of grain dimensions (length and width) for determination of the α-ejection correction, measurement of He content and its isotopic composition ($^{4}He/^{3}He$) and lastly measurement of the U and Th content (Farley & Stockli, 2002).

The apatite (U-Th)/He thermochronometer is based on the production of radiogenic He (^{4}He) through radioactive decay of ^{238}U, ^{235}U, ^{232}Th, and ^{147}Sm (Spiegel et al., 2009). Each transformation in the decay results in the generation of alpha particle or He nucleus (Hourigan et al., 2005).The decay of U and Th are one of the earliest techniques utilized by geochronologists to determine ages of rocks (Zeitler et al.,1987). These authors suggested that He can be quantitatively retained in well-crystallized lattices over geological time spans. The use of apatite emerges not only from the fact that it has moderately high U and Th content (Ehlers & Farley, 2003) but He accumulation in apatite occurs only in temperatures below ~ 70-75^{o} C, above this temperatures He retentivity is lost. Helium is found in low concentration in the atmosphere (5 ppm as opposed to 1% levels of Argon), this leads to very low contamination of samples because air-derived He is unlikely to be present in most minerals (Farley & Stockli, 2002). The low concentration of He also leads to the fast production rate of He from the decay of U and Th (Zeitler et al., 1987)

Complications in AHe dating are induced by alpha decay; α-decay of actinides releases a huge amount of energy taken up mostly in the form of energy. The α-particles may be ejected out of the target crystal or injected into a crystal from decay occurring in the surrounding minerals. To account for this (Farley & Stockli, 2002) suggests that grain dimensions measurements should be done prior to analysis in order to correct ages using the computed F_T values (fraction of U and Th in a crystal capable of yielding α particles that stop within the crystal, explained in detail

in their paper). This technique assumes the (i) there is no extra He present in the sample in the form of Inclusions and that the decay series is secular (ii) the grain to be dated must include the entire original grain surface; and (iii) the F_T model assumes that the parent nuclide distribution is homogeneous. Of greatest concern are mineral inclusions (typically zircon with high U and Th contents) and zonation in apatites crystals as this may lead to an underestimation or/ overestimation of the He age (Farley & Stockli, 2002). Challenges of AHe thermochronometry arise when rocks contain fractured anhedral crystals, as such grains impede the α-ejection correction, because it is not obvious to identify the original grain size. Some rocks yield grains with uneven surface and or tiny crystals, the latter type of grains is problematic because grain size is proportional to α-correction, where the smaller the grain the larger the correction, which limits the precision of the AHe applied to small crystals. The technique is well documented in a paper published by Farley et al. (1996), and these authors also provide solutions for alpha particle ejection.

An increasing number of recent studies report apatite (U-Th)/He ages which are older than expected on the basis of apatite fission track (AFT) data. AHe ages should complement results with AFT, potentially constraining very low magnitudes of heating and cooling (Sahu et al. (2013). Paul et al. (2006) reported discrepancies between (U-Th)/He and apatite fission track ages, where these differences were initially thought to emanate from fission track annealing but they concluded that these differences should be linked to the degree of radiation damage (Wolf, 1996; Stockli et al., 2000; Farley, 2002; Reiners & Ehlers, 2005; Spotila, 2005; Guenthner et al., 2013) within the crystal lattice. Flowers et al. (2009) introduced radiation damage accumulation and annealing model (RDAAM), which accounts for the evolution of apatite He diffusitivity in response to both damage accumulation and annealing. RDAAM is a version of He trapping model (HeTM) that uses effective fission track density as a proxy for the accumulated radiation damage as opposed to utility of He concentration as the radiation damage proxy. Under some circumstances radiation damage and He will not accumulate proportinally, damage may accumulate at temperatures where He retentivity is lost or damage may anneal at a different rate from that which He is lost, therefore the use of He concentration is a limitation. The accumulation of α-radiation damage in apatite crystals progressively influences He retentivity, to an extend were the Partial Retention Zone (PRZ) will continually shift to higher temperatures. The RDAAM explains some discrepancies found between He ages and AFT ages, i.e. (U-Th)/He dates yields older ages than AFT ages (Flowers et al., 2009).

An apatite held at 48°C for 100 Ma will have a He age older than the apatite held at 52°C. Figure 5 below shows the relationship between He ages and apatite He Partial Retention Zone (HePRZ). In the PRZ (Partial Retention Zone) the exact temperature zone depends on the

holding duration. During accumulation of radiation damage for the RDAAM, the PRZ moves to higher temperatutes for longer holding times.

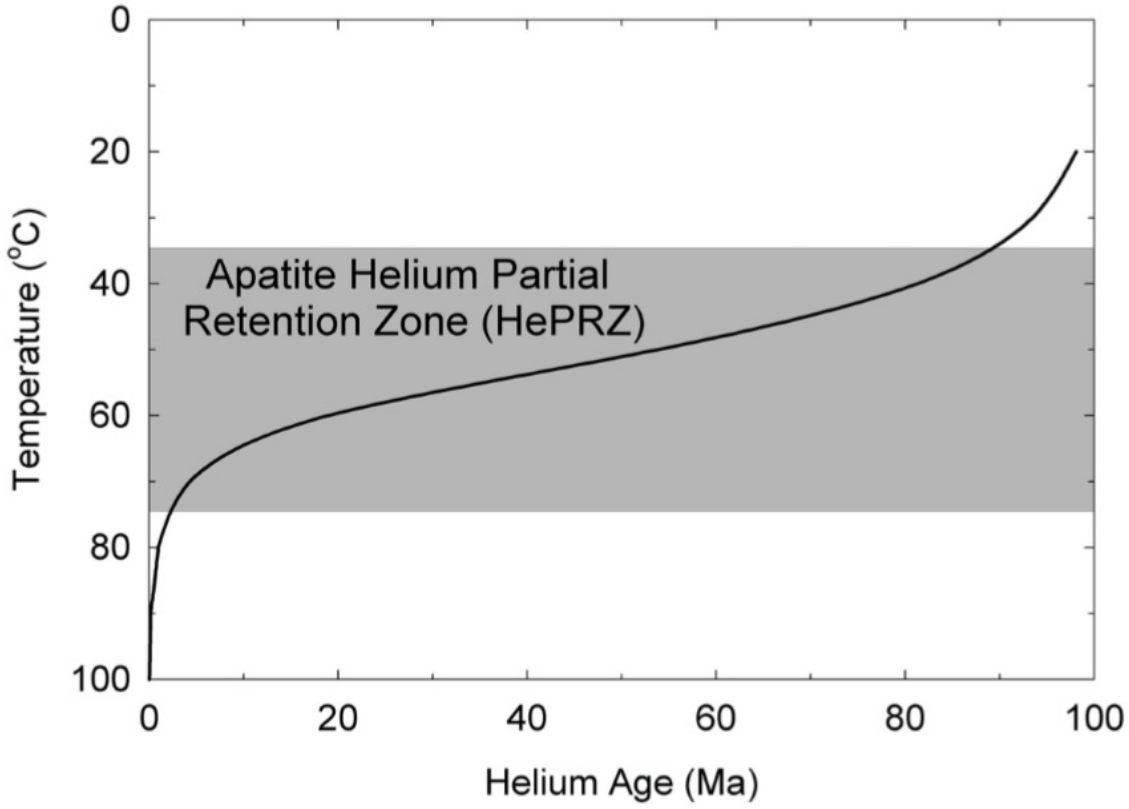

Figure 5: Apatite helium partial retention zone. In an isothermal setting held for 100 Ma, apatite (U-Th)/He ages change most rapidly between 75^{O}Cand 35^{O}C; above 85^{O}C He ages are zero. Important to note, He ages are older at low temperatures than they are at high temperatures.

Sample preparations for Thermochronology

Twenty-six kimberlitic samples were selected for apatite (U-Th/He) analysis based both on the identification of apatite using polished thin sections under a petrographic microscope and selection of samples with a coarser grained matrix whereby apatite is typically embedded. Samples were then prepared for apatite grain disaggregation and isolation, at the University of the Witwatersrand, Earth Sciences Laboratory, using the following procedure:

- A clean working environment was always with table and equipment surface wiped down before commencing any sample preparation and/or analytical work.
- Sample cross-contamination was avoided by working with only one sample at a time, and all mills and permanent sieves were cleaned thoroughly in between samples.
- Rock samples were crushed into small-sized pieces (5 cm) using a hammer and plastic wrap, and put subsequently into separate containers. Sample names were clearly written on both the container and lid with durable permanent marker.

- Sample rock crush/chips were ground down to silt- and sand-sized particles using the Fe-carbide steel disk mill machine (or “shatter box”), for no longer than 10 to 15 seconds.
- Samples were sieved using a 500 µm mesh and the >500 µm size fraction were re-ground as described above. This step was repeated until all sample material is <500 µm in size (silt to middle sand grain size), e.g. 2 to 5 times.
- The milled samples of the preferred size were put into a glass beaker, suspended in water and then decanted to discard undersize fraction (e.g., clay to fine silt). This process was repeated until undersize fraction was eliminated.
- Different-sized sieves were used to retain the grain size fraction of interest; in this case 75-200 µm is the desired grain size fraction, but the 200-500 µm and the <75 to ~20 µm fractions are also recovered, dried, and stored.
- Wet sieving of samples was done using (13 x 10 cm) disposable 200 µm mesh made from plastic (cutting and taping mesh onto a plastic bucket), followed by small 75 µm metal mesh. Samples were allowed to dry before packing. Final rinsing of samples was often conducted with ethanol in order to facilitate faster drying.

Equipment’s used:

- Class-5 glass beakers for decanting, sample handling, and potential oven-drying
- Plastic containers for sieving
- Duct tape/ electrical tape for securing mesh onto plastic containers
- Pair of scissors or carpet knife to cut-out bottoms of plastic containers
- Permanent marking pens
- 500 µm permanent metal mesh
- 200 µm one-way plastic mesh
- 75 µm permanent metal mesh

Appendix C1- Explanation for denudation estimates

Denudation estimates (section 4.1. of the thesis) for the kimberlites studied in this project were estimated from the time- temperature plots (Fig. 13 E,F of section 4.2.1) retrived from HeFTy simulations. The following tables show the different segments; only segments that are indicated as cooling were used to estimate denudation rates.

Table C1: Time-temperature segments for the studied kimberlites

SK-1 & SK-2				
	Segment A (period)	Segment B (period)	Segment C (period)	Segment D (period)
Period (Ma)	1100(130)-655(175)	655 (175)-500(115)	500(115)-200(75)	200(75)-175(30)
Thermal History	Heating/ increased T	Fast cooling	Slow cooling	Cooling in the PRZ
change in T (^{o}C)	45	60	40	45
CC-5				
Time with Temp	1100 (130)-615(178)	615(178)-360(160)	360(160)-175(75)	
Thermal History	Heating	slow cooling	Fast cooling	
change in T (^{o}C)	48	18	85	

Table C2: Calculations for denudation rates

CC-5						
Age (Ma)	**Temperature (^{o}C)**	**Cooling rate (^{o}C/Ma)**	**Geothermal Gradient (^{o}C/km)**	**Denudation rate (km/Ma)**	**No. of years in a period (Ma)**	**Denudation X No. of yrs in a period (km)**
615	18	0.029	20	0.001	255	0.37
360	85	0.236	20	0.012	185	2.18
					Total	**2.6**
SK-1 & SK-2						
655	60	0.092	20	0.005	155	0.71
500	40	0.080	20	0.004	300	1.20
200	45	0.225	20	0.011	30	0.34
					Total	**2.2**

Table C1 shows the segmenst for the chosen HeFTy plots, whereas table C2 shows denudation estimates. The following formulas were used to calculate cooling rates and denudation rates, respectively, a geothermal gradient of 20 ^{0}C/km was used:

$$Cooling\ rate\ (°C/Ma) = \frac{Temperature\ (°C)}{Time\ (Ma)}$$

$$Denudation\ \left(\frac{km}{Ma}\right) = \frac{Cooling\ rate\ \left(°\frac{C}{Ma}\right)}{Geothermal\ Gradient\ \left(°\frac{C}{km}\right)}$$

To get denudation in kilometres: denudation was multiplied by the number of years in a period e.g. 655- 500 Ma will yield 155 Ma difference. The sum for the denudation was calculated to yield a single final denudation rate in km.